



2011-05-17

# Soap Bubbles and Solid Spheres: Collisions and Interactions

Joshua A. Bryson

*Brigham Young University - Provo*

Follow this and additional works at: <https://scholarsarchive.byu.edu/etd>

 Part of the [Mechanical Engineering Commons](#)

---

## BYU ScholarsArchive Citation

Bryson, Joshua A., "Soap Bubbles and Solid Spheres: Collisions and Interactions" (2011). *All Theses and Dissertations*. 3016.  
<https://scholarsarchive.byu.edu/etd/3016>

This Thesis is brought to you for free and open access by BYU ScholarsArchive. It has been accepted for inclusion in All Theses and Dissertations by an authorized administrator of BYU ScholarsArchive. For more information, please contact [scholarsarchive@byu.edu](mailto:scholarsarchive@byu.edu), [ellen\\_amatangelo@byu.edu](mailto:ellen_amatangelo@byu.edu).

Soap Bubbles and Solid Spheres: Collisions and Interactions

Joshua Bryson

A thesis submitted to the faculty of  
Brigham Young University  
in partial fulfillment of the requirements for the degree of  
Master of Science

Tadd T. Truscott, Chair  
Jeffrey Humpherys  
Steven E. Gorrell

Department of Mechanical Engineering  
Brigham Young University  
June 2011

Copyright © 2011 Joshua Bryson  
All Rights Reserved



## ABSTRACT

### Soap Bubbles and Solid Spheres: Collisions and Interactions

Joshua Bryson

Department of Mechanical Engineering, BYU

Master of Science

Under the right conditions, a moving sphere may successfully enter, and leave, a soap bubble without rupturing that bubble. The physics behind this phenomena are not well understood, nor the limiting factors (such as sphere size, speed, etc.). This work, investigating this phenomenon using high speed photography, has produced several results which are presented. First, several distinct regimes, noted while photographing the interactions between the spheres and the bubbles, are classified and discussed. Next a probabilistic examination of the soap bubbles rupture by the moving spheres is presented. Then a conjecture for the limiting sphere sizes and speeds is presented. And finally some interesting phenomena, noted in the course of this investigation, are presented and discussed.

Keywords: soap bubbles, laplace equation, level set method, weber number



## ACKNOWLEDGMENTS

I am grateful for Dr. Truscott and his taking me on as a graduate student in my time of need. Also for his patience in reading and correcting my writing. I am also grateful for my committee and the time they spent to assist me in creating this work and for helping to guide me down the path of higher education.

I would like to thank Kyle for his help in designing and constructing the experimental setup and for helping to conduct the experiments.

I am grateful for my parents and their support over the last seven years. Also for my brother Zach for his countless hours of making bubbles with me.

Finally, I would like to thank my wife Autumn for her patience in enduring my long work hours and listening to my explanations and descriptions of things such as bubbles. I'd also like to thank my sons for being quiet while I worked and for playing with me and giving me diversion when I needed it.



## TABLE OF CONTENTS

<b>LIST OF TABLES</b> . . . . .	<b>vi</b>
<b>LIST OF FIGURES</b> . . . . .	<b>viii</b>
<b>NOMENCLATURE</b> . . . . .	<b>xiii</b>
<b>Chapter 1 Introduction</b> . . . . .	<b>1</b>
1.1 Objectives . . . . .	1
1.2 Background . . . . .	3
1.3 Soap Films and Bubbles . . . . .	3
1.3.1 Bubble Attributes and Governing Equations . . . . .	3
1.4 Thin Film Draining and Thickness . . . . .	4
1.4.1 Draining Models . . . . .	5
1.4.2 Thin Film Thickness Measurements . . . . .	5
1.4.3 Bubble Thickness and Interference Patterns . . . . .	6
1.5 Bubble Rupturing . . . . .	8
1.6 Bubble Modeling . . . . .	9
1.6.1 The Level Set Method . . . . .	9
1.7 High-Speed Photography . . . . .	11
1.8 Conclusions . . . . .	11
<b>Chapter 2 Experimental Methods</b> . . . . .	<b>13</b>
2.1 Experimental Setup . . . . .	13
2.1.1 Experimental Setup and Design . . . . .	13
2.2 Experimental Variables and Parameters . . . . .	17
2.2.1 Bubble Sizes . . . . .	17
2.2.2 Ball Surface Measurements . . . . .	18
2.2.3 Bubble Thickness . . . . .	19
2.2.4 Soap Solution Measurements . . . . .	23
2.3 Conclusions . . . . .	26
<b>Chapter 3 Experimental Results and Discussion</b> . . . . .	<b>27</b>
3.1 Regime Classification and Examples . . . . .	27
3.1.1 Pinch-off Order . . . . .	27
3.1.2 Film Bridge Shape Just Before Pinch-off . . . . .	28
3.1.3 Film Bridge Collapse . . . . .	29
3.1.4 Regime Descriptions . . . . .	30
3.2 Discussion of the Regimes . . . . .	46
3.3 Rupture Criteria . . . . .	50
3.3.1 Methods of Soap Film Rupture . . . . .	51
3.3.2 Probability of Rupture . . . . .	57
3.3.3 Rupture Dependence on Weber Number and Radius . . . . .	63



3.4	Conclusions . . . . .	69
<b>Chapter 4</b>	<b>Discussion of Interesting Phenomena . . . . .</b>	<b>71</b>
4.1	Sphere Encapsulation . . . . .	71
4.2	Curvature Battle . . . . .	73
4.3	Film Rupture: Pinch-off Repair . . . . .	76
4.4	Comparison of Linear Stretch Rates . . . . .	78
4.5	Surface Tension Forces . . . . .	78
4.6	Conclusions . . . . .	80
<b>Chapter 5</b>	<b>Conclusions . . . . .</b>	<b>81</b>
5.1	Summary . . . . .	81
5.2	Future Work . . . . .	82
<b>REFERENCES</b>	<b>. . . . .</b>	<b>83</b>

## LIST OF TABLES

2.1	Bubble sizes for both top and bottom halves of the bubble. . . . .	17
2.2	Sphere property values, (mean $\pm$ stdev [samples size]). . . . .	19
2.3	Viscosity and density values used for soap film calculations. . . . .	24
3.1	Chart of regimes with example pictures of their definitions and the Weber numbers defining their creation. . . . .	42
3.2	Limiting Weber numbers for each regime, upper hemisphere. . . . .	47
3.3	Limiting Weber numbers for each regime, lower hemisphere. . . . .	48
4.1	Gravitational to surface tension forces table. . . . .	80



## LIST OF FIGURES

1.1	Pictures from Bull’s photo series <i>Soap Bubble Bursting</i> . Note the successful entry of the paper pellet by the last frame. . . . .	1
1.2	Example of a bubble being pierced by a sphere . . . . .	2
1.3	Unperturbed and perturbed bubbles connected by a solid tube. . . . .	5
1.4	Bubble thickness profile examples. . . . .	7
1.5	Examples of interference patterns. . . . .	7
2.1	Experimental setup, the red arrows indicate directions of movements . . . . .	15
2.2	Photographs of the experimental setup . . . . .	16
2.3	Picture of the different spheres used in the experiment . . . . .	18
2.4	Sessile drop test example pictures. In this case the sphere is the 9.4 mm radius aluminum. . . . .	19
2.5	Example picture gauging the thickness of the bubble film. The dark arcs are the destructive interference rings on the bubble. Their distorted shape is a result of the projection of the bubble onto the screen. The ‘fan’ of dark lines are the reflection of the shadow cast by the 5 mm spaced screen, placed between the bubble and the laser. . . . .	20
2.6	Experimental setup for determining bubble film thickness as a function of time. . .	21
2.7	Newton black film example. The film is at the newton black film state in the center near the bottom both frames. Note the distinctive dark circle displayed by the film. The black film grows in time from image (a) to (b), 1.22 seconds later. . . . .	21
2.8	Bubble soap film drainage Profile examples. These plots have an accuracy of $\pm 5$ nm for the thickness and $\pm 0.5$ mm for the location. . . . .	22
2.9	Results of the rheometry tests. . . . .	24
2.10	Setup of the surface tension measurement system. . . . .	25
2.11	Plot of the experimental data for determining the surface tension. The slope of the best fit line represents the surface tension, so the surface tension $\sigma = 0.0263 \pm 0.015$ N/m. . . . .	25
3.1	Pinch-off location examples. Each of these pictures come from the our experiments and represent the different pinch-off types. . . . .	28
3.2	Soap film bridge funnel type examples. . . . .	29
3.3	Type (I) regime example. A 0.48 cm radius glass sphere dropped from 23.5 cm above the top of a 3.75 cm radius bubble. The shape is catenary and pinch-off order is bubble side first, sphere side second. Notice the catenary shape develop as the glass sphere interacts with the soap film, especially in frame (I). Both pinch-off locations occur between frames (I) and (J), see Figure 3.4 for greater detail. Frames are 1.5 ms apart. . . . .	32
3.4	This set of pictures displays what happens between frames (I) and (K) of Figure 3.3, only with frames 0.5 ms apart. This figure clearly shows pinch-off occurring first near the bubble (frame (C)). . . . .	33

3.5	A 0.63 cm radius aluminum sphere dropped from 15 cm above the bottom hemisphere of a 5.0 cm radius bubble. This is a type (I) regime exhibiting a catenary shape with pinch-off order occurring bubble side first then bridge collapse (see frame(K)). Note the lack of a satellite bubble. Though not always the case, this is due to the amount of liquid flowing to the bottom of the bubble (i.e. drainage). Frames are 2.0 ms apart. . . . .	34
3.6	A 0.48 cm radius glass sphere dropped from 51.5 cm above the top of a 5.0 cm radius bubble. For this type (II) regime the shape is catenary and pinch-off order is simultaneous. Notice that a similar catenary shape develops as in the first regime, especially in frame (J). Both pinch-off locations occur between frames (K) and (L). For increased temporal resolution in the last frames, an overall view was not given. Frames are 0.67 ms apart. . . . .	35
3.7	A 0.48 cm radius glass sphere dropped from 25.7 cm above the bottom hemisphere of a 2.25 cm radius bubble. This type (II) regime is defined by its catenary shape, simultaneous pinch-off order and the collapse of the film bridge. Note in frame (L) that, along with two satellite bubbles, a column of water droplets are seen indicating the presence of additional fluid as seen in the last case. Frames are 1.5 ms apart. . . . .	36
3.8	Example of regime type (III). 0.48 cm radius glass sphere dropped from 113.9 cm above the top of a 3.75 cm radius bubble. This is a cone funnel shape with pinch-off occurring sphere side first. A key characteristic of this regime is the quick collapse of the film bridge after pinch-off, see frames (H) and (I). Also note the relatively small satellite bubble. Frames are 1.5 ms apart. . . . .	37
3.9	A 0.48 cm radius glass sphere dropped from 90.3 cm above the bottom hemisphere of a 5.0 cm radius bubble. This type (III) regime is characterized by its cone-like shape, sphere side first pinch-off order, and film bridge collapse. Frames are 1.33 ms apart. . . . .	38
3.10	A 0.94 cm radius aluminum sphere dropped from 113.9 cm above the top of a 3.75 cm radius bubble. In this type (IV) the film is distorted into a hopper funnel shape and pinch-off occurs sphere side first. Notice that the disturbed film does not collapse in on itself after sphere pinch-off, as it does in Figure 3.8. Instead, the funnel stays open, frames (I) - (K), until the bubble side pinch-off occurs, capturing a large satellite bubble, frame (L). Frames are 2.5 ms apart. . . . .	39
3.11	A 0.63 cm radius aluminum sphere dropped from 94.0 cm above the bottom hemisphere of a 5.0 cm radius bubble. This type (IV) regime displays a hopper bridge shape with pinch-off occurring sphere side first. The film bridge pinches-off and captures a relatively large satellite bubble (see frame K). Frames are 2.67 ms apart. . . . .	40
3.12	A 0.94 cm radius aluminum sphere dropped from 95.0 cm above the bottom hemisphere of a 5.0 cm radius bubble. This final regime, type (V), occurs only when spheres fall through the lower hemisphere of the bubble. The regime is defined by its elongated hopper shape and sphere side pinch-off order. The film bridge pinches-off, resulting in a large satellite bubble. Note that not only is the funnel shape elongated, but that the time the film takes to pinch-off the sphere has also increased in comparison to the hopper funnel type described above. Frames are 4.0 ms apart. . . . .	41

3.13	Regime diagram showing the dependance of the film bridge shape, pinch-off order and collapse as the spheres were dropped through the upper half of the bubble. Upward pointing triangles, circles, downward pointing triangles, and diamonds indicate the four regimes, as described previously. Note the case with $r/R$ near zero. This case was produced by dropping the larger aluminum sphere through a flat film, thus approximating a bubble of infinite radius. For calculations a radius of 5,000 cm was used. Marker size indicates the size of sphere dropped, e.g. larger spheres have larger markers, smaller spheres have smaller markers. . . . .	47
3.14	Regime diagram showing the dependance of the film bridge shape, pinch-off order and collapse as the spheres were dropped through the lower half of the bubble. Upward pointing triangles, circles, downward pointing triangles, diamonds, and asterisks indicate the five regimes noticed for the lower bubble half, as shown at the right respectively. Markers are filled to further indicate downward bubble orientation. Marker size indicates the size of sphere dropped, e.g. larger spheres have larger markers, smaller spheres have smaller markers. . . . .	48
3.15	Regimes plotted Weber vs Bond number, for the upper half of the bubble. Notice that the regimes span nearly a century of bond numbers. Upward pointing triangles, circles, downward pointing triangles, and diamonds indicate the four regimes, as described respectively. Marker size indicate size of sphere dropped, e.g. larger spheres have larger markers, smaller spheres have smaller markers. . . . .	49
3.16	Regimes plotted Weber vs Bond number, for the lower half of the bubble. Notice that the regimes span nearly a century of bond numbers. Upward pointing triangles, circles, downward pointing triangles, diamonds, and asterisks indicate the five regimes noticed for the lower bubble hemisphere, as described respectively. Markers are filled to further indicate downward bubble orientation. . . . .	50
3.17	Example of a pinch-off rupture. The pinch-off occurs between frames (H) and (I) when the ‘tail’ at the bottom of the hopper funnel shape pinched-off. These are pictures of a 0.63 cm radius aluminum sphere falling from 222 cm above the upper hemisphere of a 1.5 cm radius bubble. Frames are 1.5 ms apart. . . . .	52
3.18	Example of a thinning rupture. The film is torn between frames (F) and (G). These are pictures of a 0.48 cm radius glass sphere falling from 124.6 cm above the upper hemisphere of a 2.25 cm radius bubble. Frames are 1.5 ms apart. . . . .	53
3.19	Example of a contact rupture. Note that by frame (C), with minimal displacement, the film is already ruptured. These are pictures of a 0.48 cm radius glass sphere falling from 183.4 cm above the upper hemisphere of a 2.25 cm radius bubble. Frames are 1.0 ms apart. . . . .	54
3.20	Example of a side rupture. Note the beginning of the rupture in frame (H) . These are pictures of a 0.94 cm radius aluminum sphere falling from 40 cm above the upper hemisphere of a 1.5 cm radius bubble. Frames are 1.5 ms apart. . . . .	55
3.21	Probability of bubble popping sorted by regime Weber numbers, for the upper hemisphere. The numbers in the middle of the figure indicate the number of samples taken for each data set. . . . .	58
3.22	Probability of bubble popping according to Weber number, for the upper hemisphere. The numbers in the middle of the figure indicate the number of samples taken for each data set. . . . .	59

3.23	Probability of bubble popping sorted by $r/R$ , for the upper hemisphere. The numbers in the middle of the figure indicate the number of samples taken for each data set. . . . .	59
3.24	Probability of the lower hemisphere of the bubble popping according to regime. The numbers in the middle of the figure indicate the number of samples taken for each data set. . . . .	61
3.25	Probability of the lower hemisphere of the bubble popping according to $We$ . The numbers in the middle of the figure indicate the number of samples taken for each data set. . . . .	61
3.26	Probability of the lower hemisphere of the bubble popping according to $r/R$ . The numbers in the middle of the figure indicate the number of samples taken for each data set. . . . .	62
3.27	Probability of the upper hemisphere of the bubble popping according to $r$ . The numbers in the middle of the figure indicate the number of samples taken for each data set. . . . .	62
3.28	Probability of the lower half of the bubble popping according to $r$ . The numbers in the middle of the figure indicate the number of samples taken for each data set. . . . .	63
3.29	Combination of all experimental results for the upper hemisphere. Attention is only paid to whether or not the bubble ruptured. . . . .	64
3.30	Combination of all data for the lower hemisphere. Attention is only paid to whether or not the bubble ruptured. . . . .	64
3.31	Diagram of the first stage of the surface area approximation. $R$ is the radius of the film disk, $r$ is the radius of the sphere, and $y$ is the distance the sphere has fallen. . . . .	66
3.32	Dimensions and layout used in Equation (3.5) . . . . .	66
3.33	Diagram second stage, sphere is more than half way through the film. $R$ is the radius of the film disk, $r$ is the radius of the sphere, and $y$ is the distance the sphere has fallen. . . . .	67
3.34	Plot of film thickness as a function of time. Thickness is calculated using Equation (3.4). Each line represents a different sphere. . . . .	69
3.35	Plot of film thickness as a function of time. Thickness is calculated using Equation (3.4). Each line represents a different initial velocity for a 9.4 mm radius aluminum sphere. . . . .	69
4.1	Images of a 6.3 mm radius aluminum sphere being encapsulated. Note the descent of the bubble, initially located at the top of the sphere (frame (E)), down the side of the sphere (frames (F) - (J), until, by frames (K) and (L) the encapsulating bubble's film has moved below the sphere. If the sequence of frames were continued, the bubble would be pushed up again as drag forces push on the bubble. . . . .	72
4.2	Enlargement of the encapsulated sphere from frame (J) in Figure 4.1 . . . . .	73
4.3	An example of a failed bubble side pinch-off attempt. In this example the lower hemisphere of a 2.25 cm bubble was pierced by a 9.4 mm radius aluminum sphere. Sphere side pinch-off has already occurred by frame (A). Note the necking occurring in frames (A)-(F) and the sudden expansion of the 'neck' by frame (G). Another pinch-off attempt is successfully completed by frame (K). . . . .	74

4.4	Frame (F) from Figure 4.3 with indications of high and low pressure spots as well as general forces acting on the film. Note, arrow size is unimportant. . . . .	75
4.5	This interesting phenomenon of film rupture and pinch-off repair occurred in the lower hemisphere of a 5 cm radius bubble with a 9.4 mm radius aluminum sphere falling through it. The sphere was dropped from a height of 95 cm. Note the thinning rupture by frame (G) and the pinch-off of the ruptured film in frame (K). . . . .	77
4.6	Film profile information. Each profile, with the top profile representing our initial time, $t = 0$ s, represents the film profile after 1.5 ms from the previous profile. The profiles are offset by 3 cm per 1.5 ms for clarity. Also, each profile on each axis is the profile of a 3.75 cm bubble being deformed by a sphere. For the regime II and III profiles, the dropped sphere is a 4.8 mm radius glass sphere dropped from a height of 23.5 cm and 113.9 cm respectively . The regime IV profile was created by a 9.4 mm aluminum sphere dropped from a height of 113.9 cm. . . . .	79
4.7	Percent increase in surface area as a function of time for the three profiles found in Figure 4.6. Each data set is fit with a linear polynomial. Note the highly linear results for regimes III and IV, while the regime II profile is very non-linear. . . . .	80



## NOMENCLATURE

$p_0$	Atmospheric Pressure
$\sigma$	Surface Tention
$\Delta p$	Pressure Difference
$T$	Film Thickness
$t$	Time
$\lambda$	Wavelength of light
$n$	Index of refraction
$R$	Radius of curvature/Bubble
$r$	Sphere radius
$\theta$	Wetting angle
$\mu$	Viscosity
$\rho$	Density
$u$	Velocity
$h$	Height
$We$	Weber number
$Bo$	Bond number
$\nabla$	Volume
$A_s$	Surface Area

## CHAPTER 1. INTRODUCTION

In 1904 Lucien Bull, a cinematographer interested in developing high-speed photography methods, published a series of photos entitled *Soap Bubble Bursting*, part of which may be found in Figure 1.1. Bull later described the process captured in the photos as the 'bursting of a soap-bubble caused by a paper pellet shot from a little spring gun' [1]. The film clearly shows the pellet entering the bubble without bursting it<sup>1</sup> (also shown in Figure 1.2). This publication is the first recorded example of the amazing ability of a bubble to reseal itself after being pierced by a moving object. Although resealing also occurs on exit, this was not recorded in Bull's work. Since Bull's work in 1904, little investigation has been done into this fascinating phenomenon.



Figure 1.1: Pictures from Bull's photo series *Soap Bubble Bursting*. Note the successful entry of the paper pellet by the last frame.

### 1.1 Objectives

This work investigates the remarkable phenomenon of a bubble's ability to reseal itself after the entry of a solid object. Specifically, the work address the following three questions: first, what are the characteristics or properties of this phenomena? Second, under what conditions does the passing sphere rupture the bubble? Finally, third, can a model be developed to capture bubble rupture?

---

<sup>1</sup>You may view the movie online via youtube.com. URL: <http://www.youtube.com/watch?v=RLR-LT55Ueo> last accessed 1/27/2011

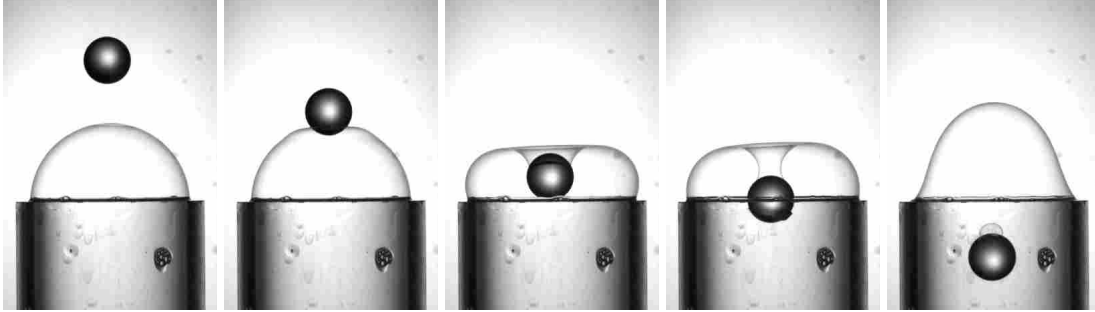


Figure 1.2: Example of a bubble being pierced by a sphere

This phenomena was studied by capturing the interaction of solid spheres being dropped through soap bubbles, with the radii, masses, and materials of the spheres, as well as the bubble size, being varried.

This investigation has lead to the classification of five interesting sphere-bubble interaction regimes, dependent on the Weber number of the moving sphere. Additionally, the importance (in terms of limiting bubble rupture) of the moving sphere's radius, and the ratio of sphere radius to the bubble radius has been quantified. The importance of the film's thickness was also noted.

It was hoped that a complete numerical model of the phenomenon might be developed: a model able to capture both the physical interactions between the moving spheres and soap film and also the actual rupturing dynamics of the film. However, numerical modeling of a soap film as a very thin sheet, with finite volume (required to accurately capture the rupture dynamics), rather than as a surface, is beyond the capabilities of current numerical schemes.

One reason for the lack of such a numerical scheme involves the need to solve the Navier-Stokes equations across a three dimensional domain many orders of magnitude larger than the film itself (centimeters vs. nanometers). A model spanning both the film thickness and the bubble size scales would surely crumple under the weight of the number of spacial nodes required to do so. Indeed, a modeling method used to solve for just the film dynamics, which is not able to handle film rupture, requires nearly a million spacial nodes for proper convergence, each of which needs to be solved in time. Thus, we will settle for a more probabilistic approach to model under what conditions a bubble will rupture when being pierced by a moving sphere.

## 1.2 Background

Although past work studying bubble-solid collisions is limited to the work done by Bull, there has been research into related phenomena, such as the study of soap film, bubbles, etc.. We will review this work in the following way. First, we will investigate work done in the area of soap films and soap film bubbles. This includes governing equations, thinning, thickness determination, and modeling. Second, the work done regarding numerical models of thin films and bubbles will be investigated.

## 1.3 Soap Films and Bubbles

Soap films have been formally studied for nearly 150 years. Yet, their history in nonscientific circles goes back even further. In the 17th century it was used in paintings and prints as a representation of the frailty of life [2]. The Assyrians even used very thin soap films to help divine the future [3].

In their most basic form soap films are formed by mixing a surfactant with water. Most people do this regularly by simply mixing liquid detergent with tap water. The surfactant plays a critical role in the creation of soap bubbles in that it lowers surface tension and allows the film to stand against its own weight in the air. The surfactant does this because of its chemical makeup.

A surfactant usually consists of a hydrophilic head and a hydrophobic tail [4]. This arrangement causes the surfactant to rise to the surface with the tail sticking out of the water. This causes the surface tension to drop. In a film, there is a monolayer of surfactant on either side of the film with a water-surfactant mixture between the two layers. These monolayers have a density greater than the water-surfactant mixture and this is what allows the soap film to be able to support its own weight [3].

### 1.3.1 Bubble Attributes and Governing Equations

The shape of a bubble is governed by its surface tension. Surface tension forces a bubble to minimize the surface area for the enclosed volume. This force also causes an internal pressure to develop inside the bubble, in excess of the pressure outside the bubble. The pressure difference at any point along the bubble wall is defined by the Laplace pressure relation:

$$\Delta p = \sigma \left( \frac{1}{R_1} + \frac{1}{R_2} \right), \quad (1.1)$$

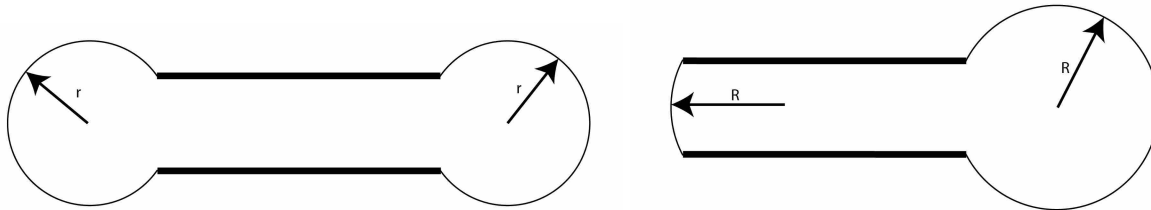
where  $\Delta p$  defines the pressure difference,  $\sigma$  is the surface tension of the bubble and  $R_1$  and  $R_2$  are the principle radii of curvature of the bubble at that location. Under steady state conditions the soap film's tendency to minimize the surface area forces the bubble to form a sphere. Because  $R_1 = R_2$  for a sphere the internal pressure is constant at every point along the wall of the bubble, and thus is constant throughout the entire bubble [3]. Although the final shape of a bubble is known, the path a bubble takes to reach this spherical state from some perturbed condition has not been well modeled.

If a soap bubble is initially non-spherical in shape, then surface tension and pressure gradients will drive the surface energy to its minimal state, resulting in the spherical shape [3]. Pressure gradients are defined by the Laplace pressure (1.1) which is a function of the gaussian curvature and the surface tension equation. If a bubble is deformed, the areas with lower curvature develop higher pressure while areas with higher curvature have lower pressures [3].

A simple demonstration of this may be seen in an experiment involving two bubbles of equal size, connected together by a hollow tube. If one bubble is perturbed slightly, air from that bubble will flow into the other bubble, increasing the unperturbed bubble's size and decreasing its own. The perturbed bubble now has a smaller curvature, being a sphere holding less volume, and thus has a higher pressure. The unperturbed bubble, now larger, has a larger curvature and thus a lower pressure. From this unbalanced state the air will empty from the smaller bubble into the larger one. The perturbed bubble will completely deflated until it becomes a film at the end of the tube, with a final curvature equal to the final curvature of the, now much larger, originally unperturbed bubble [5]. See Figure 1.3.

#### **1.4 Thin Film Draining and Thickness**

As discussed above, a thin film consists of two monolayers of surfactant surrounding a water-surfactant solution. Under the force of gravity the solution drains from in between the monolayers down the film [6, 7]. The mixture drains through three mechanisms, Poiseuille flow, convective flow, and flows due to Laplace pressure differences within the film [3]. This draining



(a) Initial, unstable condition. Each bubble is equal in size and have the same curvature  
 (b) Final, stable condition. In this case, each bubble has the same curvature but their sizes are unequal.

Figure 1.3: Unperturbed and perturbed bubbles connected by a solid tube.

continues until the water-surfactant solution has all drained, leaving just the two monolayers. At this point the film is called a Newton black film, named after Sir Isaac Newton who studied them in the 18th century. The term black refers to the 'see through' nature of these thin films, which occurs due to the thickness being below the diffraction limit ( $<100\text{nm}$ ).

#### 1.4.1 Draining Models

Schwartz and Roy [8], and Naire et al. [9] have developed models of the thinning which takes place in a vertical film over time. Both models simplify the mathematics by utilizing the lubrication approximation and both arrive at a solution using three nonlinear partial differential equations. However, neither formulation was developed to allow a changing film orientation (as is the case with a bubble). Thus, it becomes necessary to obtain thickness measurements through experimental means.

#### 1.4.2 Thin Film Thickness Measurements

As with any study involving thin films, the films thickness plays a critical role. Small changes in film thickness can dramatically alter the response of the fluid to the experimental conditions. Because of this, many methods for measuring the thickness of a thin film have been devised. The most common of which are ellipsometry, reflectometry and interferometry.

Ellipsometry works by shining polarized light, with a known angle of incidence, at the film and measuring the change in the polarization angle. The polarization angle can then be used to derive the desired attributes about the film, including thickness and index of refraction. The

light used can be either monochromatic light [10] or a spectrum of light wavelengths for greater accuracy [11]. These methods generally require the use of a substrate with known optical properties upon which the thin film is placed, though some methods have been developed for transmission ellipsometry, see [12].

In contrast with ellipsometry, reflectometry and interferometry are both methods which utilize light intensity properties to gauge film thickness. Reflectometry analyses the amount of light reflected off a thin film over a spectrum of wavelengths [13].

Interferometry splits a light beam and later superimposes the resulting light beams to form an interference pattern. In this way information about changes in wavelengths may be measured with great accuracy. This in turn may be used to gather information about the films properties [14, 15].

Although these methods are widely used in industry and research, their application is not suited for the problem at hand. This is due to geometric considerations. It is clear that classical ellipsometry is ill suited due to the use of the substrate for measurements. Transmission ellipsometry and classical methods of reflectometry and interferometry all suffer from the same shortcoming, namely that they require the transmission and measurement of light through the film. In our case, this would require either the light source, or the receiver to be located inside the bubble. This makes their use for measuring the thickness of a bubble impractical, at best. Thus we turn to interference patterns for a solution.

### **1.4.3 Bubble Thickness and Interference Patterns**

As stated above, the drainage of a soap film due to gravity also causes the profile of a soap film bubble to change with location, see Figure (1.4(a)). If an infinitesimal slice of the bubble is taken and straightened out, it may be seen that that slice forms a wedge of decreasing thickness, see Figure (1.4(b)).

The illumination of the thickness variations in a thin film (caused by drainage or otherwise) reveals interference patterns on the surface of the film. For example, under white light (or a spectrum of light wavelengths), these interference patterns are demonstrated by regions of differing colors, with each color representing an area of differing thickness. Illumination under a monochromatic light yields light and dark areas which represent the different thicknesses of the

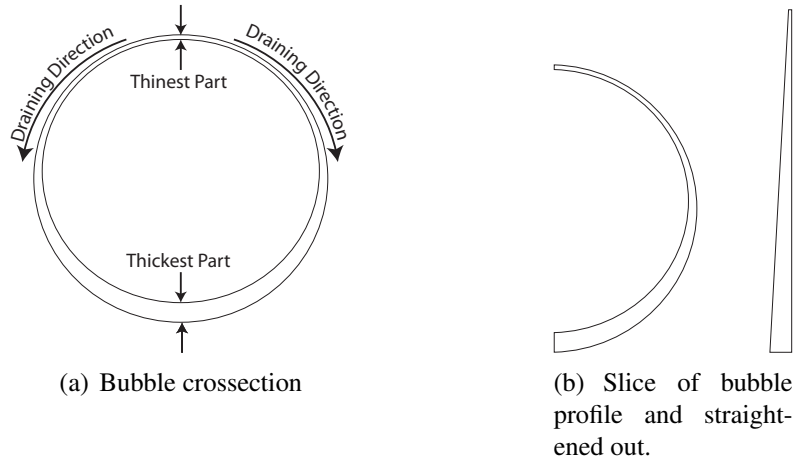
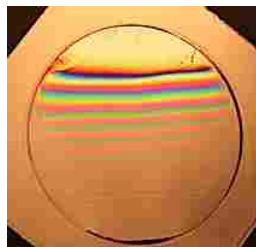
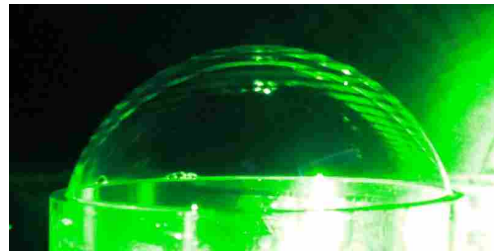


Figure 1.4: Bubble thickness profile examples.

film. Interference patterns are demonstrated by horizontal bands of color, as seen in Figure (1.5(a)) for a film wedge. If viewed under a light of a single wavelength (or a small band of wavelengths), light and dark rings are seen circling the bubble, see Figure (1.5(b)).



(a) Wedge with interference lines shown



(b) Bubble with interference rings shown

Figure 1.5: Examples of interference patterns.

These rings may be used to measure the thickness of the bubble profile in time by utilizing the well developed theory of interference for thin film [7, 14]. This theory yields the following equations for the thickness of a thin film wedge:

$$t = \frac{(m + \frac{1}{2})\lambda}{2n} \quad m = 0, 1, 2, \dots \quad (1.2a)$$

$$t = \frac{m\lambda}{2n} \quad m = 0, 1, 2, \dots \quad (1.2b)$$



where  $\lambda$  is the wavelength of light,  $t$  is the film thickness and  $n$  is the index of refraction for the thin film. Equation (1.2a) refers to the thickness of the film at the  $m$ th constructive interference band. Equation (1.2b) refers to the thickness at the  $m$ th destructive interference band.

The utilization of interference patterns to measure the thickness of the thin film is a straight forward method. One must simply capture the interference band locations in time. These bands appear at the top of the fluid as it thins and move down the film. Once the film reaches a thickness smaller than the wavelength of the light being used to illuminate the film, no new bands will appear. At this point the last new interference band represents the thickness where  $m = 0$ . With this marker we may evaluate the thickness of each band using Equations 1.2a and 1.2b.

The advantage of this method over standard ellipsometry, reflectometry, and interferometry, is that the bubble may simply be formed and photographed to determine the thickness at any point in time. As mentioned above, ellipsometry, reflectometry, and interferometry, require either the use of a substrate or the reflection through a single membrane. This makes their use difficult at best. Furthermore, these methods only take point samples of the thickness, while the capture of interference patterns yield profile information for the entire bubble.

However, this method does suffer from several disadvantages. First, for the best accuracy, a monochromatic light source should be used and the wave length of that source needs to be known. Even if a monochromatic light is used, the accuracy of the method is limited to the wavelength of that light, see Equation (1.2). The second disadvantage of this method stems from the difficulty of photographing reflections off a transparent film. This requires careful light, camera, and backdrop positioning.

## **1.5 Bubble Rupturing**

The rupture of a thin film and, in the case of a bubble, the consequent bursting of the bubble has been studied for some time. As long ago as the late 1800's Rayleigh studied the recoil of ruptured film via photography and developed a model for the recoil speed using a kinetic energy argument [16]. However, this argument has proved somewhat too simplistic, under-predicting the recoil speed, and much work has been done to provide a more accurate model of film recoil after rupture [17] [18] [19].

Some work has been done into the requirements for film rupture. For example, Taylor and Michael [20] investigated the conditions under which thin sheets of fluids rupture by piercing the fluid with probes of different sizes. Their work suggests that rupture occurs when the radius of the probe is greater than the thickness of the sheet. But, if the probe has a radius smaller than the thickness of the sheet, the sheet is able to repair itself once the probe is withdrawn. In the case of soap films this seems to make sense, as the film usually ruptures once most of the fluid has drained from between the two monolayers of surfactant, leaving a film thickness on the order of 10 nm. At this point, nearly any disturbance of the film may create a hole with a radius greater than the thickness of the film.

## **1.6 Bubble Modeling**

Chen and Steen have developed a model able to capture the dynamics of a film bridge collapse and pinch-off [21], a process resembling the final stages of a sphere passing through a soap bubble's film. Their work investigated how an axisymmetric film bridge comes together and pinches off into two separate films. It does not, however, take into account different initial radii as is the case with spheres of different sizes passing through the bubble. Nor does the work address the presence of foreign and moving bodies.

Other work has been done on the growth and collapse of bubbles. Delale et al. developed analytical and numerical models for cylindrical vapor bubbles [22], while Kim et al. used a control volume method to simulate the growth of foam for graphical purposes [23]. However, neither of these works account for general shapes of bubbles but rather assume symmetry or ignore the driving forces governing the movement of the bubble.

### **1.6.1 The Level Set Method**

Because the curvature of a bubble determines its pressure, see Equation (1.1), and therefore pressure gradients, the shape the bubble takes in time is of critical importance. There are several methods for tracking the shape or interface of a fluid and each has its own merits and disadvantages. A method of particular usefulness is the level set method developed by Sethian in 1982. This method has the ability to accommodate fluid coalescence and breakup, and may also deal with

regions having different property values [24], [25]. It is these properties of the level set method which make it so applicable to the question at hand. As the sphere moves through the exterior of the soap bubble the film must move apart and some of the fluid even attaches itself to the sphere [26]. Thus any method attempting to accurately model these events must allow the fluid to act accordingly. The level set method allows for the modeling of these types of events. Although some work has been done to model bubbles using the level set method, [27] [28], their work does not model bubble-solid interactions.

The level set method is able to track changes in topology, the formulations of cusps, and other complicated geometries by embedding the surface of interest into a function of a higher dimensional space, with time providing the extra dimension. For example, a two dimensional surface, a function of  $x$  and  $y$ , would be imbedded in a three dimensional function,  $\phi(x(t),y(t),t)$ . This function,  $\phi$ , is called the level set function. Taking the time derivative of  $\phi$  and simplifying yields the level set equation:

$$\phi_t + F\|\nabla\phi\| = 0 \tag{1.3}$$

where  $\|\cdot\|$  represents the euclidian norm. The function  $F$  determines the speed in the outward normal direction of the evolution of the surface. The solution to this PDE yields the solution of how the higher dimensional surface evolves in time and the level set of this higher dimensional surface corresponding to  $t = 0$  represents the evolution of our original surface at any time step. A more complete formulation may be found in [29]. In practice the level set equation is usually solved numerically through a finite difference scheme [29].

One method of modeling the interaction between two fluids is called the Ghost Fluid method, developed by Fedkiw et al. [30] to help capture discontinuities between two phase contacts. The method works by discretizing the domain twice, once for each fluid. One set of nodes contains the mass, momentum, and energy information for the fluid really at that location, while the other set, the ghost cells, contains the mass, momentum, and energy information for the other fluid. The choice of which set of nodes to use at a particular location depends on the sign of the level set function Equation (1.3). With the domain discretized and defined in this manner, standard single phase numerical methods may be utilized to solve the problem and the level set function may be

evolved in time. The function is updated after each time step to ensure use of the correct fluid properties at each location [31].

One problem with level set methods is the ability of the method to lose mass in unresolved areas of the flow. Thus, while the level set method is moving along, the mass of the modeled water is disappearing from the system. Foster and Fedkiw proposed a method which hybridizes particle methods and the level set method, known as the particle level set method, to combat this problem [32]. This method works by refining the mesh in areas of high curvature within the system, adding extra resolution to the locations which suffer the most mass lost [31].

## **1.7 High-Speed Photography**

An important part of any numerical model is validation. Thoroddensen et al. provide a good overview of high-speed photography and its application in capturing fluid phenomena [33]. For example, in 1990 Ashgriz and Poo used high speed-cameras to capture the collisions of two droplets and classified the results [34]. Tanguy and Belemont used the images from Ashgriz and Poo's work to verify their numerical level set method model of droplet collisions.

## **1.8 Conclusions**

This chapter has presented research into soap films and their interactions and governing equations. Models covering bubble draining rates, film collapse and coalescence, as well as possible methods for their future modeling have also been presented. It is clear, however, that the research performed does not answer the question at hand. Namely: how does a moving object, specifically a moving sphere, successfully pass through a bubble without rupturing the bubble. The remainder of this work attempts to address that question.



## **CHAPTER 2. EXPERIMENTAL METHODS**

This chapter discusses the experimental setup, variables and parameters. First the experimental setup is described, both its physical appearance and its operation. Next the experiment variables are discussed and their parameters given.

### **2.1 Experimental Setup**

This section discusses the experimental setup, design and operation. First we will detail the bubble making apparatus and its operation. Then we will detail the methods of sphere handling and cleaning.

#### **2.1.1 Experimental Setup and Design**

Top, front, and side views of the experimental setup may be seen in Figures 2.1.1 and 2.2(a). The main frame consists of a central column supported by two legs and a cross brace. The frame was clamped near the top of the central column to the “T” channels supporting the ceiling tiles. This made the frame sufficiently ridged to eliminate vibration of the bubble when opening the iris. Attached to the frame are three movable arms mounted on linear bearings. These arms support the iris used to drop the spheres, the level used to gauge bubble size, and the arm supporting the bubble cylinder (see front view in Figure 2.1.1). The frame for the setup was constructed from 8020® extruded aluminum.

To create a bubble, a gloved hand was dipped into the soap solution (discussed in 2.2.4), and wiped across the top of a clear acrylic cylinder, referred to as the bubble cylinder. The bottom of this cylinder would have already been immersed in a bowl of water located on top of a scissor jack. The bubble is then created by raising the jack height, thus further immersing the bottom of the bubble cylinder in the water and creating a pressure inside of the cylinder and creating the top half of a bubble. The lower half of the bubble was created in a similar manner. First the film was

wiped across a plate of clear acrylic with a hole of the appropriate diameter cut into it. Then the plate was placed on top of a similarly immersed cylinder, but of a diameter larger than that of the hole in the acrylic plate (see Figure 2.2(b)). Next the water bowl is lowered, causing a vacuum in the cylinder which sucks the film downward, creating the bottom half of the bubble. Note that to ensure suction, the top of the bubble cylinder, upon which the plate was placed, was wetted with water before the plate was placed thereon.

In order to produce bubbles of the correct size a laser level was placed to shine a horizontal beam at the desired height above the top of the bubble cylinder. The scissor jack operator could watch the film move up the laser lines until reached the desired height and interrupted the beam. For speed, ease of use, and to lower the amount of fluid drainage, the chuck of an electric hand drill was connected to the screw of the scissor jack. The drill was then operated in forward or reverse, fast or slow, as was needed. A screen was placed to the side of the frame to capture the laser/bubble interactions.

The heights for the drops were varied by moving the iris up or down via moving the arm to which the iris was attached. Additionally, the location of the drop could be varied in/out and left/right by adjusting the cross piece attached to the iris arm. This helped in hitting the center of the bubble.

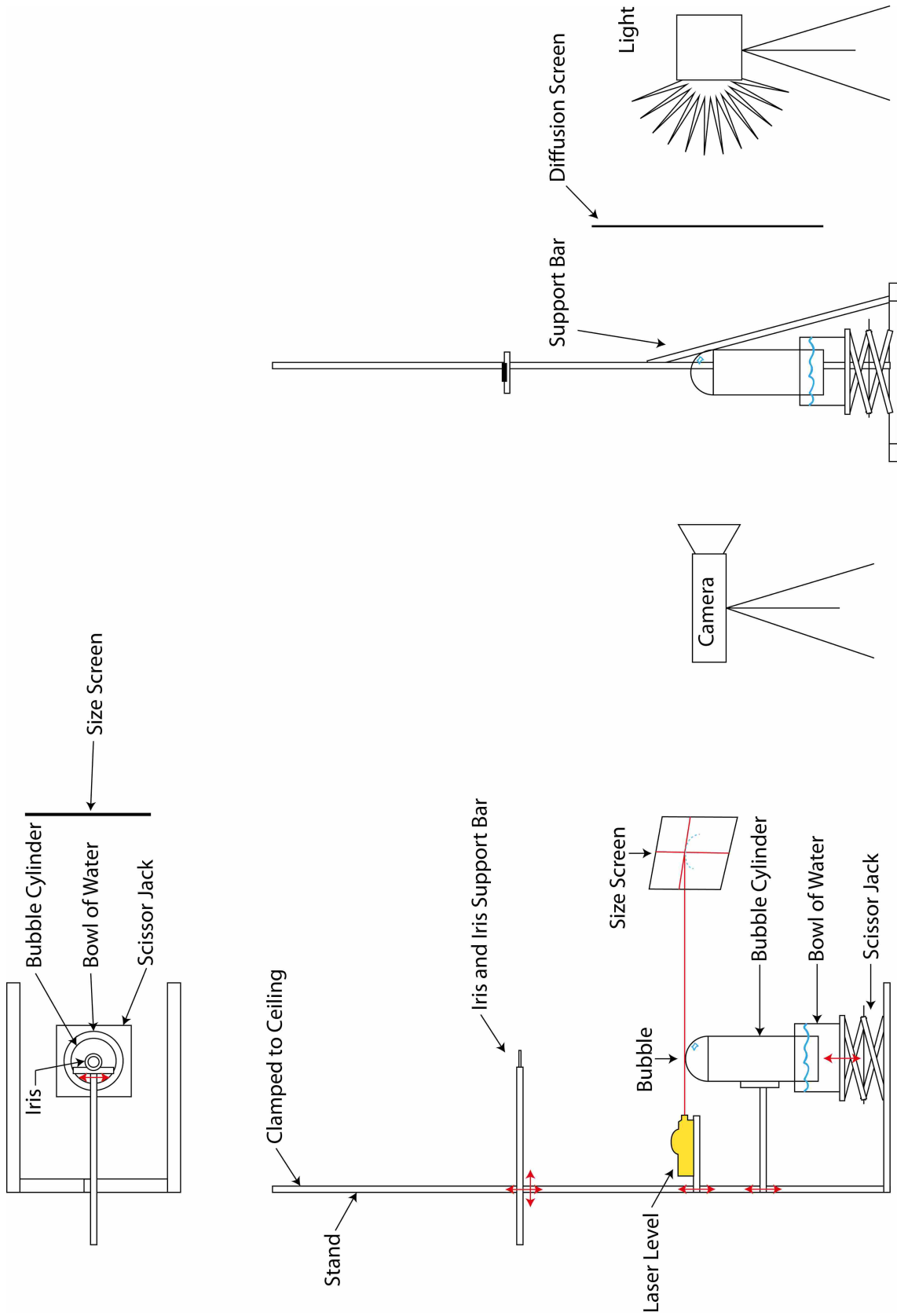


Figure 2.1: Experimental setup, the red arrows indicate directions of movements





(a) Overall view of the setup

(b) View of the setup for creating the lower half of the bubble

Figure 2.2: Photographs of the experimental setup

Images of the experiment were captured with a Photron Fastcam SA3 high speed camera. The camera was placed in front of the bubble cylinder and the lighting for the pictures was provided by a halogen lamp placed behind the cylinder. The light from the lamp was diffused through a piece of vellum placed between the bubble cylinder and the lamp.

### Ball Cleaning

To increase accuracy, consistency, and reproducibility of the results, the spheres used in the experiments were cleaned prior to each use. The cleaning process consisted of the following steps:

1. Retrieve the spheres from the bowl of water used to create the bubble and into which they fell after piercing the bubble. If the spheres were not used in any prior experiments step two was performed directly.

2. Dry the spheres with a microfiber towel.
3. Rinse the spheres in an 70 percent isopropyl alcohol bath.
4. Dry the spheres using a canned electronics duster. Note, the duster contained only tetrafluoroethane. A duster was used which contained another additive, but it was discovered that this duster contaminated the experiment, resulting in far more bubble ruptures than was otherwise the case.

The balls were handled only with gloved hands.

## 2.2 Experimental Variables and Parameters

### 2.2.1 Bubble Sizes

To be able to determine whether the size of the bubble was of any significance, the bubble sizes were varied. Five bubble sizes were used in this experiment and their radii and orientations are given below in Table 2.2.1.

Table 2.1: Bubble sizes for both top and bottom halves of the bubble.

Radius (m)	Upper Hemisphere	Lower Hemisphere
0.0150	Yes	Yes
0.0225	Yes	Yes
0.0375	Yes	Yes
0.0500	Yes	Yes
0.0625	Yes	No

As stated above, the bubble upper hemisphere were created using clear acrylic cylinders of the appropriate size. Only one cylinder per size was used. For the lower hemisphere of the bubble, the holes cut into the acrylic sheets (mentioned above) were cut to match the size of the corresponding cylinder; again, only one hole, per size, was used.

### 2.2.2 Ball Surface Measurements

These experiments were conducted using spheres of different sizes and materials. Four steel spheres, three glass spheres, two hollow aluminum spheres, and two billiard balls were used, see Figure 2.3. The diameter, mass, and wetting angle for each of these spheres are given in Table 2.2. The advancing contact angle for similar materials was assumed to be equal and diameter and mass values were averaged for each sphere size.



Figure 2.3: Picture of the different spheres used in the experiment

The wetting angle for each of the different types of materials was calculated using the sessile drop method. The spheres were placed on a table, on top of a washer (to hold them steady). The spheres were backlit with a light behind a diffuser. Then three to four drops of water were placed on the sphere using a pipette. After each drop a picture was taken of the sphere with the drop on it, see Figure 2.4. The pictures were taken with a Canon EOS 5D DSLR with a 100 mm macro lens. After three or four drops were placed on the sphere the drops were removed using the same pipette. Again, after each removal of water a picture was taken. The advancing and receding contact angles were then calculated from each image, and averaged to give the values in Table 2.2.

Table 2.2: Sphere property values, (mean  $\pm$  stdev [samples size]).

Material	Radius (mm)	Mass (g)	Advancing Contact Angle (deg)	Receding Contact Angle(deg)
Steel	12.7 $\pm$ 0.0 [5]	65.7 $\pm$ 0.05 [5]	45.2 $\pm$ 3.4 [4]	62.2 $\pm$ 8.6 [2]
Steel	11.9 $\pm$ 2.89e-3 [5]	5402 $\pm$ 0.84 [5]	45.2 $\pm$ 3.4 [4]	62.2 $\pm$ 8.6 [2]
Steel	11.1 $\pm$ 0.0 [5]	44.2 $\pm$ 0.0 [5]	45.2 $\pm$ 3.4 [4]	62.2 $\pm$ 8.6 [2]
Steel	8.7 $\pm$ 0.0 [5]	21.5 $\pm$ 0.42 [5]	45.2 $\pm$ 3.4 [4]	62.2 $\pm$ 8.6 [2]
Glass	4.8 $\pm$ 2.24e-3 [6]	1.1 $\pm$ 0.0 [6]	40.8 $\pm$ 6.9 [3]	73.5 $\pm$ 0 [1]
Glass	3.2 $\pm$ 0.0 [6]	0.3 $\pm$ 0.0 [6]	40.8 $\pm$ 6.9 [3]	73.5 $\pm$ 0 [1]
Glass	1.175 $\pm$ 0.0 [5]	1.707e-2 $\pm$ 0.0 [5]	40.8 $\pm$ 6.9 [3]	73.5 $\pm$ 0 [1]
Aluminum	9.4 $\pm$ 2.62e-2 [6]	2.4 $\pm$ 0.0 [6]	26.5 $\pm$ 4.1 [5]	49.2 $\pm$ 10.9 [4]
Aluminum	6.3 $\pm$ 0.0 [14]	0.7 $\pm$ 0.06 [14]	26.5 $\pm$ 4.1 [5]	49.2 $\pm$ 10.9 [4]
Billiard Ball	28.5 $\pm$ 0.0 [6]	183.9 $\pm$ 0.0 [6]	22.2 $\pm$ 10.2 [5]	52.4 $\pm$ 0.6 [3]
Billiard Ball	17.4 $\pm$ 1.51e-1 [1]	39.9 $\pm$ 0.926 [1]	26.9 $\pm$ 2.9 [4]	47.9 $\pm$ 10.8 [2]

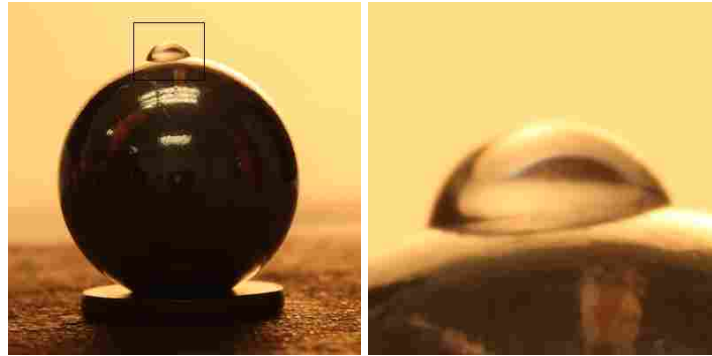


Figure 2.4: Sessile drop test example pictures. In this case the sphere is the 9.4 mm radius aluminum.

### 2.2.3 Bubble Thickness

In order to capture the interference patterns as outlined in 1.4.3 the bubble was backlit with monochromatic light provided by a HeNe laser pointer (max output  $<5\text{mW}$ ) with a stated wavelength of  $532\pm 10$  nm. In order to fully (or nearly fully) illuminate the bubble the laser was passed through a 532 nm 2-8X beam expander. The expander was placed 8.5 m in front of the bubble and 80-90 cm above the top of the bubble. It was realized, however, that the interference rings, though clearly visible to the eye were difficult to capture on film. This problem was solved

by shining the beam at a low angle of incidence to the film and to view the reflection of the beam off the soap film on a backdrop, see Figure 2.5.

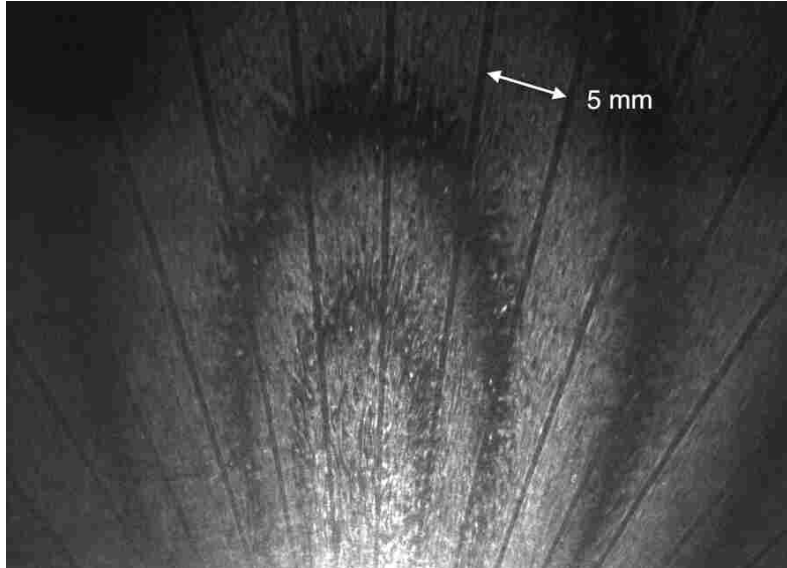


Figure 2.5: Example picture gauging the thickness of the bubble film. The dark arcs are the destructive interference rings on the bubble. Their distorted shape is a result of the projection of the bubble onto the screen. The 'fan' of dark lines are the reflection of the shadow cast by the 5 mm spaced screen, placed between the bubble and the laser.

The arcs in Figure 2.5 are the reflection of the interference rings on the bubble. Because the reflection distorted the circular interference rings into the elongated arcs it became necessary to find a way of judging the scale of the reflection. To do this we placed a transparency printed with 5 mm spaced vertical lines in the path of the laser beam, 30 cm in front of the center of the bubble. These lines then cast a shadow in the bubble which was then reflected onto the backdrop, giving a scale from which to judge the size and location of the interference rings. The general setup may be seen in Figure 2.6.

The draining rates of the fluid from the bubble were all recorded at 60 fps using the same high-speed camera used to capture the falling spheres. Three sets of images were recorded for each bubble size. Image recording started once the bubble reached the cylinder diameter and stopped once the film reached the newton black film state. This state is very recognizable as a dark circle which grows larger with time as seen in Figure 2.7.

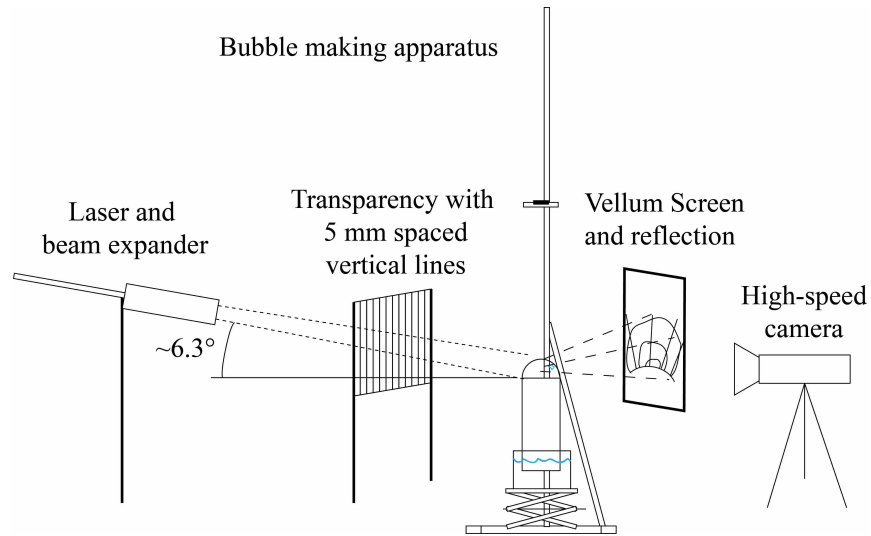


Figure 2.6: Experimental setup for determining bubble film thickness as a function of time.



(a) Beginning formulation of newton black film.



(b) Note the increase in size of the black film.

Figure 2.7: Newton black film example. The film is at the newton black film state in the center near the bottom both frames. Note the distinctive dark circle displayed by the film. The black film grows in time from image (a) to (b), 1.22 seconds later.

These image sets for each bubble size were processed to gather profile information for the bubble in time. The profile information is limited by the curvature of the bubble. The smaller bubble has a higher curvature and thus the reflection is more distorted. Because of this the profile information varies from 1.5 for the 0.015 m radius bubble, to 3.5 cm for the 0.05 cm radius bubble. These results are found in Figure 2.8.

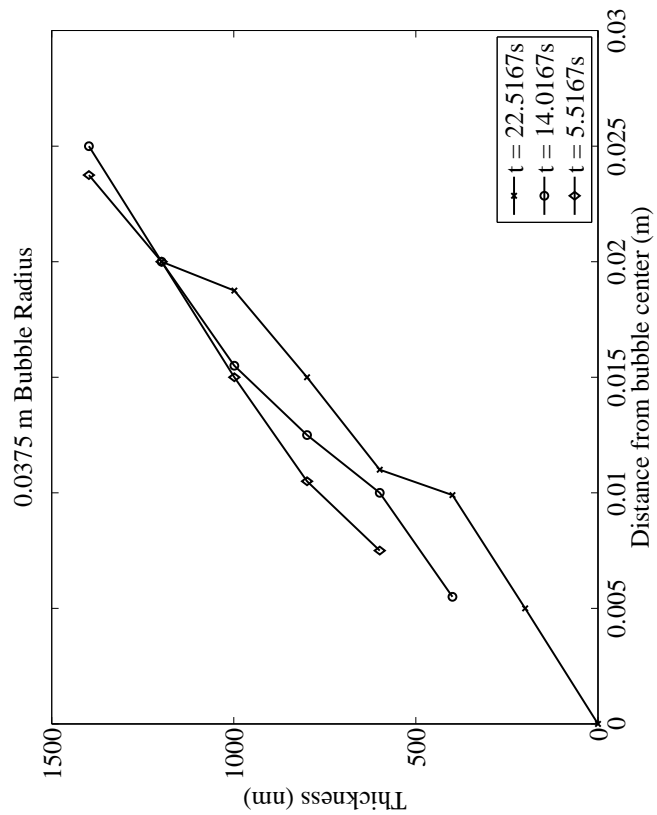
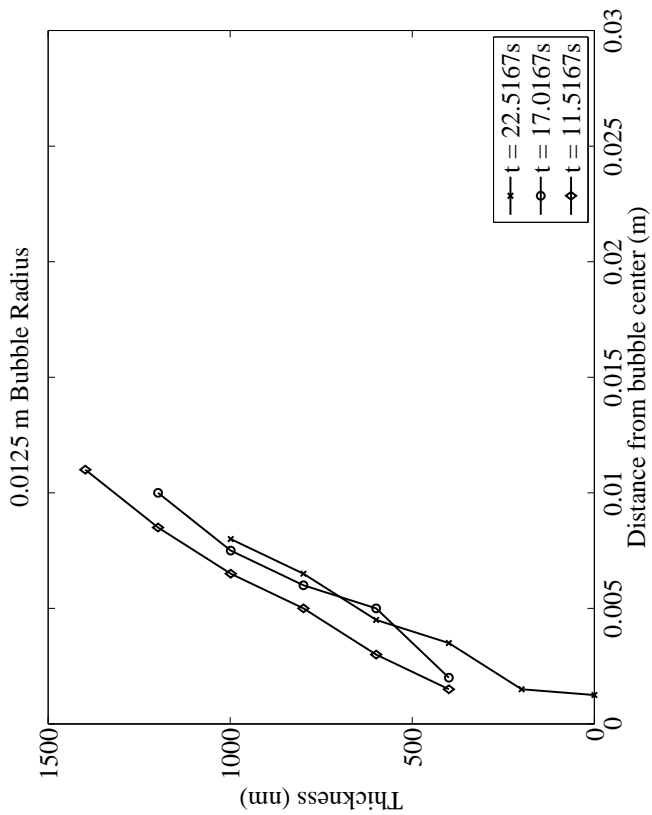
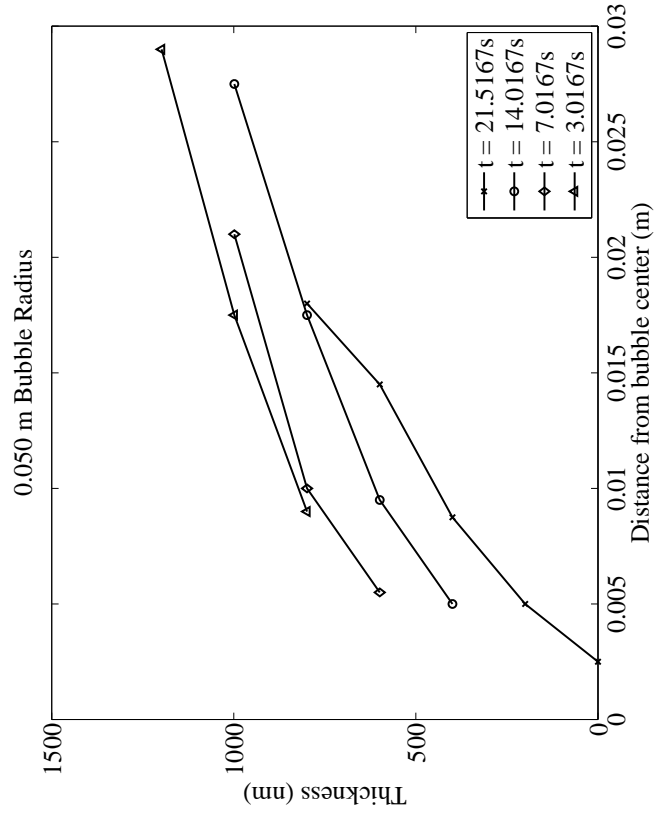
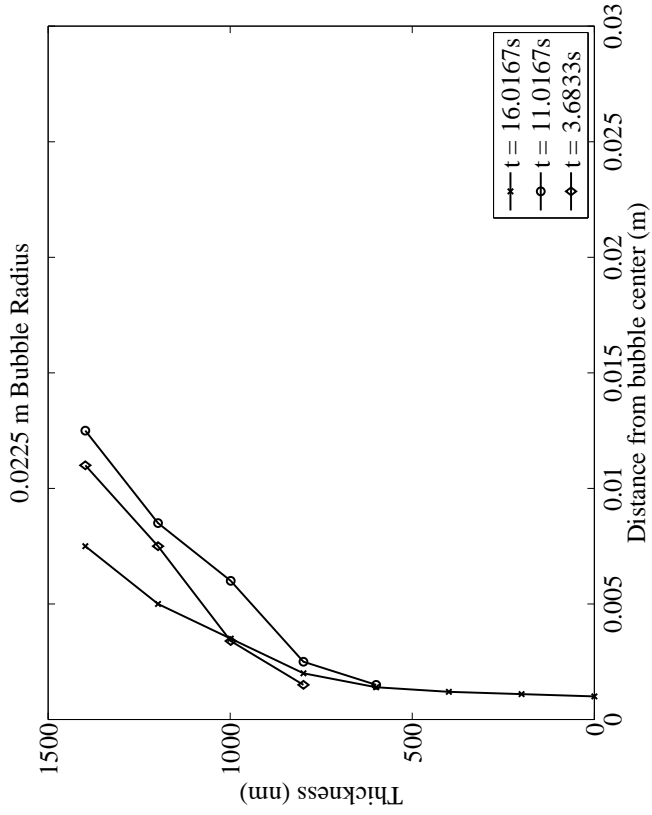


Figure 2.8: Bubble soap film drainage Profile examples. These plots have an accuracy of  $\pm 5$  nm for the thickness and  $\pm 0.5$  mm for the location.

The thickness calculated in Figure 2.8 were calculated at the destructive interference bands using Equation 1.2b. For these calculations the values of  $532 \pm 10$  nm and 1.332 were used for  $\lambda$  and  $n$  respectively. The variance in the wavelength,  $\lambda$  results in an uncertainty in thickness of  $\pm 3.8$  nm. Inaccuracy in locating the edge of the destructive interference fringes, due to camera resolution and noise, resulted in an uncertainty of  $\pm 0.25$  mm in the location of the thickness values on the bubble. The plots in Figure 2.8 each represent a single bubble drainage experiment.

From the results found in Figure 2.8, we may state a general observation that, in most cases, the bubble thickness at the time of sphere drop is at or above 600 nm. Indeed, this is a conservative statement since interference bands are very blurry for the first couple of seconds after bubble formation. This indicates that, though there do seem to be rings of set thicknesses, convection and other transport methods are moving a lot of fluid around during the first few moments after formation.

For the lower bubble half the fluid drains into the area of sphere-bubble collision, thus the thickness increases with time. Therefore, it is assumed that the thickness at the point of intersection is greater than one micron at all times.

#### **2.2.4 Soap Solution Measurements**

The soap film solution was created by mixing water and *Dawn Ultra Concentrated, original scent* dishwashing liquid at a 25 to 1 ratio. The viscosity of the mixture was calculated using an AR 2000 Rheometer. The viscosity of both the mixture and of water were measured using a stepped flow test. Figure 2.9 shows the results of these measurements.

The viscosity is somewhat larger than expected. Most texts state that water has a viscosity near  $1.002 \times 10^{-3}$   $Ns/m^2$  at 20°C, more than three times smaller than the calculated values. This discrepancy is most likely do to improper machine calibration or use. That said, the similarity between the viscosity of the water and the mixture should not come as a surprise. The mixture is 96% water by volume and the viscosity of the detergent is not much larger than water. Thus the effects of the detergents larger viscosity are negligible. Accordingly, all calculations involving viscosity and density came from tabulated values of water at 20 °C [35], see Table 2.3



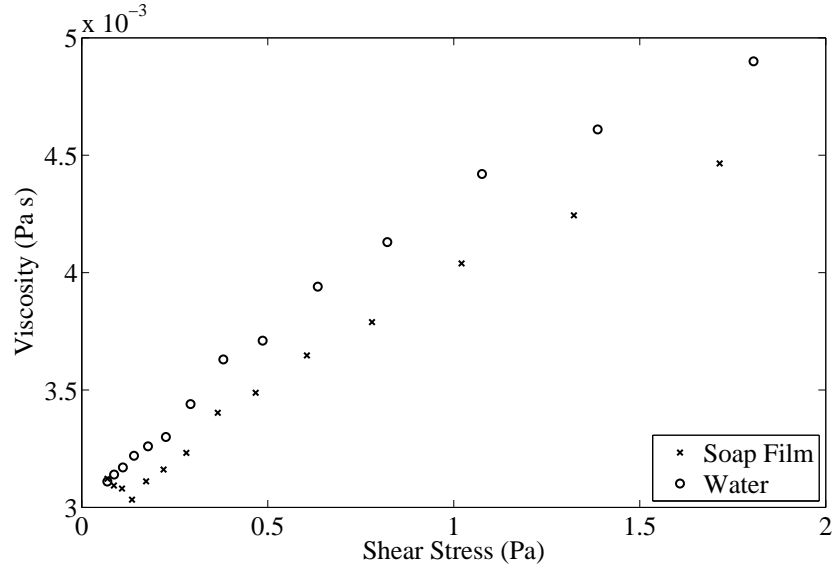


Figure 2.9: Results of the rheometry tests.

Table 2.3: Viscosity and density values used for soap film calculations.

Viscosity ( $Ns/m^2$ )	Density ( $kg/m^3$ )
1.002e-3	998.2

### Surface Tension Measurements

The surface tension was measured following the technique used by Jackson and Sleyman. They developed a very simple method utilizing the Laplace equation, see Equation (1.1), which shows that the radius and internal pressure of bubbles of different sizes are related via the surface tension of the fluid from which they are formed. Our method of recording the bubble size and pressure is similar to the method used by Jackson and Sleyman and a picture of the setup is seen below in Figure 2.10.

To create the bubble a syringe was connected to a glass bubble cylinder of radius 2.64 mm and to an incline manometer. A film was wiped onto the bubble cylinder via a gloved hand, as above, and the syringe was depressed to inflate the bubble. Once a bubble of desired size was created the gauge pressure was noted and a picture of the bubble was taken. The 1 cm square grid

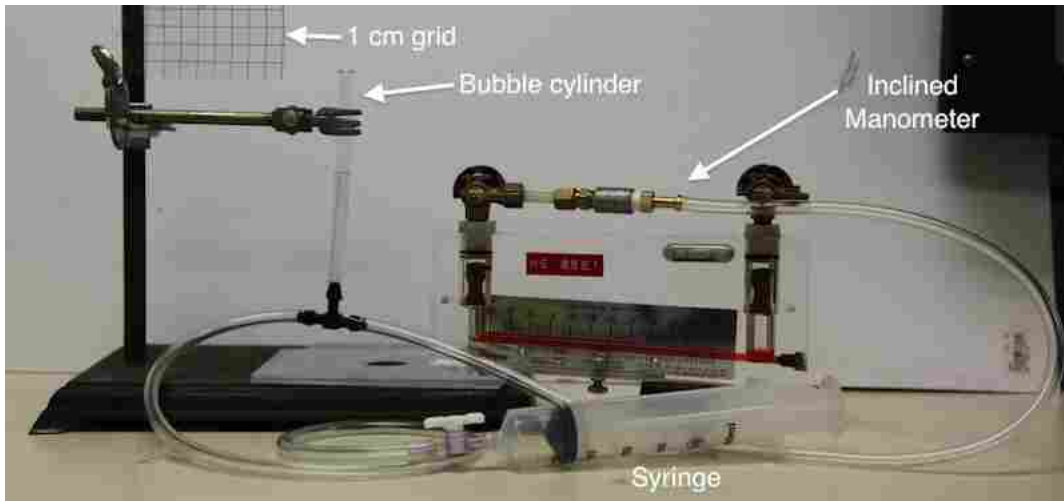


Figure 2.10: Setup of the surface tension measurement system.

next to the bubble cylinder seen in Figure 2.10 was also captured in an image and was used to calculate the size of the bubble. The data was used to create Figure 2.11, seen below.

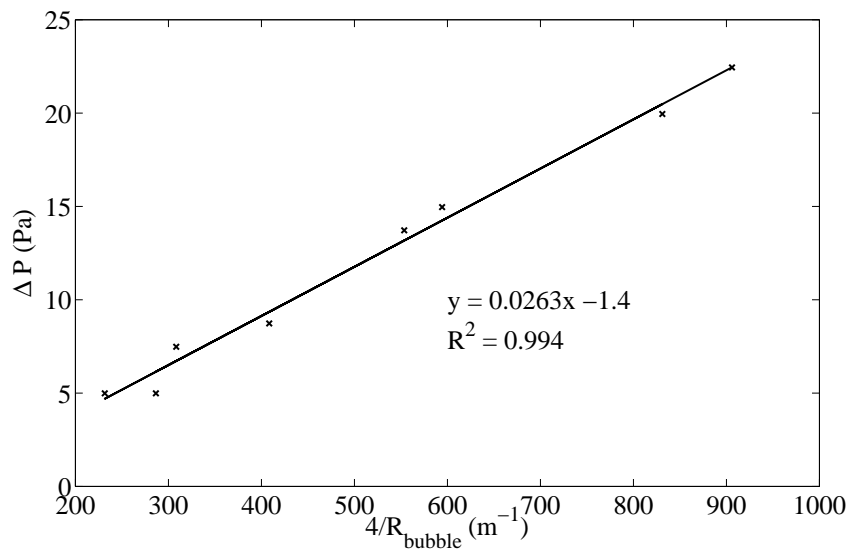


Figure 2.11: Plot of the experimental data for determining the surface tension. The slope of the best fit line represents the surface tension, so the surface tension  $\sigma = 0.0263 \pm 0.015 \text{ N/m}$ .

Taking the value of slope of the best fit line to the data as the surface tension yields a value of  $\sigma = 0.0263 \text{ N/m}$ . As this value is in good agreement with surface tension values calculated for other soap films, such as the film used by Jackson and Sleyman, we will use it in our calculations.

### **2.3 Conclusions**

This chapter outlined the methods used for the creation of soap bubbles of various sizes and for the dropping of spheres through those bubbles. Estimates for the draining of the soap film bubble are also given. Finally, the soap film solution was analyzed and its properties given, including surface tension, density, and viscosity.

The above mentioned methods and results were utilized to gather and analyze the experimental data discussed in the following chapters and the fluid properties given are the ones used in the calculations that follow.

## CHAPTER 3. EXPERIMENTAL RESULTS AND DISCUSSION

In this chapter we present the results of the experiment and explore some of their implications and significance. First we will present some interesting interactions between the bubble's soap film and the moving sphere. Next we will discuss where these phenomena occur and offer an explanation into their occurrence. Finally we will discuss popping criteria and offer 'best method' for sending a sphere through a bubble.

### 3.1 Regime Classification and Examples

Five distinct regimes appear when the sphere passes through the bubble membrane. These regimes are characterized by three main parameters: pinch-off order, deformation shape, and film bridge collapse.

At rest, surface tension forces form the soap film into its minimal surface. Once the film has reached a minimal surface it has reached an equilibrium state for the surface energy functional defining the film surface. As this surface is perturbed by the passing of the solid sphere that equilibrium is upset and the surface tension works to restore it.

#### 3.1.1 Pinch-off Order

As the sphere passes through the soap film forming the bubble the soap film wraps itself around the sphere and, if the bubble doesn't pop, the film reseals itself, usually in two places. This resealing will be referred to as the pinch-off and may occur in several ways.

1. **Bubble side pinch off.** The first type of pinch-off occurs when the film bridge connecting the sphere to the bubble pinches-off near the soap film first, see Figure 3.1(a).
2. **Simultaneous pinch off.** The second type of pinch-off occurs when the pinch-off near the soap film and the bubble occur at, or near, the same time, see Figure 3.1(b).

3. **Sphere side pinch off.** This final type of pinch-off occurs near the sphere first, then near the bubble soap film, see Figure 3.1(a).

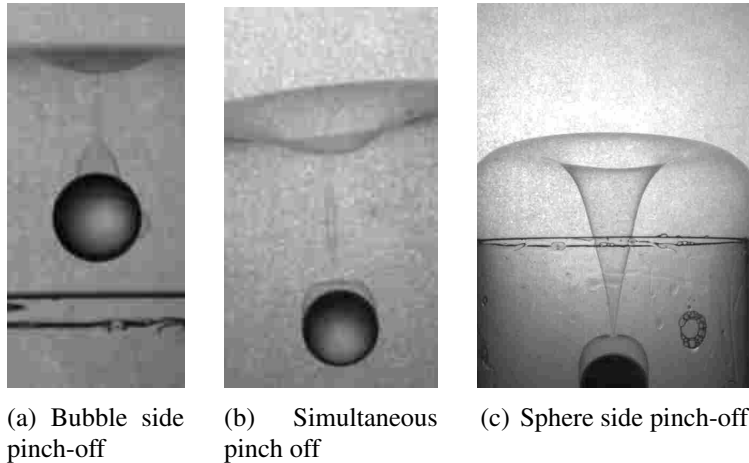


Figure 3.1: Pinch-off location examples. Each of these pictures come from the our experiments and represent the different pinch-off types.

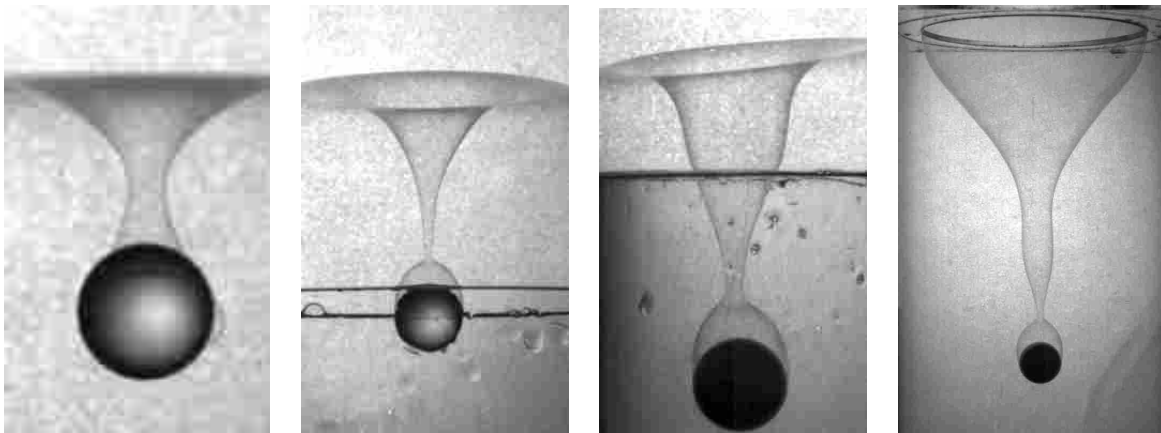
### 3.1.2 Film Bridge Shape Just Before Pinch-off

When a sphere passes through a soap film, the film must deform to allow that passage. As the film deforms to allow the passage of the sphere the ‘bridge’ linking the sphere to the bubble takes on several unique shapes:

1. **Catenary.** A catenary is the shape a chain makes when hanging between two fixed points. It was noticed that when the spheres were dropped from low heights the bridge linking the sphere to the bubble takes on the shape similar to that of a catenary. This shape was also noticed by Gilet and Bush in their paper discussing droplets bouncing on a soap film [36]. See Figure 3.2(a) for an example.
2. **Funnel.** This shape only occurs when pinch-off occurs sphere side first. Just before pinch-off, the soap film bridge connecting the bubble to the sphere takes on the shape of a funnel. This may be a simple conical type funnel, or a cone with a cylinder on top, see Figures 3.2(b) and 3.2(c).

3. **Elongated Funnel.** This final shape is very much like the funnel, except that the distance the sphere travels before pinch-off is much larger, see Figure 3.2(d). Note, this shape only occurs when a sphere is dropped through the lower hemisphere of a bubble.

Although shape (1) was remarked upon previously by Gilet and Bush in [36], film bridge shapes (2) and (3) are new to this study.



(a) Catenary shape example.

(b) Conical like funnel shape.

(c) Cone funnel, similar to a hopper.

(d) Elongated funnel.

Figure 3.2: Soap film bridge funnel type examples.

### 3.1.3 Film Bridge Collapse

In general, the collapse of a film bridge may be described by three parameters: necking, breaking, and relaxing [37] [21]. In this section we will focus on the necking stage. But, as the geometry and dynamics of our experiment involves more complex film dynamics than studied in [37] and [21], we will use the term collapse as a more appropriate term than necking.

1. **Bridge collapse.** The first form of collapse is essentially the same as that noticed by Cryer and Steen in their film collapse study [37]. The main characteristic of this collapse is the capture/formation of one or more satellite bubbles as a nearly cylindrical portion of the bridge collapses. These bubble are of relatively small size, on average their volume total volume is less than 5% the volume of the sphere falling through the bubble. This collapse

happens with pinch-off occurring at both locations nearly simultaneously or sphere side first. For examples see Figures 3.3 and 3.8.

2. **Bridge pinch-off.** The second type of collapse occurs only when pinch-off happens sphere side first. From this point the film bridge doesn't so much collapse, as the first example does, but the air in the bridge becomes mostly trapped by the bridge as the film necks and pinches-off near the bubble. Additional necking and pinch-off locations, forming additional bubbles, may also occur. In this case the total volume of the satellite bubbles is relatively large, averaging between 65% and 1.86% that of the sphere. For examples see Figures 3.10 and 3.12.

### 3.1.4 Regime Descriptions

Using the above descriptions for pinch-off and deformation shape we may accurately classify the interactions between the spheres and the bubble film. These classifications yield five distinct regimes for interactions between the falling spheres and the bubbles. Regimes (I)-(IV) occur in both the top and bottom halves of the bubble. Regime (V) occurs only within the bottom hemisphere of the bubble. A description of the regimes is given below. Additionally, one may refer to Table 3.1 for quick reference to the details of each regime.

- I. The first regime is characterized by a catenary deformation shape with pinch-off occurring first at the bubble side, then at the sphere side. The film bridge collapses, forming up to one satellite bubble. An example of this is seen in Figures 3.3 and 3.5.
- II. The second regime has the same catenary deformation shape as the first, but pinch-off occurs simultaneously at both the bubble and sphere side. Again, the film bridge collapses, forming up to one satellite bubble, see Figures 3.6 and 3.7.
- III. In regime three the bridge takes on the funnel shape, generally only the cone type funnel is noticed. Pinch-off occurs sphere side first and the film bridge collapses, creating one or more, up to five were recorded, bubbles forming during collapse, see Figures 3.8 and 3.9.
- IV. The fourth regime is defined by the funnel shape with the hopper type funnel usually forming, though some instances of cone like funnels were recorded. Pinch-off occurring sphere side

first and the film bridge is then pinched-off. The pinched-off bridge may collapse further, as discussed above, resulting in up to seven satellite bubbles, see Figure 3.10 and 3.11..

- V. Regime five is characterized in much the same way as the hopper funnel shape is characterized above in IV, only in this case the funnel is much longer, with necking occurring bubble side before sphere side pinch-off has taken place. Additionally, total bubble volumes in this regime are typically larger, reaching up to 330% the volume of the passing sphere. This regime is only found occurring in the bottom hemisphere of the bubble (see Figure 3.12).

It is interesting to note that in all cases a bubble is formed on top of the moving sphere, see, for example Figures 3.3, 3.6, and 3.8, frames (L), (L), and (I) respectively. This will be discussed further in Section 4.1.



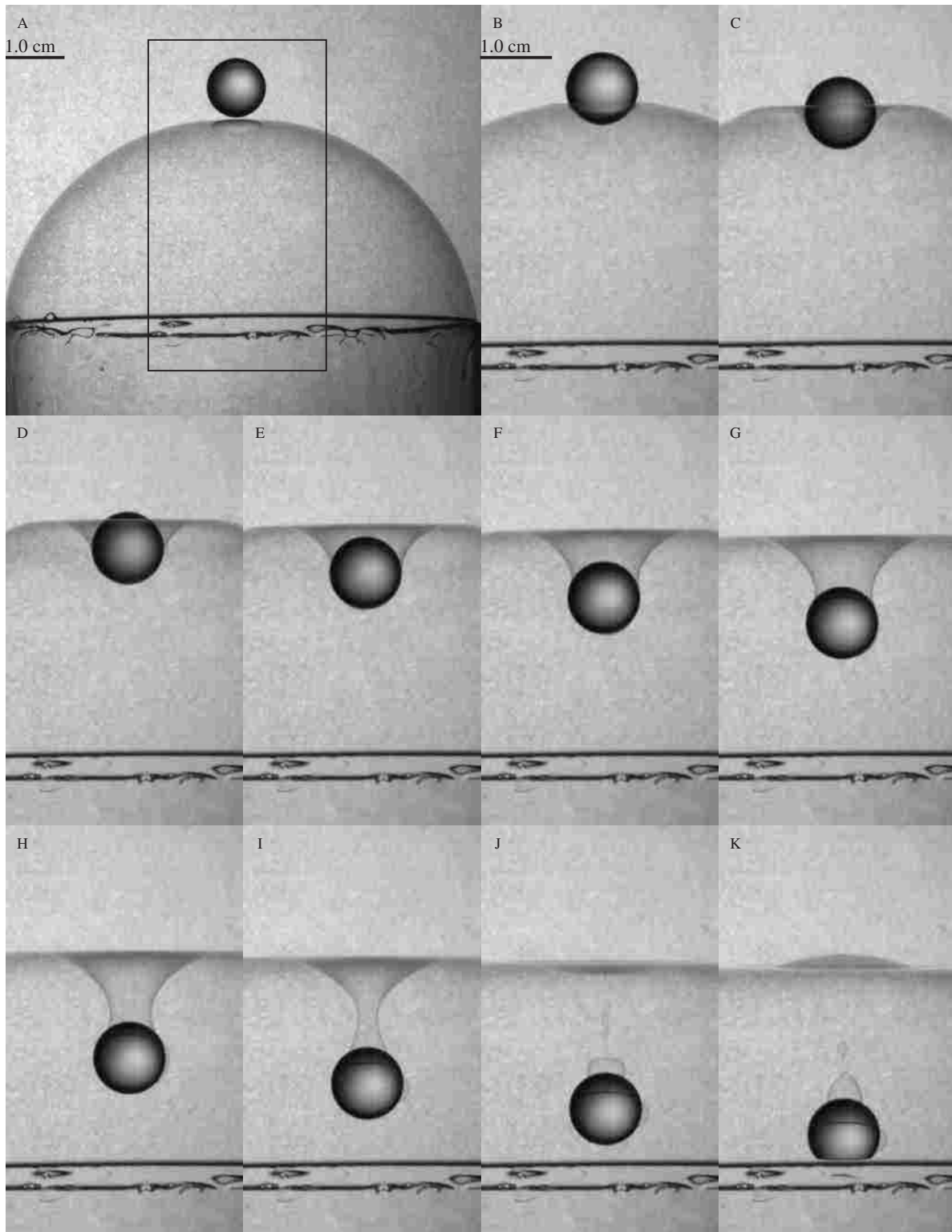


Figure 3.3: Type (I) regime example. A 0.48 cm radius glass sphere dropped from 23.5 cm above the top of a 3.75 cm radius bubble. The shape is catenary and pinch-off order is bubble side first, sphere side second. Notice the catenary shape develop as the glass sphere interacts with the soap film, especially in frame (I). Both pinch-off locations occur between frames (I) and (J), see Figure 3.4 for greater detail. Frames are 1.5 ms apart.

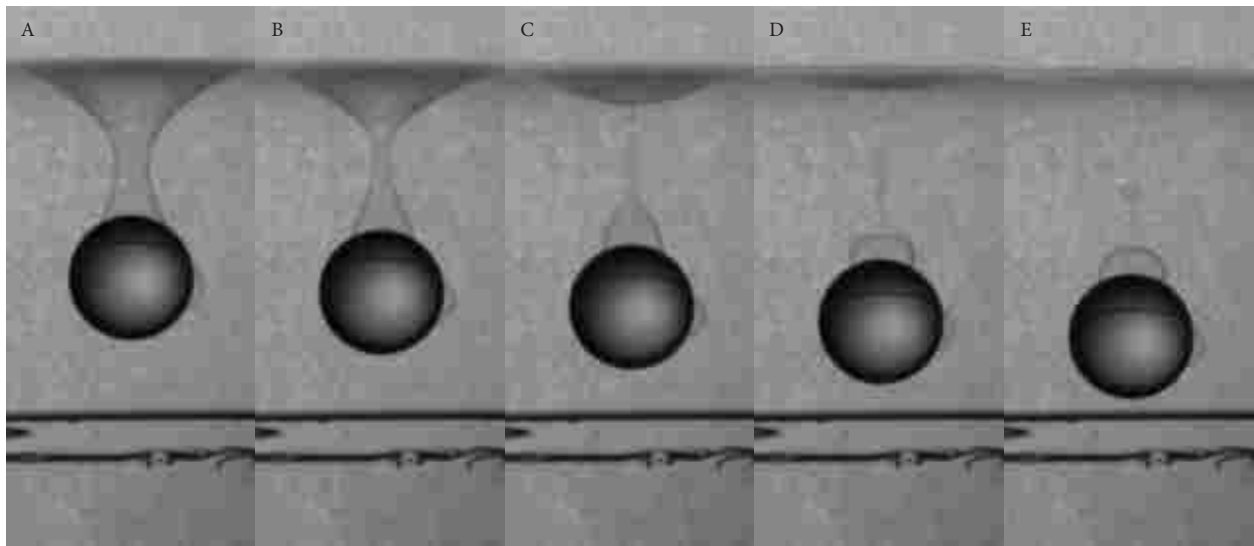


Figure 3.4: This set of pictures displays what happens between frames (I) and (K) of Figure 3.3, only with frames 0.5 ms apart. This figure clearly shows pinch-off occurring first near the bubble (frame (C)).

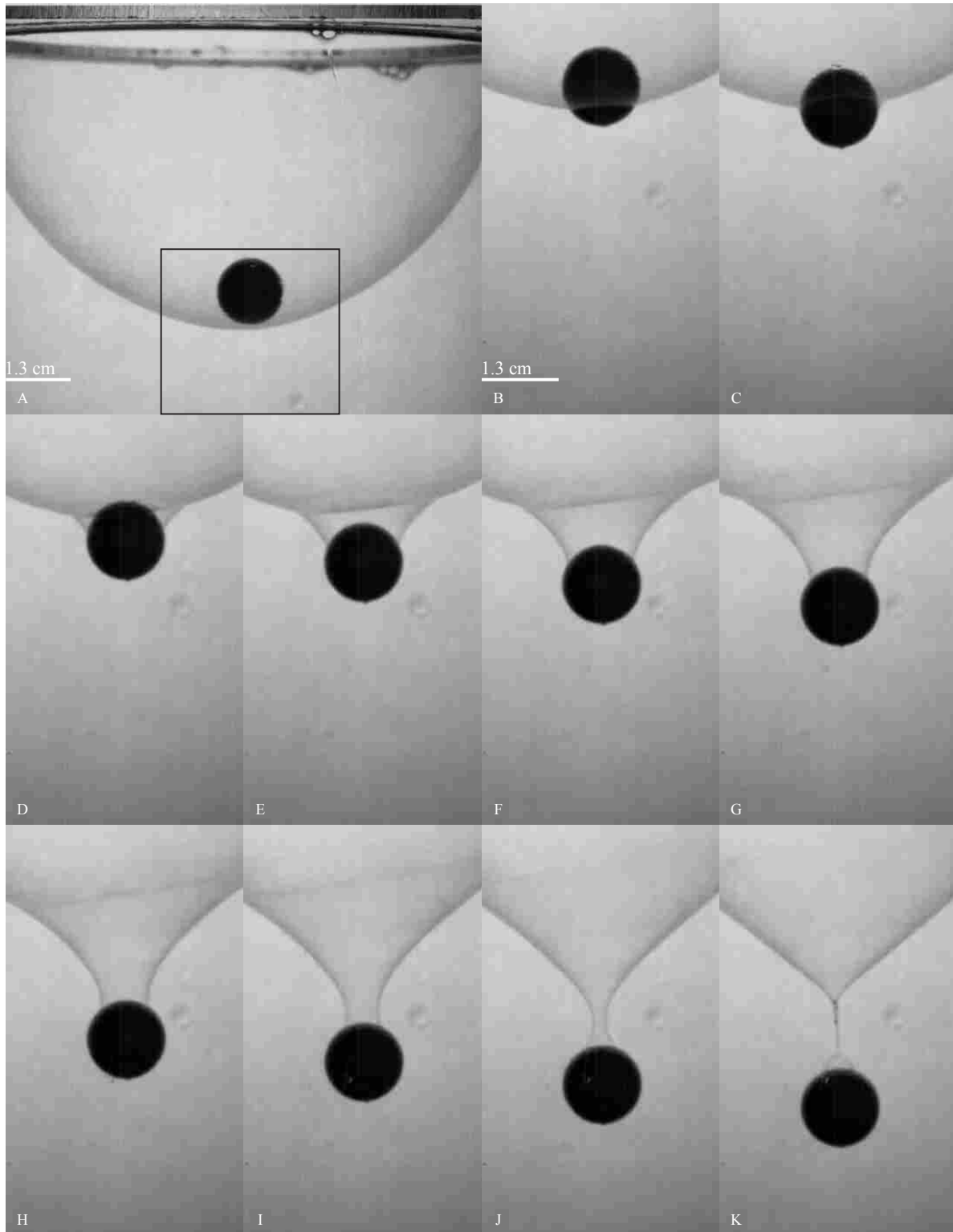


Figure 3.5: A 0.63 cm radius aluminum sphere dropped from 15 cm above the bottom hemisphere of a 5.0 cm radius bubble. This is a type (I) regime exhibiting a catenary shape with pinch-off order occurring bubble side first then bridge collapse (see frame(K)). Note the lack of a satellite bubble. Though not always the case, this is due to the amount of liquid flowing to the bottom of the bubble (i.e. drainage). Frames are 2.0 ms apart.

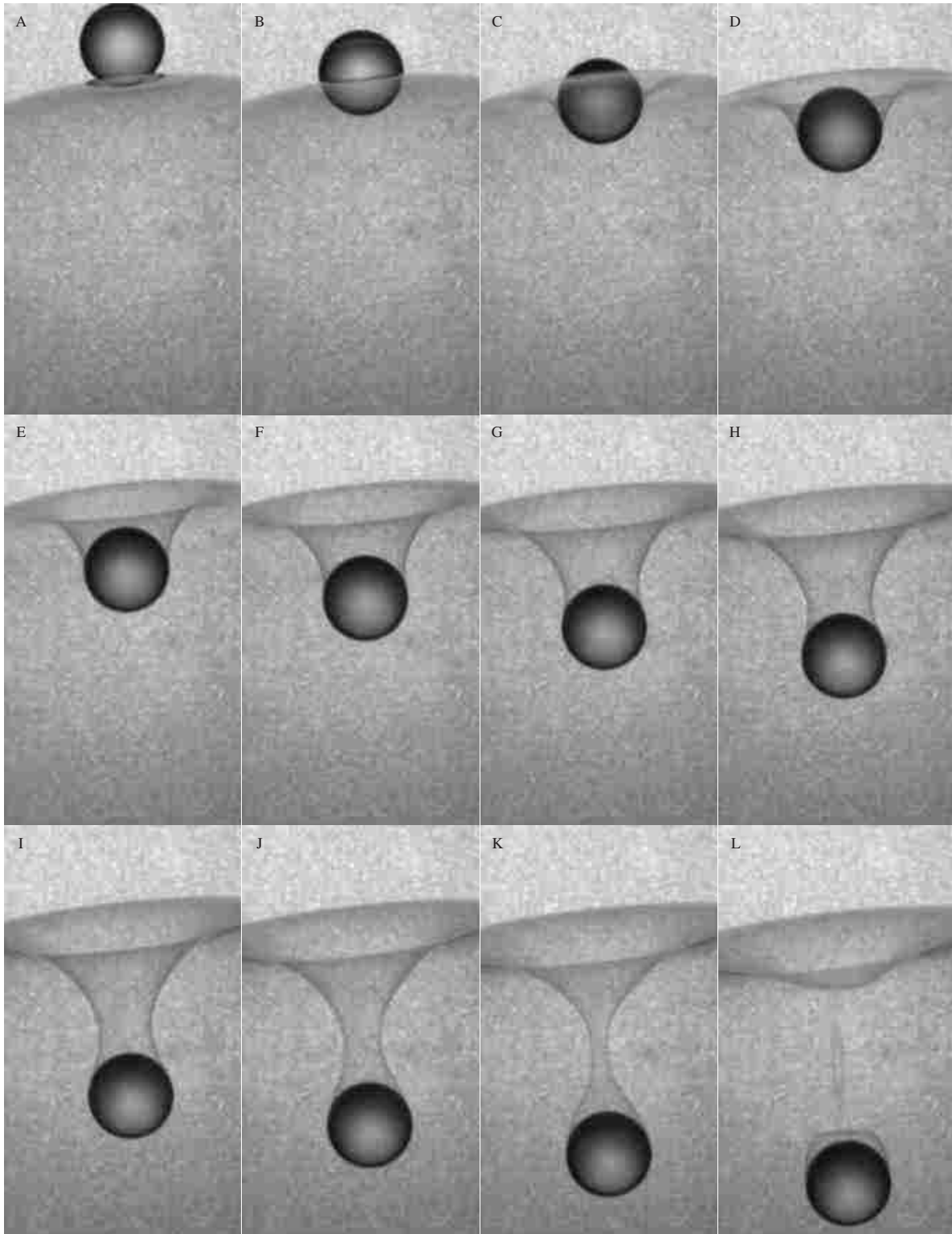


Figure 3.6: A 0.48 cm radius glass sphere dropped from 51.5 cm above the top of a 5.0 cm radius bubble. For this type (II) regime the shape is catenary and pinch-off order is simultaneous. Notice that a similar catenary shape develops as in the first regime, especially in frame (J). Both pinch-off locations occur between frames (K) and (L). For increased temporal resolution in the last frames, an overall view was not given. Frames are 0.67 ms apart.

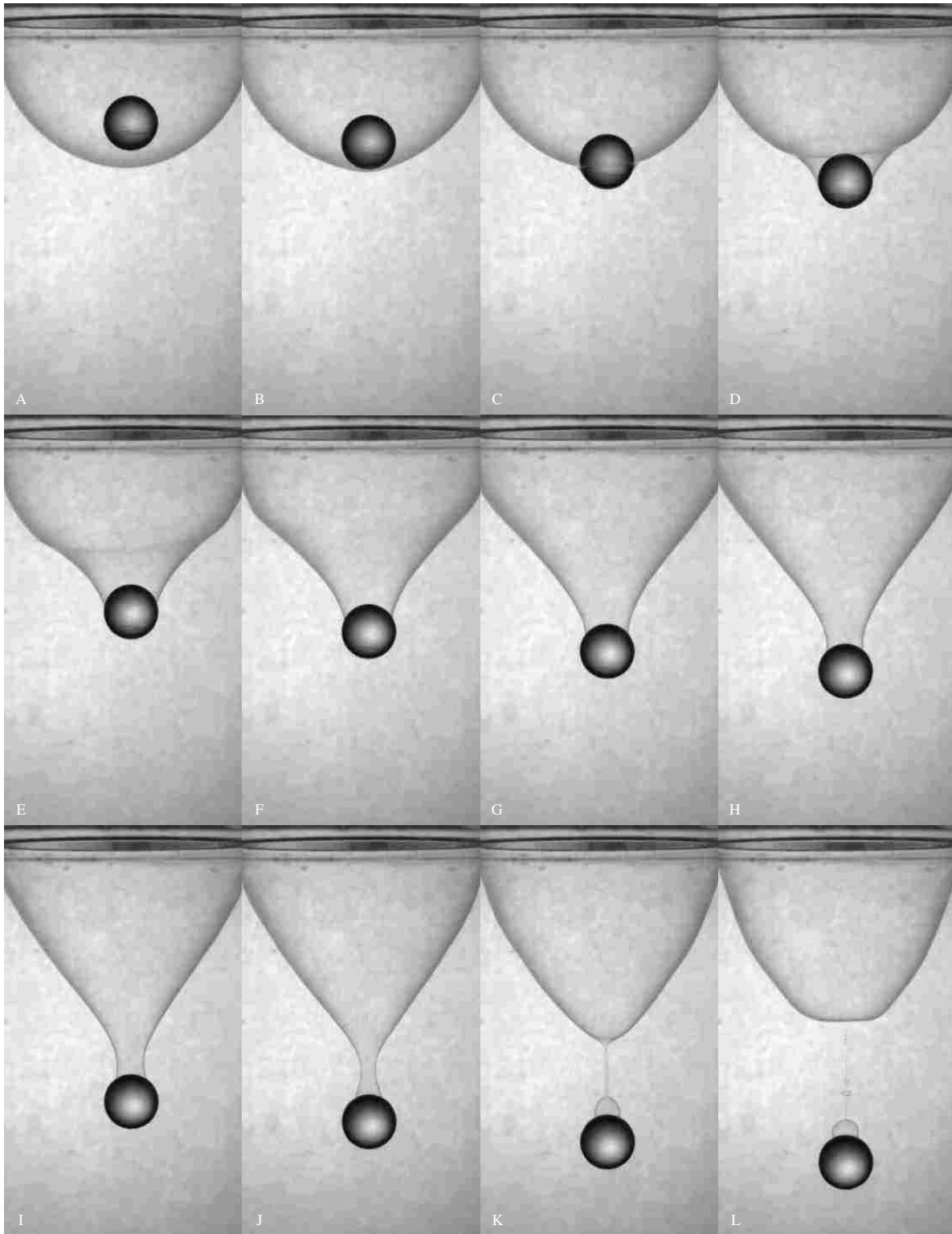


Figure 3.7: A 0.48 cm radius glass sphere dropped from 25.7 cm above the bottom hemisphere of a 2.25 cm radius bubble. This type (II) regime is defined by its catenary shape, simultaneous pinch-off order and the collapse of the film bridge. Note in frame (L) that, along with two satellite bubbles, a column of water droplets are seen indicating the presence of additional fluid as seen in the last case. Frames are 1.5 ms apart.

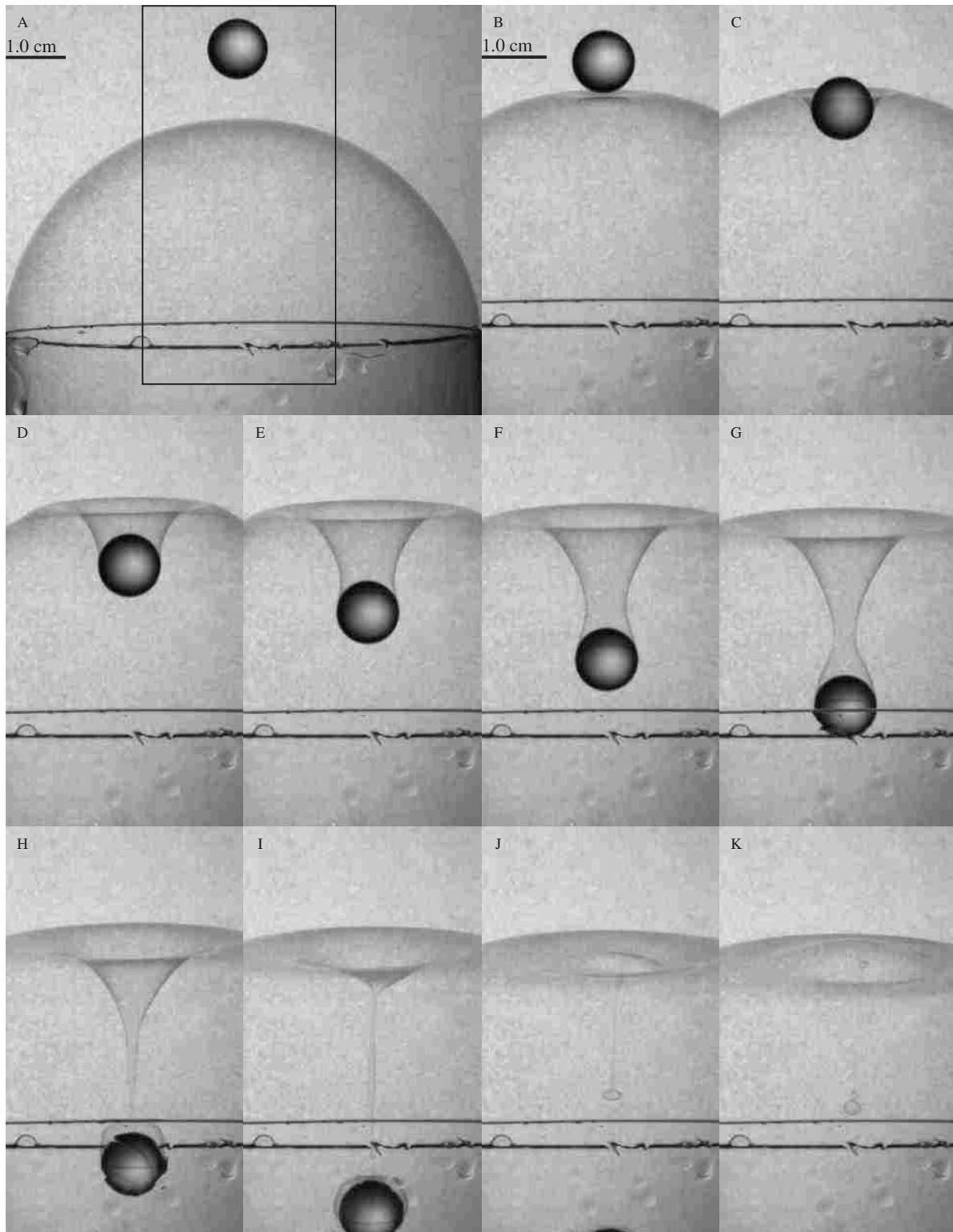


Figure 3.8: Example of regime type (III). 0.48 cm radius glass sphere dropped from 113.9 cm above the top of a 3.75 cm radius bubble. This is a cone funnel shape with pinch-off occurring sphere side first. A key characteristic of this regime is the quick collapse of the film bridge after pinch-off, see frames (H) and (I). Also note the relatively small satellite bubble. Frames are 1.5 ms apart.

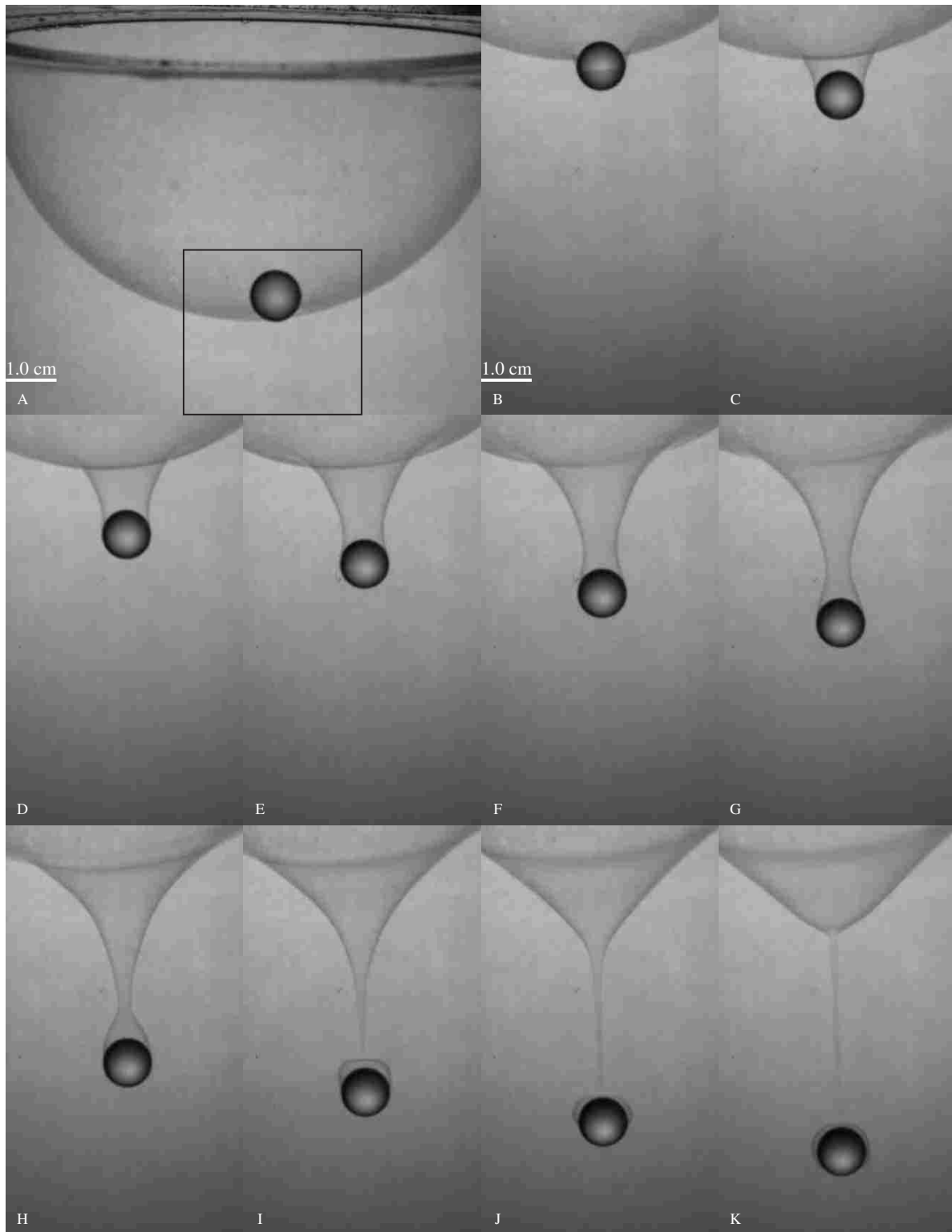


Figure 3.9: A 0.48 cm radius glass sphere dropped from 90.3 cm above the bottom hemisphere of a 5.0 cm radius bubble. This type (III) regime is characterized by its cone-like shape, sphere side first pinch-off order, and film bridge collapse. Frames are 1.33 ms apart.



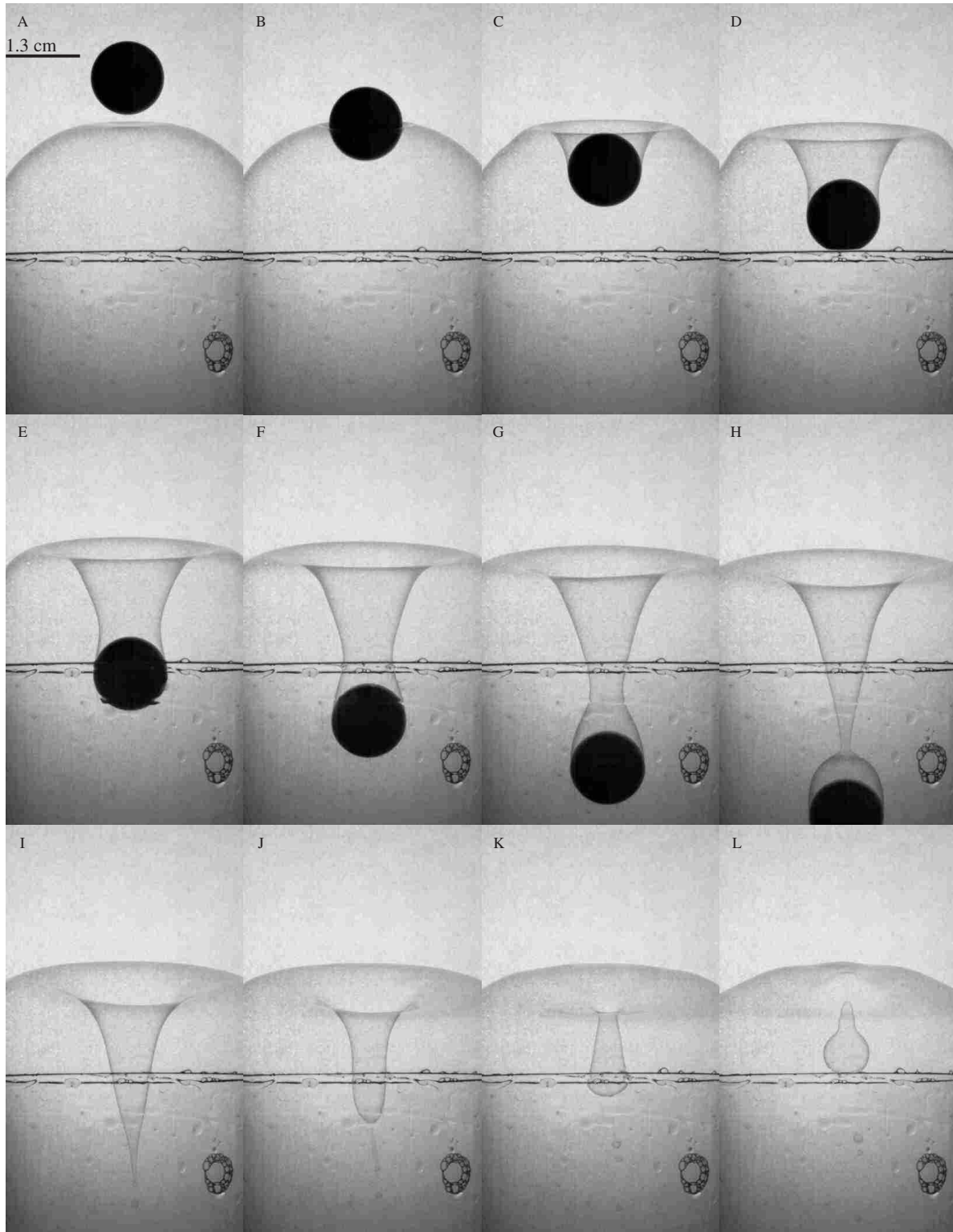


Figure 3.10: A 0.94 cm radius aluminum sphere dropped from 113.9 cm above the top of a 3.75 cm radius bubble. In this type (IV) the film is distorted into a hopper funnel shape and pinch-off occurs sphere side first. Notice that the disturbed film does not collapse in on itself after sphere pinch-off, as it does in Figure 3.8. Instead, the funnel stays open, frames (I) - (K), until the bubble side pinch-off occurs, capturing a large satellite bubble, frame (L). Frames are 2.5 ms apart.



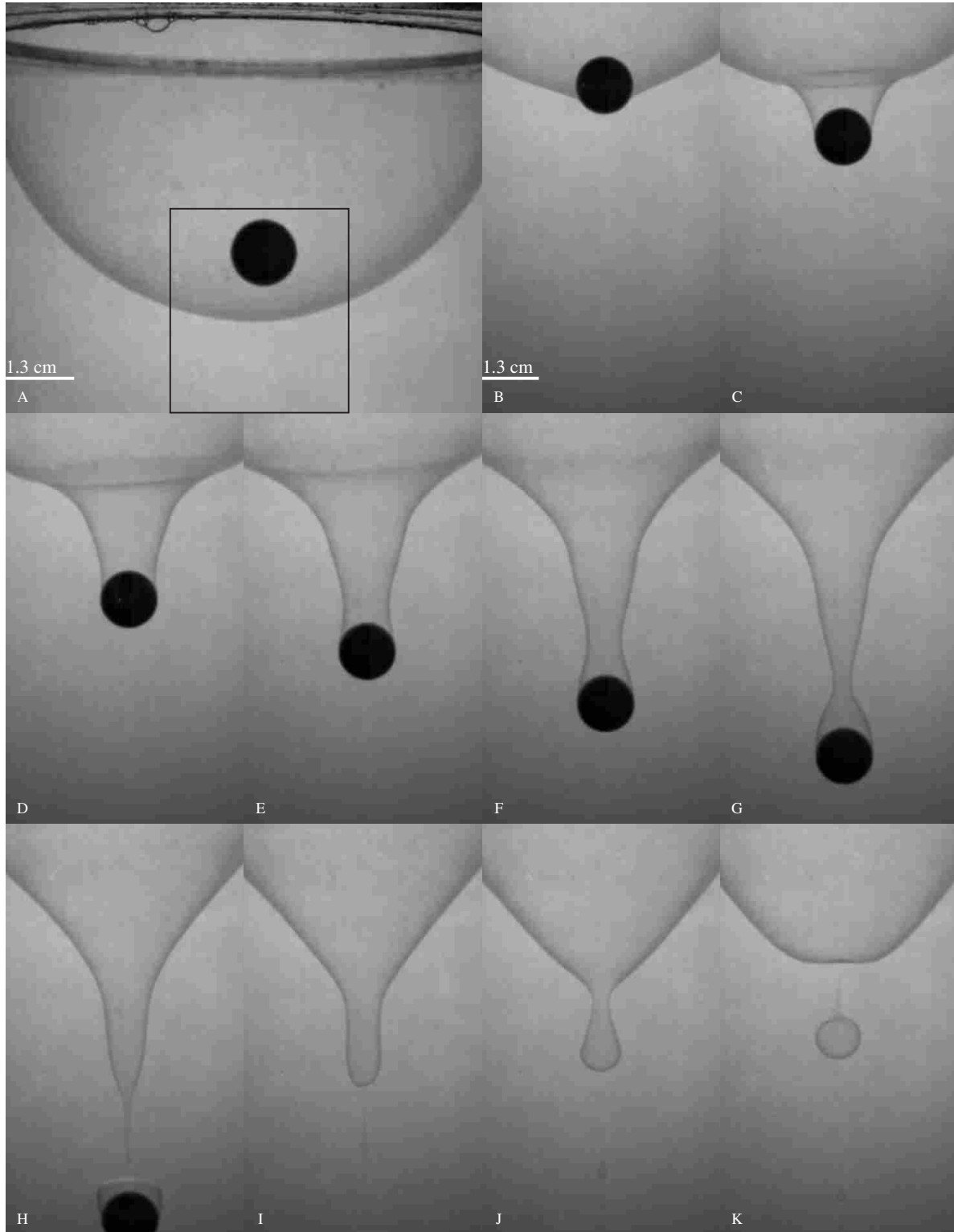


Figure 3.11: A 0.63 cm radius aluminum sphere dropped from 94.0 cm above the bottom hemisphere of a 5.0 cm radius bubble. This type (IV) regime displays a hopper bridge shape with pinch-off occurring sphere side first. The film bridge pinches-off and captures a relatively large satellite bubble (see frame K). Frames are 2.67 ms apart.

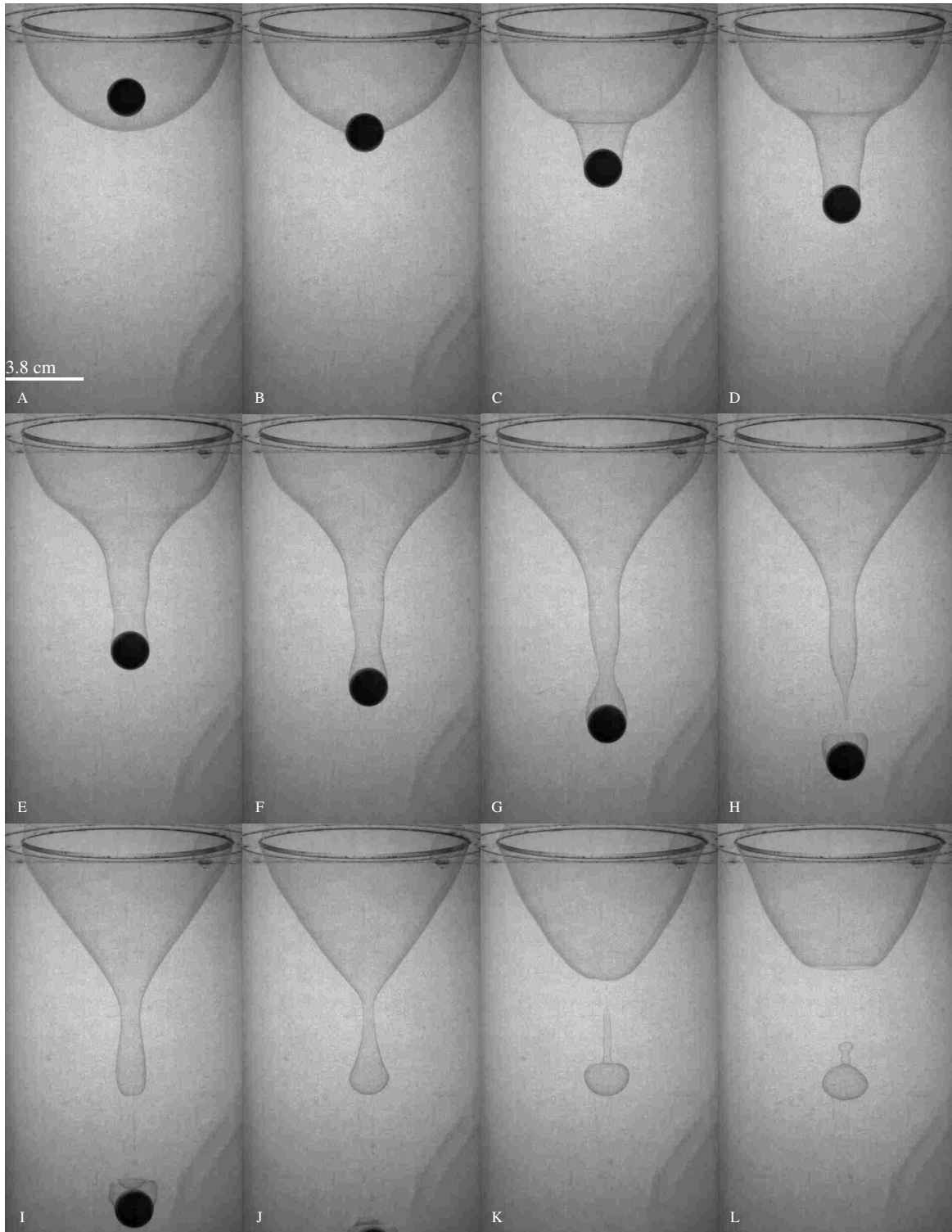
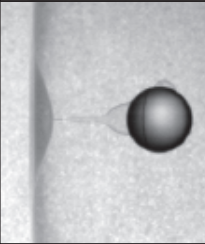
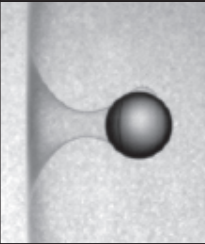
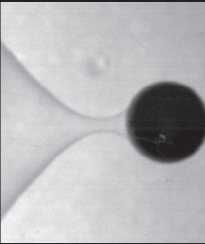
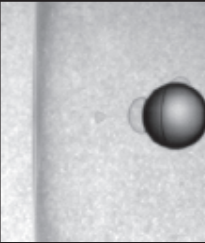
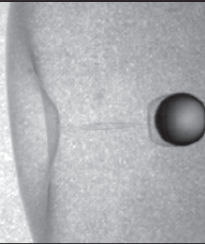
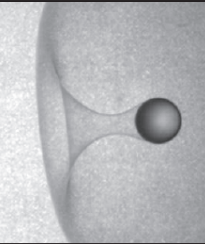
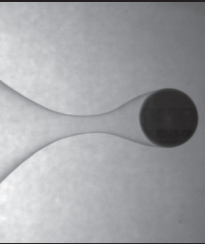
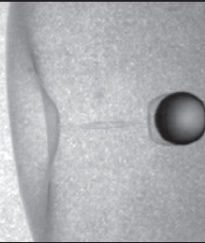
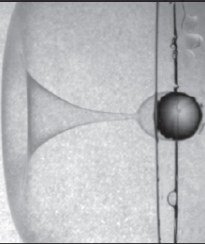
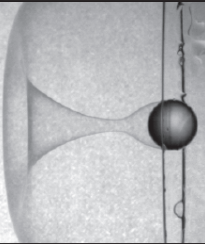
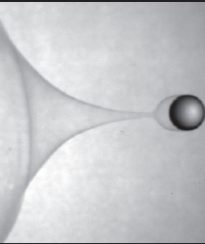
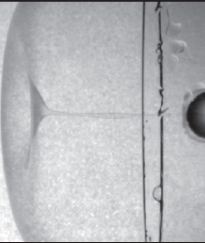
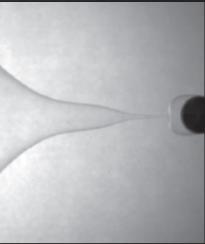
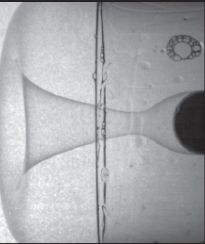
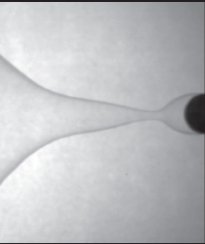
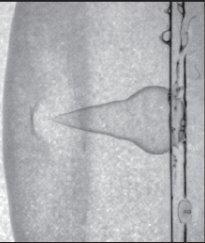
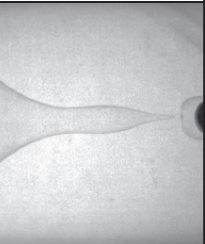


Figure 3.12: A 0.94 cm radius aluminum sphere dropped from 95.0 cm above the bottom hemisphere of a 5.0 cm radius bubble. This final regime, type (V), occurs only when spheres fall through the lower hemisphere of the bubble. The regime is defined by its elongated hopper shape and sphere side pinch-off order. The film bridge pinches-off, resulting in a large satellite bubble. Note that not only is the funnel shape elongated, but that the time the film takes to pinch-off the sphere has also increased in comparison to the hopper funnel type described above. Frames are 4.0 ms apart.

Table 3.1: Chart of regimes with example pictures of their definitions and the Weber numbers defining their creation.

Regime Number	Regime Description	Photographic Examples				Weber number Upper/ Weber number Lower
		Pinch-off	Bridge shape - Upper	Bridge shape - Lower	Collapse	
I	Characterized by a catenary deformation shape with pinch-off occurring first at the bubble side, then at the sphere side. The film bridge collapses, forming up to one satellite bubble.					$We_U < 1650$ $We_L < 708$
II	Characterized by the catenary deformation shape only with pinch-off occurring nearly simultaneously. The film bridge collapses, forming up to one satellite bubble.					$1650 < We_U < 3170$ $708 < We_L < 2650$
III	In this regime the bridge takes on the funnel shape, generally only the cone type funnel is noticed. Pinch-off occurs sphere side first and the film bridge collapses, creating one or more, up to five were recorded, bubbles forming during collapse.					$3070 < We_U < 6090$ $2650 < We_L < 3380$
IV	This regime is characterized by a hopper like shape, though some instances of cone were recorded. Pinch-off occurs sphere side first and the film bridge is pinched-off. The pinched-off bridge may collapse further, resulting in up to seven satellite bubbles.					$We_U > 6090$ $3380 < We_L < 6310$
V	Regime five is characterized by an elongated hopper shape and sphere side pinch-off. Total bubble volumes for this regime are typically larger, as much as 330% the volume of the passing sphere.		N/A		N/A	$We_L > 6310$

### **A short discussion of the regime type image sequences**

In Figure 3.3 we see a 0.48 cm radius glass sphere passing through the upper hemisphere of a 3.75 cm radius bubble. The sphere was dropped from 23.5 cm above the top of the soap bubble. In frame (A) we see an overall view of the setup, with the sphere just above the soap film. Frames (B) through (K) are enlargements of the indicated area. In frames (B) - (F) we see the development of the film bridge into a catenoid shape, with full development of the shape by frame (G). Note the disturbance wave caused by the sphere's contact with the soap film in frame (C). In frames (G) - (I) we see further elongation of the film bridge. By frame (J) the film bridge has pinched-off, leaving a satellite bubble forming just above the sphere, and another bubble attached to the top of the sphere. Note that by frame (K) the satellite bubble is starting to take on a spherical shape. Finally, notice the smaller attached bubble on the right side of the sphere in frames (I) - (K). This bubble is formed by the entrainment of the air forming the boundary layer surrounding the falling sphere.

Figure 3.5 shows the development of the same regime as Figure 3.3, but for the lower hemisphere of a 5.0 cm radius bubble and a 0.63 cm radius aluminum sphere. The sphere was dropped from 15 cm above the bottom of the hemisphere. As in Figure 3.3, frame (A) provides an overall view of the setup with the sphere just above the soap film. Frames (B) - (H) show the development of the film bridge into a catenary shape, with clear shape distinction by frame (I). Frames (I) and (J) show further elongation and development of the film bridge. By frame (K) the film bridge has pinched-off, with the formation of an attached bubble on top of the falling sphere. Note, however, the lack of a satellite bubble and the presence of a stream of film droplets. The cause of this is the greater film thickness in the lower hemisphere, due to the internal film drainage discussed above in Chapter 1.

Figure 3.6 begins with a 0.48 cm radius glass sphere already touching the soap film, with film disturbance clearly seen just under the sphere (frame A). The sphere was dropped from 51.5 cm above the top of a 5.0 cm radius upper hemisphere bubble. As seen above, we see the development of the film bridge and its catenoid shape in frames (B) - (F) with clear shape development by frame (G) and further stretching of the bridge continuing through frame (K). Note, however, the greater elongation of the film bridge by the final frame before pinch-off, frame (K), as com-

pared to the elongation in frame (I) of Figure 3.3. Frame (L) depicts the simultaneous pinch-off, an elongated satellite bubble, and a bubble attached to the falling sphere.

We see in Figure 3.7 a 0.48 cm radius glass sphere falling through the lower hemisphere of a 2.25 cm radius bubble. The sphere was dropped 25.7 cm above the lowest surface of the film. The size of the bubble allows us to obtain an overall view in every frame. We see the usual development of the film bridge in frames (A) - (H), with a clear catenary shape by frame (I). This shape develops and elongates further in frame (J). Frame (K) shows the film bridge just before the simultaneous pinch-off. Not the nearly columnar shape of the bridge at that point. In frame (N), while we see the typical bubble formed on top of the falling sphere, we also see that two satellite bubbles have been created, a deviation from what has happened in the examples mentioned above.

The photo sequence in Figure 3.8 illustrates the development of a type III regime. The sequence was created with a 0.48 cm glass sphere being dropped 113.9 cm above the top of the upper hemisphere of a 3.75 cm radius bubble. Frame (A) gives an overall view of the setup with the sphere just above the soap film. Frame (B) shows the sphere still above the film, however, the film has been disturbed by the surrounding fluid moving out of the way of the moving sphere. Frames (C)-(E) show the development of the film bridge, forming a catenary like shape by frame (E). This shape quickly becomes distorted in frames (F) and (G), with the shape becoming very cone like by frame (H). Frame (H) also shows the formation of the typical bubble attached to the top of the sphere. However, note that the bubble's edges are wrapped down the side of the sphere, as apposed to resting on top of the sphere. Additionally, note the downward movement of the bubble's lower edge in frame (I) and continued in frame (J). This is due to the boundary layer surrounding the moving sphere preventing wetting of the sphere surface, and is discussed in greater detail in section 4.1. We also see in frame (I) the collapse of the film bridge with pinch-off already having occurred sphere side, and progressing bubble side. Frames (J) and (K) show the creation of three satellite bubbles, two near the top of the cylinder and one near the bubble film. We also see the response of the soap film following the two pinch-offs, see frames (J) and (K).

Figure 3.9 shows the development of regime type III, formed by a 0.48 cm radius glass sphere falling through the lower hemisphere of a 5.0 cm radius bubble. The sphere was dropped from 90.3 cm above the bottom of the bubble hemisphere. Frame (A) gives an overall view, with catenary film bridge shape being developed in frames (B) through (D). Frames (E) through (H)

show elongation of the bridge, with clear deviation from the catenary shape. By frame (H) the film bridge begins to become cone like, with a very steep cone being formed by frame (I). Pinch-off occurs by frame (J), while the bridge collapses in frames (J) and (K). Again we see in frames (I) through (K) the formation of the bubble on the top of the sphere and the bubbles movement down the sides of the sphere.

Figure 3.10, shows our first example including film bridge pinch-off. Frame (A) shows the 0.94 cm radius aluminum sphere just above the upper hemisphere of a 3.75 cm radius bubble. The sphere was dropped from a height of 113.9 cm above the top of the bubble's film. Again we see the bubble distortion of the by the potential effects of the falling sphere. Frames (B) through (H) show the development of the film bridge. Note, however, that the bridge shape never seems to take on the classic catenary shape noticed in all the examples above. Rather, we see a sharp distortion of the film bridge just above the sphere in frame (D) and moving further and further away in frames (E) through (G). Also note the large distortion of the bubble's film in frames (C) through (H) as the film responds to the sphere's movement. Sphere side pinch-off occurs between frames (H) and (I). We notice that frames (I) through (K) show the air exiting the film bridge at the same time that the top of the bridge moves to pinch-off. Pinch-off of the film occurs bubble side by frame (L), with the formation of a satellite bubble of larger size than those seen in the above examples.

Figure 3.11 shows a 0.63 cm radius aluminum sphere falling through the lower hemisphere of a 5.0 cm radius bubble. The sphere was dropped from 94.0 cm above the bottom of the hemisphere. Frame (A) provides an overall view of the experiment. Frames (B) through (G) show the development of the hopper shape film bridge. Again note the lack of catenary shape. Pinch-off occurs sphere side in frame (H), and an intermediate pinch-off also occurs in frame (I), forming a single satellite bubble. The film bridge empties out some of its entrained air in frames (I) and (J), until bridge pinch-off occurs between frames (J) and (K). Again, note the larger size of the satellite bubble formed by frame (K).

The final photo sequence (Figure 3.12) was formed by a 0.94 cm radius aluminum sphere dropped through the lower hemisphere of a 5.0 cm radius bubble. The sphere was dropped from 95.0 cm above the bottom of the bubble. We observe bridge development in frames (A) through (H). Pinch-off occurs bubble side frame (H). Again, note a secondary pinch-off occurring by frame (I), creating satellite bubbles, with a final bridge pinch-off occurring in frame (K). The distinguish-

ing characteristic of this regime from the last is the extremely large satellite bubble(s) formed from the film bridge pinch-off.

### 3.2 Discussion of the Regimes

The regimes noted above are separated by the Weber number of the falling sphere, which we will define as:

$$We = \frac{\rho u^2 r}{\sigma} \quad (3.1)$$

where  $\rho$  is the density of the fluid,  $u$  is the velocity of the sphere at impact,  $r$  is the radius of the sphere, and  $\sigma$  is the surface tension of the fluid. To calculate of the falling sphere we used the recorded drop height and the equation:

$$u = \sqrt{2gh} \quad (3.2)$$

where  $g$  is the gravitational constant and  $h$  is the height above the bubble surface from which the sphere was dropped. Although this may not yield exact velocities, the results are accurate enough for the present purposes.

Figures 3.13 and 3.14 show the regimes displayed as a function of Weber number vs  $r/R$ , where  $R$  is the bubble radius. The non-dimensional number  $r/R$  was chosen as it indicates a relative scale of the sphere to bubble sizes. This is an important ratio as it demonstrates one limit to the successful passing of a sphere through a bubble. For example, it is no surprise that a sphere is unable to pass through a bubble of equal size. Thus an  $r/R$  value of one indicates an upper limit to successful entry and exit of a sphere through a bubble.

Horizontal lines in Figures 3.13 and 3.14 separate the regimes discussed above and show the dependance of each regime on Weber number. The Weber number ranges during which each of the regimes was notice are in Tables 3.2 and 3.3. Note that their limiting values are the values for which the horizontal lines in the figures are plotted. These values were calculated by averaging the highest Weber number in the lower regime with the lowest Weber number in the higher regime. For example, the first transition line in for the upper hemisphere of the bubble bubble was found by

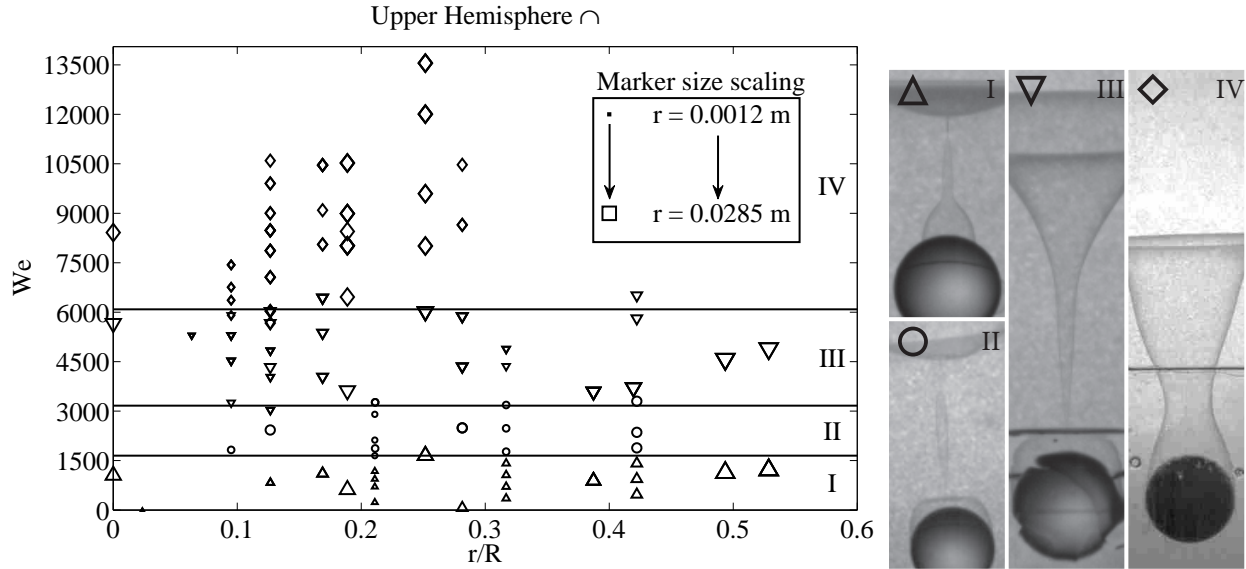


Figure 3.13: Regime diagram showing the dependence of the film bridge shape, pinch-off order and collapse as the spheres were dropped through the upper half of the bubble. Upward pointing triangles, circles, downward pointing triangles, and diamonds indicate the four regimes, as described previously. Note the case with  $r/R$  near zero. This case was produced by dropping the larger aluminum sphere through a flat film, thus approximating a bubble of infinite radius. For calculations a radius of 5,000 cm was used. Marker size indicates the size of sphere dropped, e.g. larger spheres have larger markers, smaller spheres have smaller markers.

averaging the highest Weber number in regime (I) with the lowest Weber number in regime (II).

Table 3.2: Limiting Weber numbers for each regime, upper hemisphere.

Regime	Weber Number Range
I	$We < 1650$
II	$1650 < We < 3170$
III	$3170 < We < 6090$
IV	$We > 6090$

It should be noted that only one data point exists in regime I for the lower hemisphere (Figures 3.14 and 3.16). It is believed that this is due to the difficulty of obtaining data with such a low Weber number in the lower hemisphere (a result from the experimental setup), rather than a deviation from the complete Weber number dependence of the regimes.



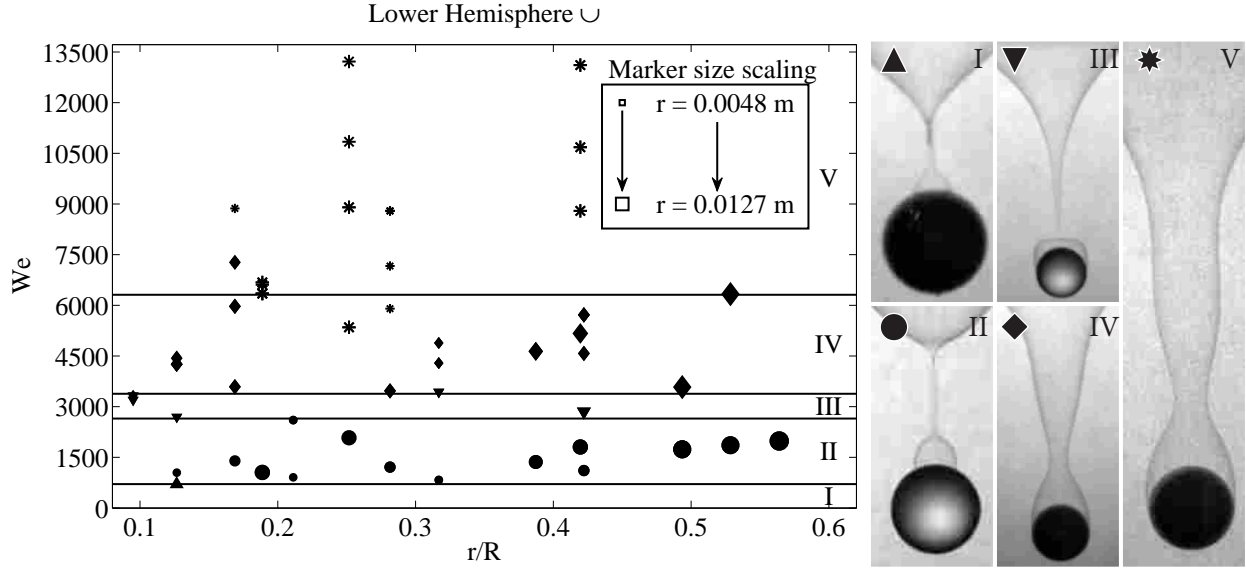


Figure 3.14: Regime diagram showing the dependence of the film bridge shape, pinch-off order and collapse as the spheres were dropped through the lower half of the bubble. Upward pointing triangles, circles, downward pointing triangles, diamonds, and asterisks indicate the five regimes noticed for the lower bubble half, as shown at the right respectively. Markers are filled to further indicate downward bubble orientation. Marker size indicates the size of sphere dropped, e.g. larger spheres have larger markers, smaller spheres have smaller markers.

Table 3.3: Limiting Weber numbers for each regime, lower hemisphere.

Regime	Weber Number Range
I	$We < 708$
II	$708 < We < 2650$
III	$2650 < We < 3380$
IV	$3380 < We < 6310$
V	$We > 6310$

Another potential choice for plotting against the Weber number is the bond number, defined as:

$$Bo = \frac{gr^2\rho}{\sigma} \quad (3.3)$$

where  $g$  is the gravitational constant, and the other variables are defined as before. Figures 3.15 shows Weber number vs. bond number for the upper hemisphere while Figure 3.16 shows the lower cases.

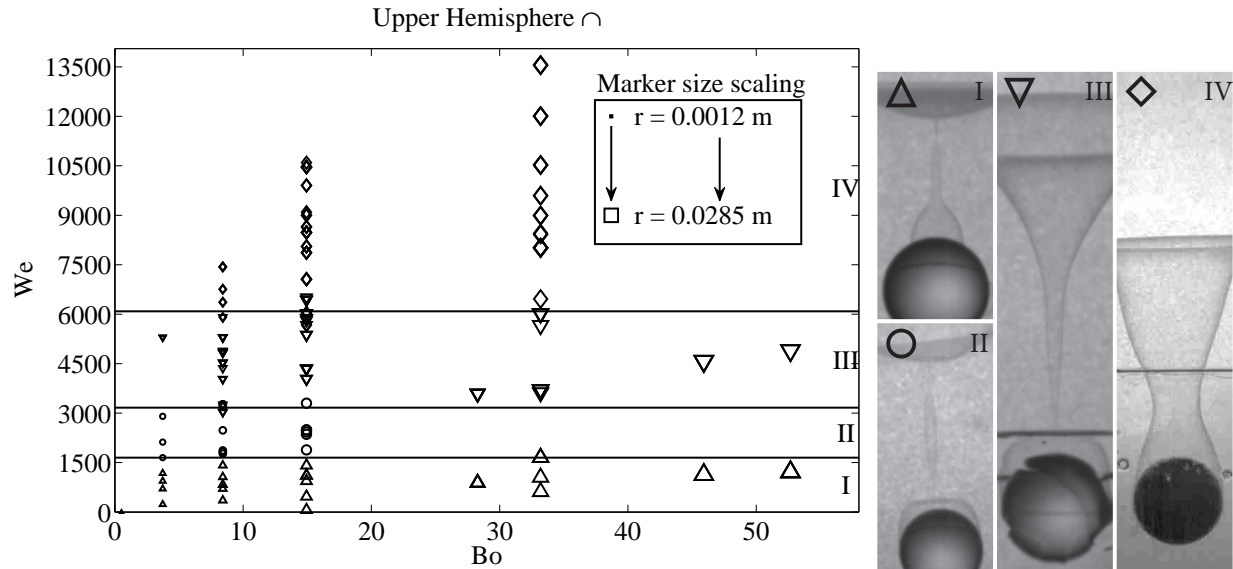


Figure 3.15: Regimes plotted Weber vs Bond number, for the upper half of the bubble. Notice that the regimes span nearly a century of bond numbers. Upward pointing triangles, circles, downward pointing triangles, and diamonds indicate the four regimes, as described respectively. Marker size indicate size of sphere dropped, e.g. larger spheres have larger markers, smaller spheres have smaller markers.

Note how in both cases, more than a half century of bond numbers are spanned and the regimes are still displayed in their appropriate locations. However, there is an interesting lack of the higher regimes found in both the low and high bond number cases and are missing for separate and unrelated reasons. A Lower bond numbers indicate a smaller sphere radius. Smaller sphere radii results in a smaller Weber number, the only important number when finding a regime, it appears, and thus the need to drop the sphere from a higher height becomes necessary. This height quickly becomes prohibitive. For example, to enter regime IV, in the upper hemisphere, the smallest sphere would needed to have been dropped from a height of over 70 meters, neglecting drag forces. To even enter regime II would require a drop height of nearly 19 meters. Thus for bond numbers less than 10, reaching the upper regimes is difficult using the current system.

The reason the upper regimes are not evident in the higher bond numbers is also due to the radius of the sphere, but for a different reason. As the sphere moves through the film, the film is displaced and stretched. A larger sphere, of necessity, requires more stretching to allow that sphere to pass through. However, the film is of finite thickness and will rupture when it thins too much. Since the higher numbered regimes require more surface area, in a per radius view (meaning that

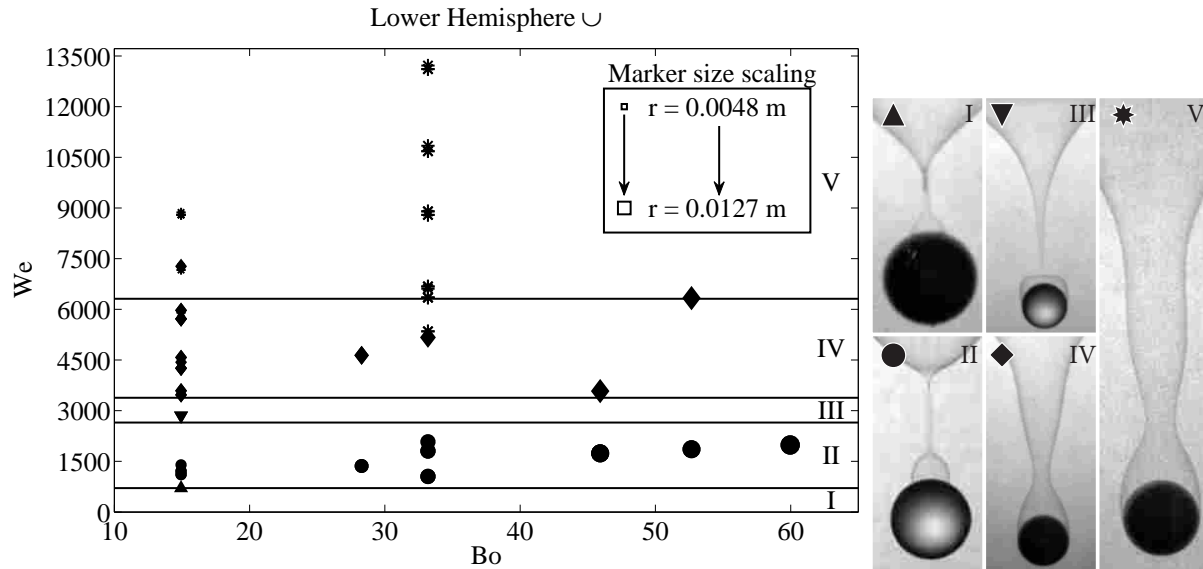


Figure 3.16: Regimes plotted Weber vs Bond number, for the lower half of the bubble. Notice that the regimes span nearly a century of bond numbers. Upward pointing triangles, circles, downward pointing triangles, diamonds, and asterisks indicate the five regimes noticed for the lower bubble hemisphere, as described respectively. Markers are filled to further indicate downward bubble orientation.

they get longer), that surface area requirement becomes prohibitive to allowing the sphere to pass without bubble rupture when the radius becomes too great. Some credence may be given to this argument by comparing the Figures 3.15 and 3.16. Notice the existence of the higher regimes in the lower bubble half case as opposed to the upper bubble half case. The difference being that the fluid drains down and into the point of collision for the lower case (providing more fluid), versus down and away from the point of collision for the upper case (lowering the amount of fluid available). This argument is discussed further below in 3.3.3.

### 3.3 Rupture Criteria

Some insight into the criteria for popping may be found by examining the probability of a bubble popping, plotted against different variables, namely: shape,  $We$  and  $r/R$ . It should be noted, however, that due to the number of experiments performed (in excess of 1000) and the sensitivity of soap films to small impurities, not all the experiments performed were recorded or saved. Some experiments were ignored if their results were deemed to be affected by external forces, such as a

dirty sphere or an unusually thin bubble. However, data was only discarded if the results deemed unnatural were unable to be duplicated. Additionally, since many experiments were performed holding all variables the same, only an accurate sample of the total number of experiments were kept. However, it is believed that the representation presented herein is a good one and that the probabilities given are repeatable. That said, we shall begin our discussion of the bursting of soap bubbles with a description of the ways in which it is accomplished.

### 3.3.1 Methods of Soap Film Rupture

There are many ways for a soap film to rupture and burst. Common types of bursting inherent to soap bubbles include: a charged or a dirty object (in our case spheres) touching the film, and deterioration of the film due to drainage or evaporation of the soap film liquid held between the monolayers of surfactant. Excluding these types of film rupture, there have been four observed types of breaking.

- A. **Pinch-off Rupture.** This rupture occurs when some part of the film bridge necks and attempts to pinch-off another part of the bridge, or the sphere. At pinch-off the film is ruptured and surface tension forces pull the bubble apart. An example of this may be found in Figure 3.17
- B. **Thinning Rupture.** This film breakup is characterized by the sphere deforming the bubble, forming the bridge shapes described above. However, before pinch-off the film cradling the sphere thins to the point of rupture and the bubble pops. See Figure 3.18 for an example.
- C. **Contact Rupture.** This rupture type takes place very soon after contact of the sphere with the film. The sphere seems to punch a hole through the film and rupture happens before the sphere is able to enter one sphere diameter into the bubble, see Figure 3.19
- D. **Side rupture.** This rupture takes place when the passing of the sphere through the bubble so distorts the bubble that its connection to the bubble cylinder is broken and the bubble ruptures from the side. This type of rupture indicates that the size of the sphere compared to the ball is too great for passage. See Figure 3.20 for an example.

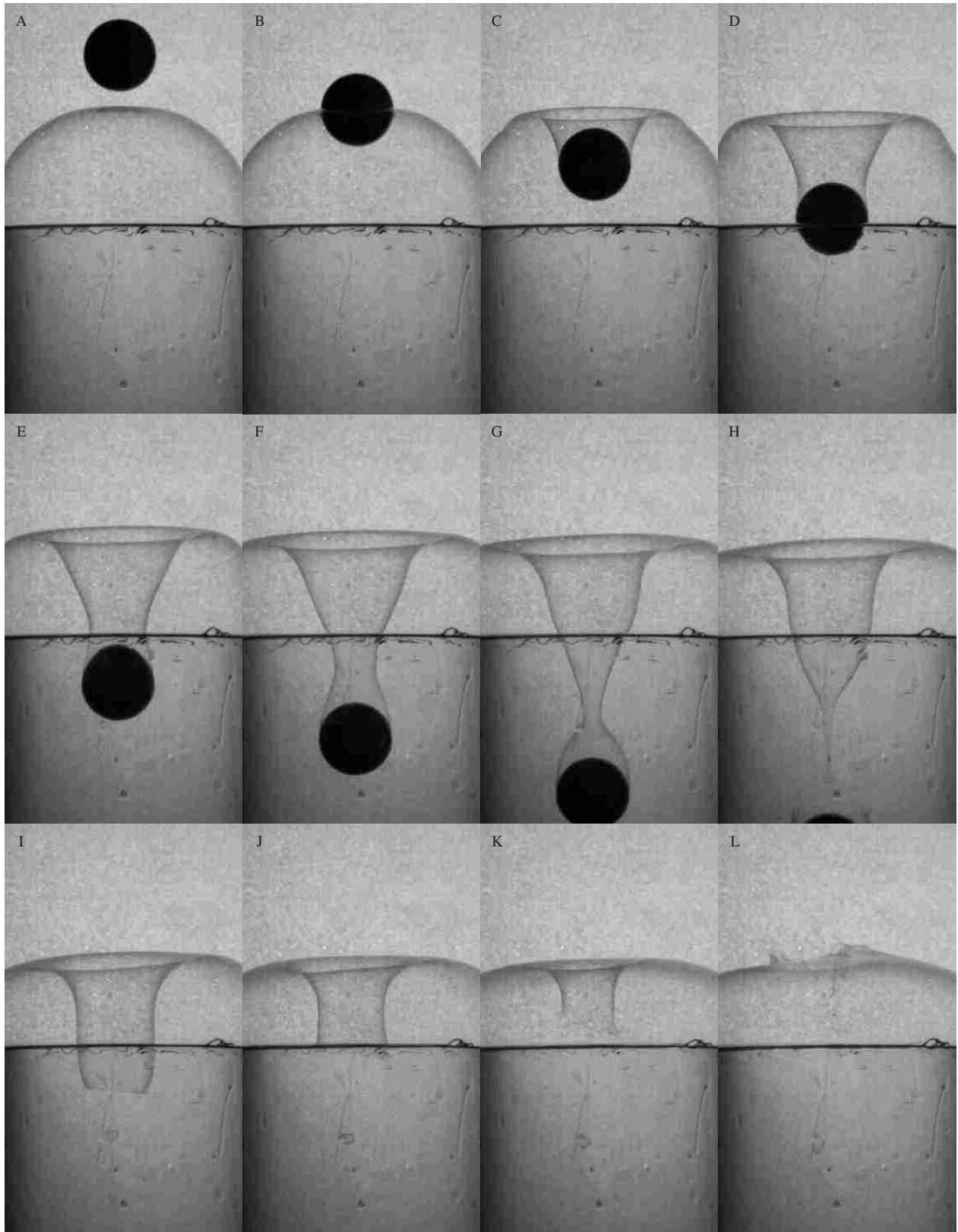


Figure 3.17: Example of a pinch-off rupture. The pinch-off occurs between frames (H) and (I) when the ‘tail’ at the bottom of the hopper funnel shape pinched-off. These are pictures of a 0.63 cm radius aluminum sphere falling from 222 cm above the upper hemisphere of a 1.5 cm radius bubble. Frames are 1.5 ms apart.

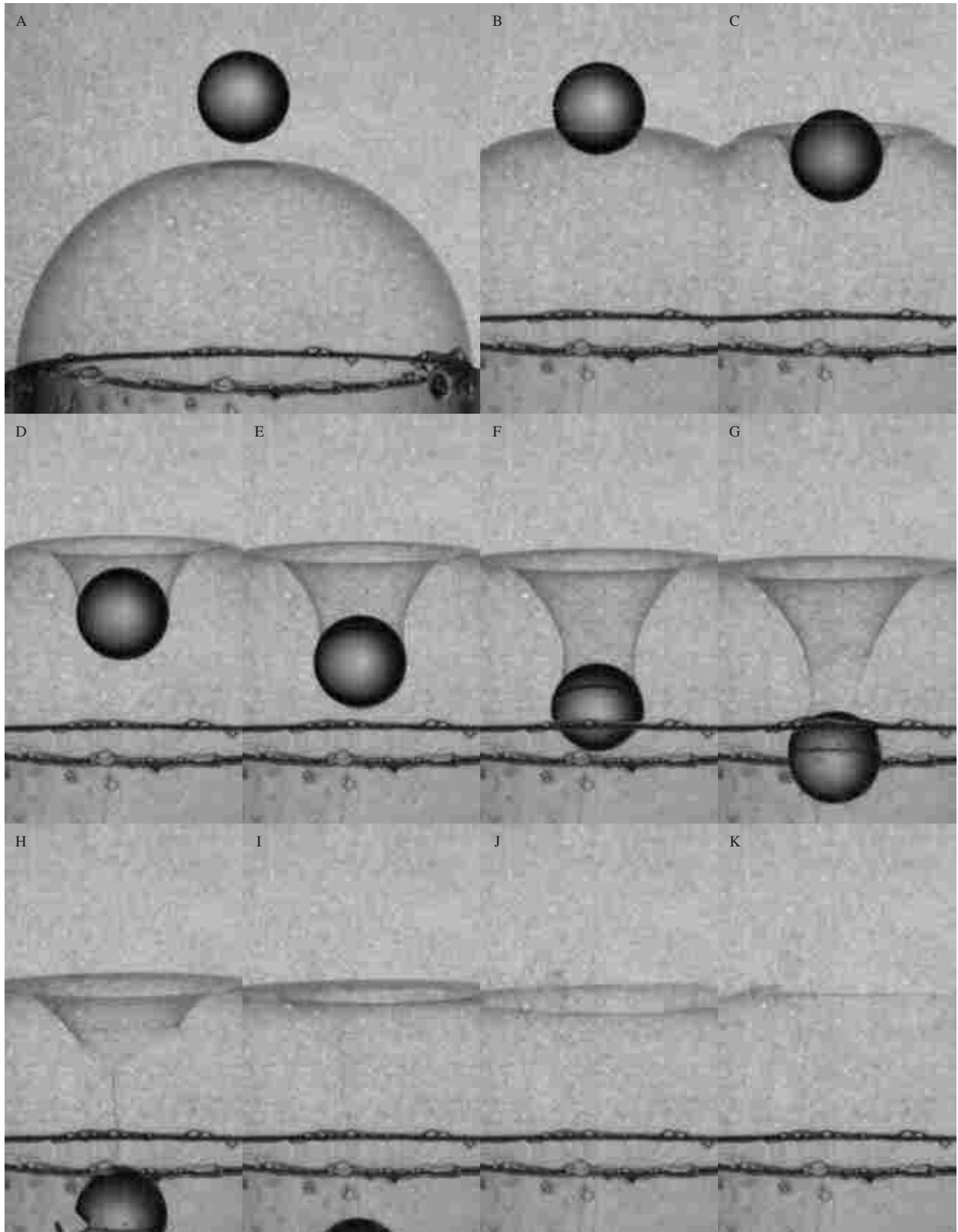


Figure 3.18: Example of a thinning rupture. The film is torn between frames (F) and (G). These are pictures of a 0.48 cm radius glass sphere falling from 124.6 cm above the upper hemisphere of a 2.25 cm radius bubble. Frames are 1.5 ms apart.

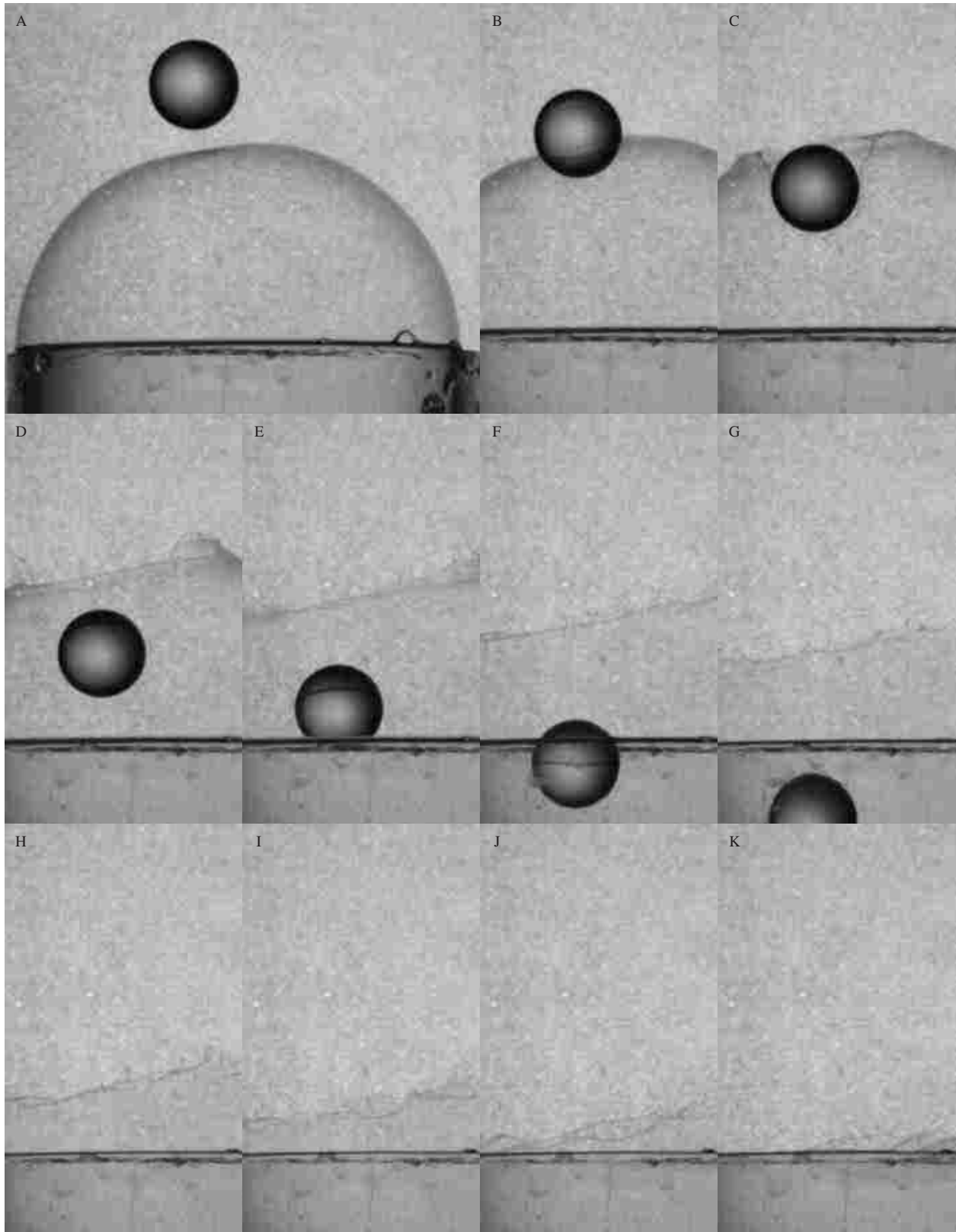


Figure 3.19: Example of a contact rupture. Note that by frame (C), with minimal displacement, the film is already ruptured. These are pictures of a 0.48 cm radius glass sphere falling from 183.4 cm above the upper hemisphere of a 2.25 cm radius bubble. Frames are 1.0 ms apart.



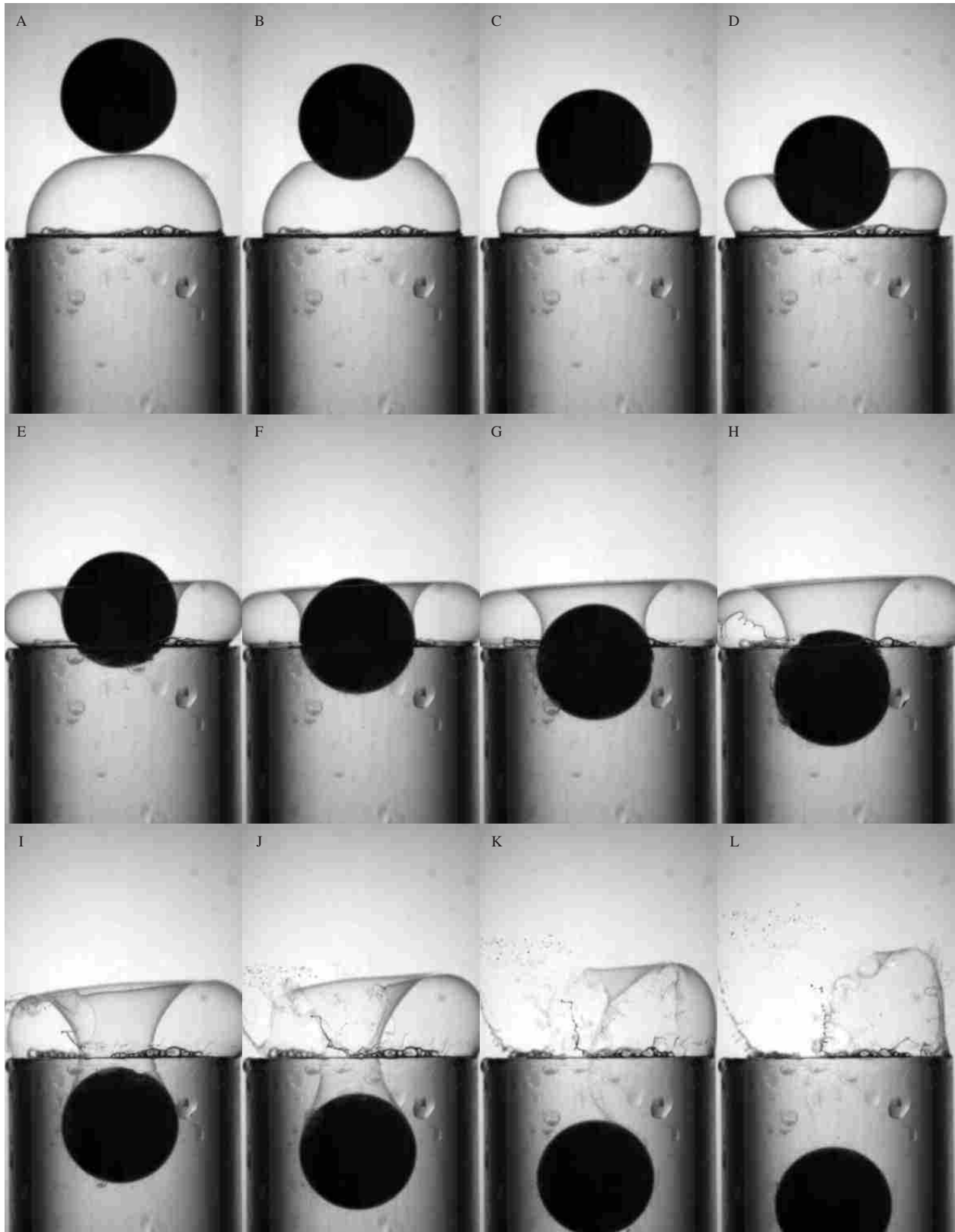


Figure 3.20: Example of a side rupture. Note the beginning of the rupture in frame (H) . These are pictures of a 0.94 cm radius aluminum sphere falling from 40 cm above the upper hemisphere of a 1.5 cm radius bubble. Frames are 1.5 ms apart.



### Short discussion of the rupture type image sequences

In Figure 3.17 we see the formation of a type IV regime, described above, but with rupture occurring before bubble side pinch-off. This example of pinch-off type rupture was created by dropping a 0.63 cm radius aluminum sphere through the upper hemisphere of a 1.5 cm radius bubble. The sphere was dropped from 222 cm above the film. Pinch-off occurs sphere side first between frames (G) and (H). Note the small film ‘tail’ at the bottom of the film bridge. This tail is pinched-off between (H) and (I), however this pinch-off is unsuccessful, do to an insufficient amount of film and rupture occurs. We see in frames (I) through (L) the movement of the rupture up the film bridge.

Figure 3.18 depicts a 0.48 cm radius glass sphere falling through the upper hemisphere of a 2.25 cm radius bubble. The sphere was dropped from 124.6 cm above the top of the hemisphere. This scenario should form a cone like film bridge shape, indicative of a type III regime. However, as the bridge develops in frames (A) through (F) the film thins to the point of rupture, with rupture occurring between frames (F) and (G). Frames (G) through (H) show the travel of the rupture up the film bridge and onto the main portion of the bubble.

The example of contact rupture, seen in Figure 3.19, was created by dropping a 0.48 cm radius glass sphere through the upper hemisphere of a 2.25 cm radius bubble. The sphere was dropped from 183.4 cm above the top of the bubble. Note how by frame (C) the film is already ruptured and how the rupture spreads over the bubble until it reaches the bubble cylinder, frames (C) - (K).

The final rupture example, seen in Figure 3.20, shows a 0.94 cm radius aluminum sphere falling through the upper hemisphere of a 1.5 cm radius bubble. The sphere was dropped from 40 cm above the top of the bubble. First note the large size of the sphere compared to the bubble (the sphere’s radius is 60% the bubble’s radius). We see in frames (A) through (G) large deformation of the bubble, with the bubble bulging around the sphere. The bulging eventually forces the film off the side of the bubble cylinder, causing rupture, see frame (H). this rupture spreads, left to right, across the bubble until nearly all of the bubble’s film is gone, see frames (H) through (L).

### 3.3.2 Probability of Rupture

As the data was gathered in two hemispheres, we will first examine each hemisphere separately. First we will look at the popping data for the upper hemisphere of the bubble, followed by the lower hemisphere. The data in both cases are examined from a probabilistic view point. The importance of such an examination lies in the general trends they demonstrate.

Soap films are incredibly unpredictable due, in part, to the variability of their thickness and their sensitivity to impurities. This results in mixed results for the same experiment. A sphere of a certain radius and dropped from a certain height may or may not rupture the film. Thus, since we were unable to control the film thickness, we will examine the probability of film rupture under various conditions.

#### Probability of rupture: upper hemisphere

Our first examination is that of how the bubbles popped according to the shape observed. For this plot the data was separated according to the transition Weber numbers (see Table 3.2). Thus all data samples in the I bar had Weber numbers below 1,650, all data samples in the II bar had Weber numbers between 1,650 and 3,170, etc. Each bar is a stack of the probabilities of bubble popping for each rupture type: pinch-off, thinning, punch, and side rupture and the numbers in the middle indicate the number of samples taken in each set. Thus, for regime IV in Figure 3.21 there were 171 experimental sphere drops. Of these, 30.4% produced a pinch-off rupture, 20.5% produced thinning rupture, 14.6% produced a punch rupture, and 0% produced a side rupture, for a total of 65% chance of rupture for this regime.

Note the nearly equal probability of popping for the first three regimes. Also, that regime IV probability of popping is more than twice that of the other regimes. It is not surprising that the probability of each type of rupture has increased in regime IV, however, it is surprising that the dramatic disproportionate increase in the number of pinch-off type ruptures.

The lack of side ruptures in regime IV is due to the fact that we stopped dropping very large spheres through small bubbles ( $0.6 \lesssim r/R$ ). We did this because all attempts resulted in bubble rupture, either through thinning or a side rupture. Side ruptures happened more often at higher drop heights. This is not shown in Figure 3.21 simply because, as stated above, once it

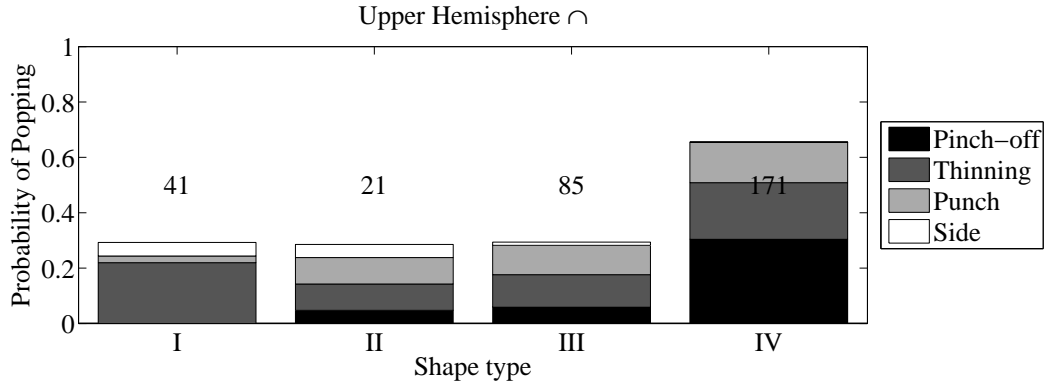


Figure 3.21: Probability of bubble popping sorted by regime Weber numbers, for the upper hemisphere. The numbers in the middle of the figure indicate the number of samples taken for each data set.

became obvious that a combination of conditions (sphere and bubble size, height, etc.) always resulted in bubble rupture no additional data was taken at, or above, the given height.

Figure 3.22 shows the probability of popping throughout the range of Weber numbers recorded. The vertical lines indicate the transition lines from one regime to another. Note that the large percentage of the pinch-off ruptures occur at the end of regime (III) and the beginning of regime (IV). Also, the sudden increase in probability of popping near the middle of the third regime. This seems to indicate that around this point the fluid is being stretched too quickly to repair itself either at pinch-off or through tearing. The tearing failures dramatically increase in probability around a Weber number of 12000. This is perhaps due to the increase in thinning rate of the film. Thus, if the film were not thick enough to begin with, it is much more likely to tear before pinch-off occurs.

Figure 3.23 sorts the probability of popping by the ratios of the radii,  $r/R$ . Several things may be learned from this figure, first, the extremes of the ratios yield drastically different results. Sphere radii near or above 55% of the bubble radii are unable to successfully enter the bubble. Note the lack of pinch-off ruptures in these cases. This indicates that the film thinned to the point of rupture before the film bridge had time to collapse. On the other end of the spectrum, all attempts to pass a sphere through the flat film representing an infinite size bubble were successful. However, only five data points and a maximum  $We = 8,415$  were examined. An increase in either of these numbers would surely increase the number of ruptures, but the complete lack of ruptures is still

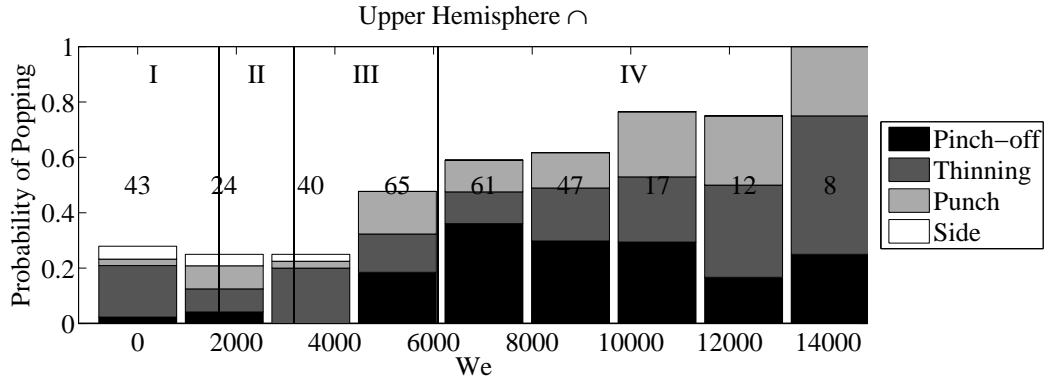


Figure 3.22: Probability of bubble popping according to Weber number, for the upper hemisphere. The numbers in the middle of the figure indicate the number of samples taken for each data set.

significant. One possible reason for this lies in the lack of draining of the film found in the other ratios. In this case the film thickness at the moment of impact was certainly much higher than in the other cases. It is likely that the film thickness at the point of impact was at least double that in the other cases.

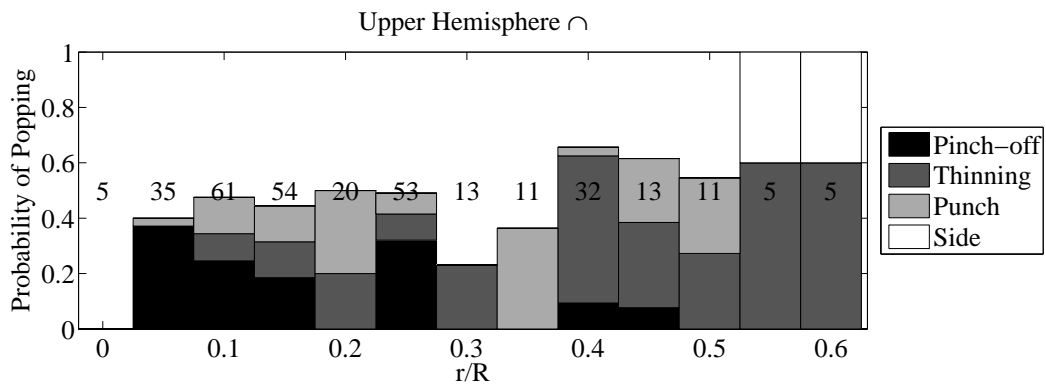


Figure 3.23: Probability of bubble popping sorted by  $r/R$ , for the upper hemisphere. The numbers in the middle of the figure indicate the number of samples taken for each data set.

### Probability of rupture: lower hemisphere

We will examine the popping probabilities of the lower half of the bubble in the same order as the upper half, that is: by regime,  $We$ , and  $r/R$ .

Examining the probabilities sorted by regime (see Table 3.3 for the regime Weber number divisions), it is remarkable what low percentages of rupture occur in each of the first three regimes as compared the last two, IV and V, see Figure 3.24. Although this increase in rupture rates was seen above, starting in regime IV, the increase was not so dramatic. Also, note the low percentages of thinning type ruptures and the low, and nearly constant, rates of pinch-off type ruptures. These two phenomena are no doubt a product of the thicker film found in the lower hemisphere of the bubble. One conclusion is that a thinning type rupture is related mainly to the thickness of the bubble film at the time of contact.

Although there has been a decrease in thinning type ruptures, there are much higher rates of punch type ruptures. This may be due to the geometry of the situation. Whereas for the upper hemisphere of the bubble, the pressure difference and bubble curvature work together to push the film close to, and around the sphere, the situation is reversed in the lower hemisphere. In the lower hemisphere the higher pressure inside and lower pressure outside the bubble naturally want to push the film apart and push *with* the sphere against surface tension forces instead of *against* the sphere, as is the case in the upper hemisphere. Thus, quicker rupture is much more likely to happen in the lower hemisphere than the upper. Another possible reason for these ruptures is that as the sphere moves through the film, in the lower hemisphere, it is intersecting increasingly thinner film, due to drainage. This is not so for spheres crossing the film in the upper hemisphere, which move through progressively thicker film, also due to drainage. Thus, whereas in the upper hemisphere the film becomes increasingly able to allow the spheres passage, in the lower hemisphere the films ability to allow sphere passage diminishes with the motion.

Additional insight may be found by further sorting the data by Weber number and by  $r/R$ . The results of sorting by Weber number are found in Figure 3.25 and they mirror the results seen in Figure 3.24. First, there seems to be a large jump in pinch-off type ruptures for Weber numbers above 10,000 and very high percentages of thinning ruptures occurring between Weber numbers 4,000 and 10,000. Additionally, comparing these results to the upper hemispheres analogous results in Figure 3.22 one finds a marked difference. The lower Weber number results have a much smaller percentage of popping than is found above. This is also true regarding the higher Weber numbers. The lower hemispheres' likelihood of popping is, on average, more than 25% lower for the last three bars than the corresponding bars for the upper hemisphere (see Figure 3.22). Finally,

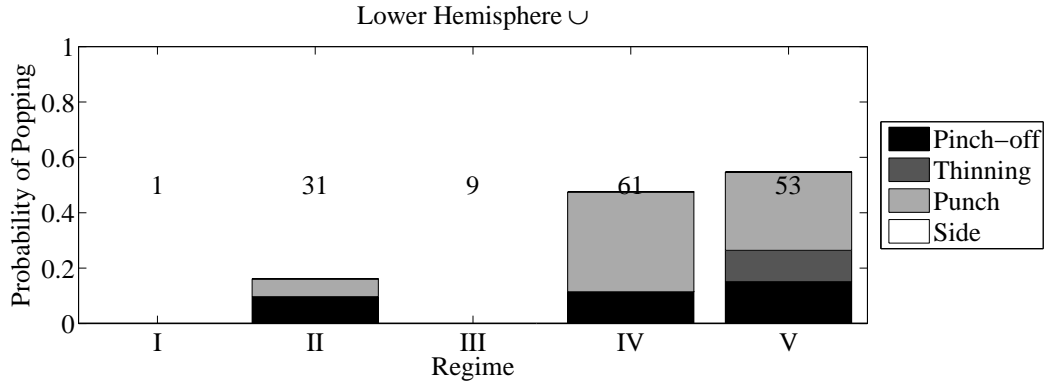


Figure 3.24: Probability of the lower hemisphere of the bubble popping according to regime. The numbers in the middle of the figure indicate the number of samples taken for each data set.

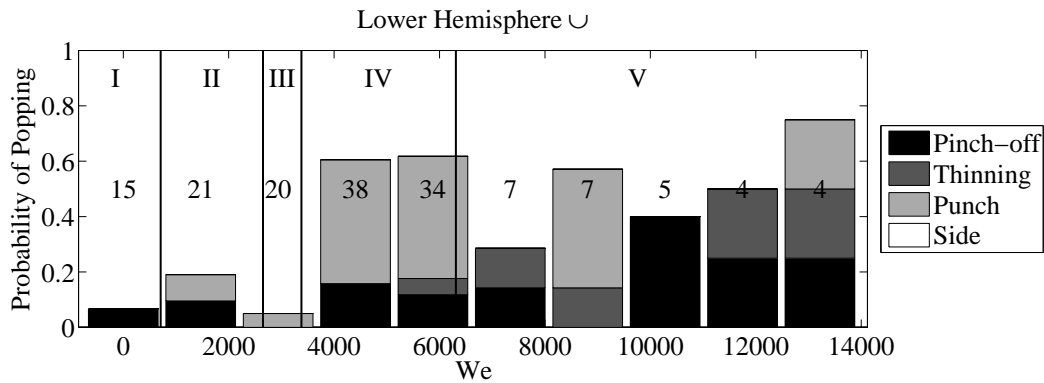


Figure 3.25: Probability of the lower hemisphere of the bubble popping according to  $We$ . The numbers in the middle of the figure indicate the number of samples taken for each data set.

the last bar is lower than unity. This suggests that higher Weber numbers may be obtained without rupture in the lower hemisphere than the upper.

Sorting by  $r/R$  (see Figure 3.26) generates a few final comments. First, there is a remarkable consistency in the probability of rupture spanning the entire scale of  $r/R$ . This mirrors the results seen for the upper hemisphere, see Figure 3.23, with the exception that there is a relatively low percentage of ruptures for  $r/R$  values between 0 and 0.1. In the upper hemisphere this area exhibits roughly the same chance of rupture as its larger neighbors. The second comment relates also to a comparison to the upper hemispheres results. It is clear from the graphs that the probabilities for rupture, according to  $r/R$  ratios, is appreciably lower, on average, than they are for the upper hemisphere. As a third and final comment, it is interesting to note the dominance of

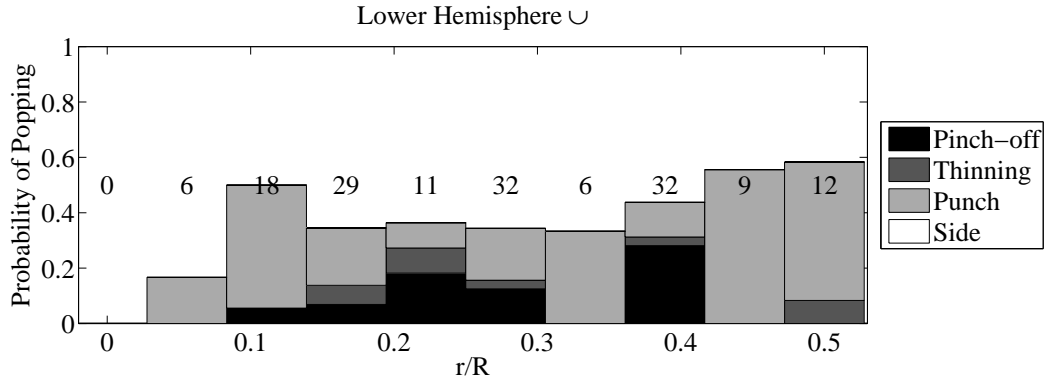


Figure 3.26: Probability of the lower hemisphere of the bubble popping according to  $r/R$ . The numbers in the middle of the figure indicate the number of samples taken for each data set.

the punch type rupture in nearly each data bar. Combining this data with the results presented in Figure 3.25 suggests that most of these punch ruptures occur at Weber numbers ranging from four to ten thousand and not that the high percentages of punch ruptures was due to something such as sphere size. Rather it seems that there is a 'sweet spot' for achieving a punch type rupture and that that sweet spot depends mainly upon Weber number.

So far we have investigated the probability of film rupture sorted by regime, Weber number, and  $r/R$ . Some final insight to this phenomena may be found by sorting the data by sphere size. The results are presented in Figures 3.27 and 3.28. Do to the low number of experiments performed using the smallest glass sphere and the two pool balls, their data was omitted from the figures.

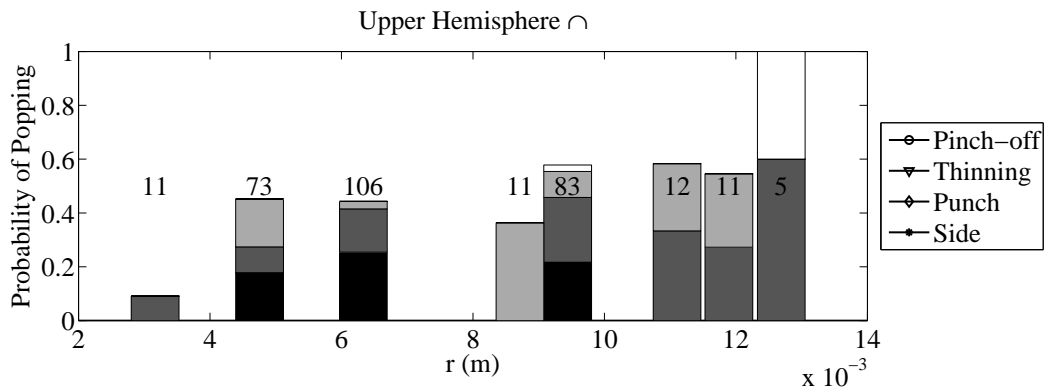


Figure 3.27: Probability of the upper hemisphere of the bubble popping according to  $r$ . The numbers in the middle of the figure indicate the number of samples taken for each data set.

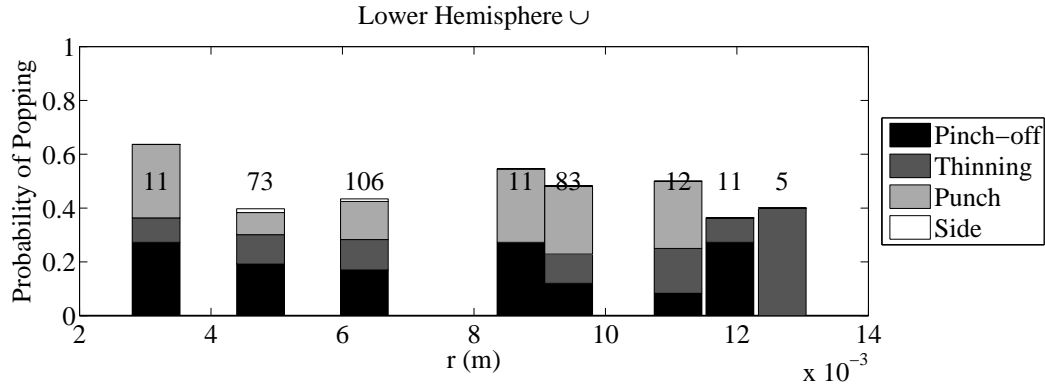


Figure 3.28: Probability of the lower half of the bubble popping according to  $r$ . The numbers in the middle of the figure indicate the number of samples taken for each data set.

A general higher upward trend of the percentage of ruptures occurring as the spheres get larger, culminating in the largest presented sphere size which obtained 100% ruptures. Also note the increasing, then decreasing trend in the percentage of pinch-off ruptures as well as the high percentage of thinning ruptures for spheres with a radius greater than  $10e-3$ . Both of these trends denote a relationship between film thickness and the sphere's size. Indeed, the larger the sphere, the more the surface area of the bubble must be deformed to allow the passage of the sphere. As the surface area grows through this deformation, the thickness of the film necessarily grows thinner, increasing the chance of rupture. This idea is further illustrated below.

### 3.3.3 Rupture Dependence on Weber Number and Radius

It is instructive to view all experimental data on one single graph. Where as above in Figures 3.13 and 3.14 we only presented data representing un-ruptured bubbles, Figures 3.29 and 3.30 present all the data together on a single plot, per hemisphere.

Figure 3.29 suggests that there exists a limit to a sphere's size and velocity, and its ability to pass through the bubble. As the ruptures in the gray area indicate, this is an area where no sphere was able to successfully enter the bubble. This trend is continued in Figure 3.30 for which a similar gray mask has been applied.

Although the defining line for certain bubble rupture is not quite as clear in Figure 3.30 as it is in Figure 3.29, in both plots there seems to exist a point where the thinning required to allow the sphere to pass through is too great and rupture occurs. This thinning is related to the Weber



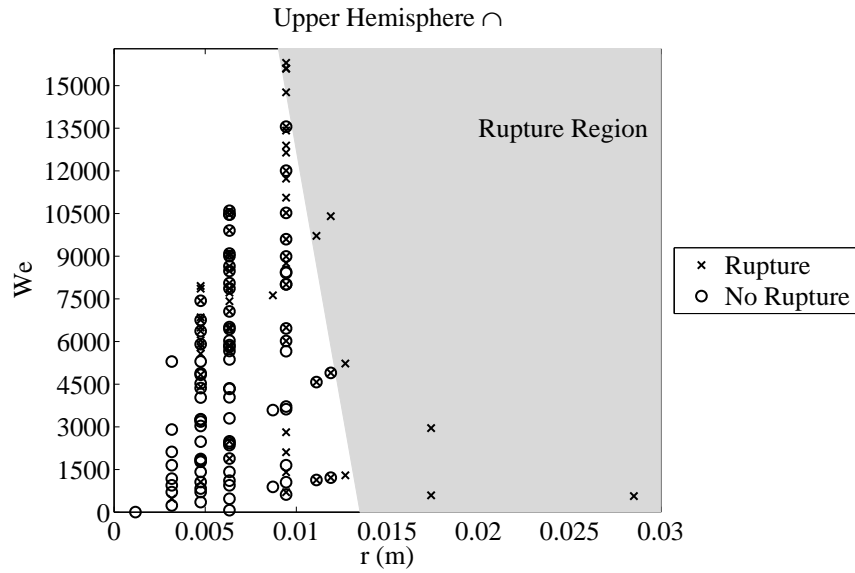


Figure 3.29: Combination of all experimental results for the upper hemisphere. Attention is only paid to whether or not the bubble ruptured.

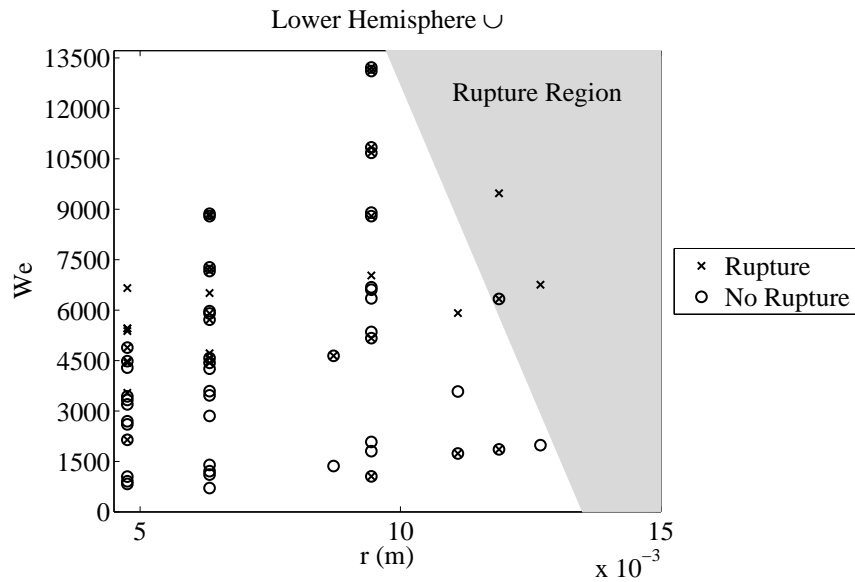


Figure 3.30: Combination of all data for the lower hemisphere. Attention is only paid to whether or not the bubble ruptured.

number (Equation (3.1)). As stated above, the larger the sphere, the more the film must stretch to allow passage. Also, the faster the sphere is moving, the quicker the film must stretch (thin) to allow entry or exit of the sphere. Thus, it should not be surprising that ruptures increase with Weber number, see Figures 3.22 and 3.25. Furthermore, it should not be surprising that the size of the sphere also matters. For a larger sphere will thin the bubble's film more quickly (regardless of the bubble size), in order to allow the passage of the sphere, than a smaller sphere with the same Weber number. This idea is supported through a simple analysis.

We may approximate the thinning of a bubble's film, resulting from the passage of a moving sphere, by modeling a sphere passing through a film disk. If we assume that the film is formed from a constant volume of fluid and that the film's thickness is equal at all points, in time, (meaning that no portion of the film is thicker or thinner than another portion, at any point in time), we may approximate the thickness by the following equation:

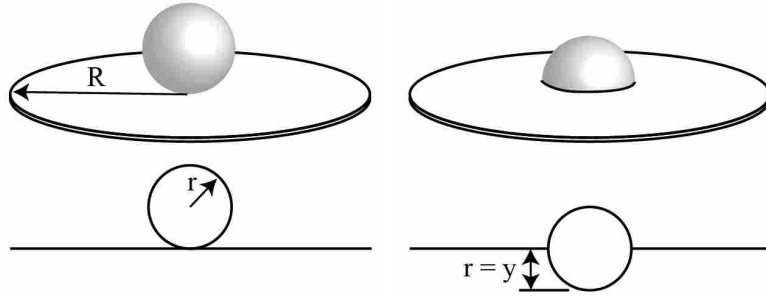
$$T(t) = \frac{\forall}{A_s(t)} \quad (3.4)$$

where  $T(t)$  is the film's thickness as a function of time,  $\forall$  is the initial, and constant, film volume, and  $A_s(t)$  is the film surface area, in time. We may approximate this surface area of the sphere-film interaction in two stages. Given a film disk of set thickness and radius, the first stage begins when the moving sphere begins to deform the film, and ends once the film reaches the sphere's equator see Figures 3.31(a) and 3.31(b). For this stage, the surface area can be modeled as the sum of the surface area of the sphere touching the film and the surface area of the unaltered disk, see Equation (3.5).

$$A_s = \int_0^{2\pi} \int_0^{\alpha} r^2 \sin(\theta) d\theta d\phi + \pi(R^2 - (\sqrt{r^2 - (r-y)^2})^2) \quad y \leq r \quad (3.5a)$$

$$= 2\pi r^2(1 - \cos(\alpha)) + \pi(R^2 - 2ry + y^2) \quad y \leq r \quad (3.5b)$$

where  $R$  is the radius of the film disk,  $r$  is the radius of the sphere,  $y$  is the vertical distance the sphere has moved from its initial condition, and  $\alpha$  is the angle between the bottom of the sphere and the point on the sphere intersecting the unaltered film disk, see Figure 3.32.



(a) Beginning of the first stage, just before the sphere hits the film. (b) End of first stage, the sphere is half way through the film.

Figure 3.31: Diagram of the first stage of the surface area approximation.  $R$  is the radius of the film disk,  $r$  is the radius of the sphere, and  $y$  is the distance the sphere has fallen.

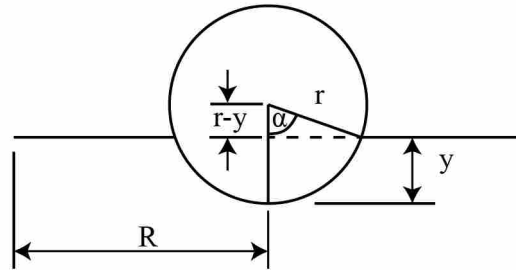


Figure 3.32: Dimensions and layout used in Equation (3.5)

Equation (3.5) may be simplified by noting that

$$\alpha = \arccos\left(\frac{r-y}{r}\right). \quad (3.6)$$

Thus Equation (3.5) becomes

$$A_s = 2\pi r^2(1 - \cos(\arccos(\frac{r-y}{r}))) + \pi(R^2 - 2ry + y^2) \quad y \leq r \quad (3.7a)$$

$$= 2\pi r^2(1 - (\frac{r-y}{r})) + \pi(R^2 - 2ry + y^2) \quad y \leq r \quad (3.7b)$$

$$= 2\pi ry + \pi(R^2 - 2ry + y^2) \quad y \leq r \quad (3.7c)$$

$$= \pi(R^2 + y^2). \quad y \leq r \quad (3.7d)$$

The second stage begins once the sphere has moved a distance further than its own radius down from its initial position, see Figure 3.33. For this stage the surface area is calculated as the summation of: half the surface area of the sphere, the surface area of the open cylinder connecting the sphere to the unaltered film and the surface area of the unaltered film disk, see Equation (3.8).

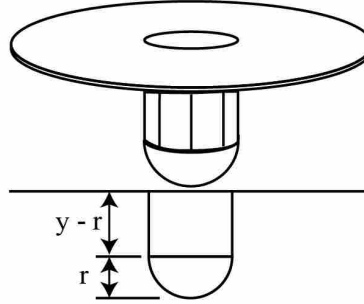


Figure 3.33: Diagram second stage, sphere is more than half way through the film.  $R$  is the radius of the film disk,  $r$  is the radius of the sphere, and  $y$  is the distance the sphere has fallen.

$$A_s = 2\pi r^2 + \pi r(y - r)\pi(R^2 - r^2) \quad y > r \quad (3.8a)$$

$$= \pi(R^2 + 2ry - r^2) \quad y > r \quad (3.8b)$$

Since our spheres are falling, with an initial velocity of zero,  $y$ , the distance the sphere has fallen, may be approximated as

$$y = u_0 t, \quad (3.9)$$

where  $u_0$  is the velocity at the moment of impact and  $t$  is the time elapsed since impact. Combining Equations (3.7) and (3.8) and substituting the value of  $y$  from Equation (3.9) yields:

$$A_s(t) = \begin{cases} \pi(R^2 + (u_0 t)^2) & y \leq r \\ \pi(R^2 + 2ru_0 t - r^2) & y > r \end{cases} \quad (3.10)$$

Now that we have an approximation of the surface area as a function of time, we only need to know the volume in order to determine the thickness from Equation (3.4). Since we assume that the volume of the film is constant in time, the volume may given by

$$V = \pi R^2 T, \quad (3.11)$$

where  $T$  is the initial thickness of the film disk. Equations (3.10) and (3.11) may be substituted into Equation (3.4) to obtain an approximation of the thickness of the film at any point in time. Using this approximation of the thickness, we see that when the sphere first contacts the film, the film's thickness decreases quadratically in time (this is a result of equation (3.10)). Once the sphere has descended a depth of larger the length of its radius into the film the thinning becomes linear. Although we lack the ability to validate this model (since we are unable to know the initial thickness of the film), we were able to get a qualitative feel for it's validity overall. Additionally, we were able to find good agreement between the linear portion of the model and actual increase in surface area. This is discussed below in 4.4

Using this model we may now examine the thickness of the film in time for spheres of different radii and velocities. First, we see that because larger spheres have a larger radius, more time is spent with the film thinning quadratic (see Figure 3.34).

In this plot the thinning rates for all the spheres were calculated using the same initial velocity and thickness. Note that by the end of the time of interest (0.05 s) the smallest sphere has a thickness more than four times that of the largest sphere.

Although sphere radius plays a large role in the thinning rates, the role of the spheres velocity cannot be discounted, as Figure 3.35 indicates. This figure was generated using the above model, holding the sphere radius constant and altering the initial velocities.

Using this model one may hypothesize that if the thickness of the film could be known just before sphere contacts the film, that one could scale the data used in Figures 3.29 and 3.30, so that the ruptures in those figures would lie only in the gray area, while the non-rupture cases would lie only in the white.

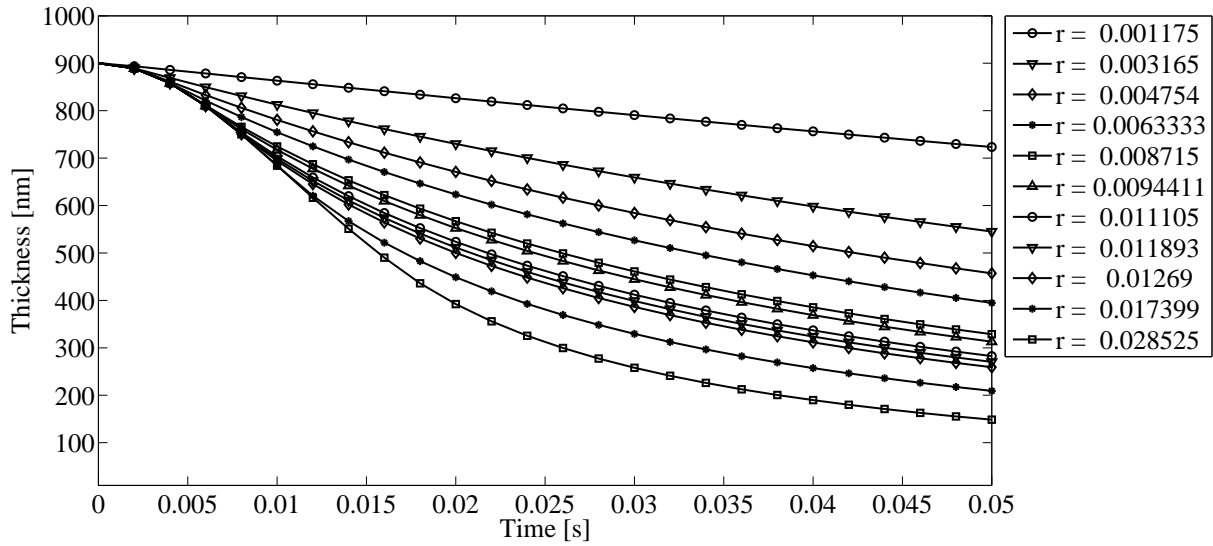


Figure 3.34: Plot of film thickness as a function of time. Thickness is calculated using Equation (3.4). Each line represents a different sphere.

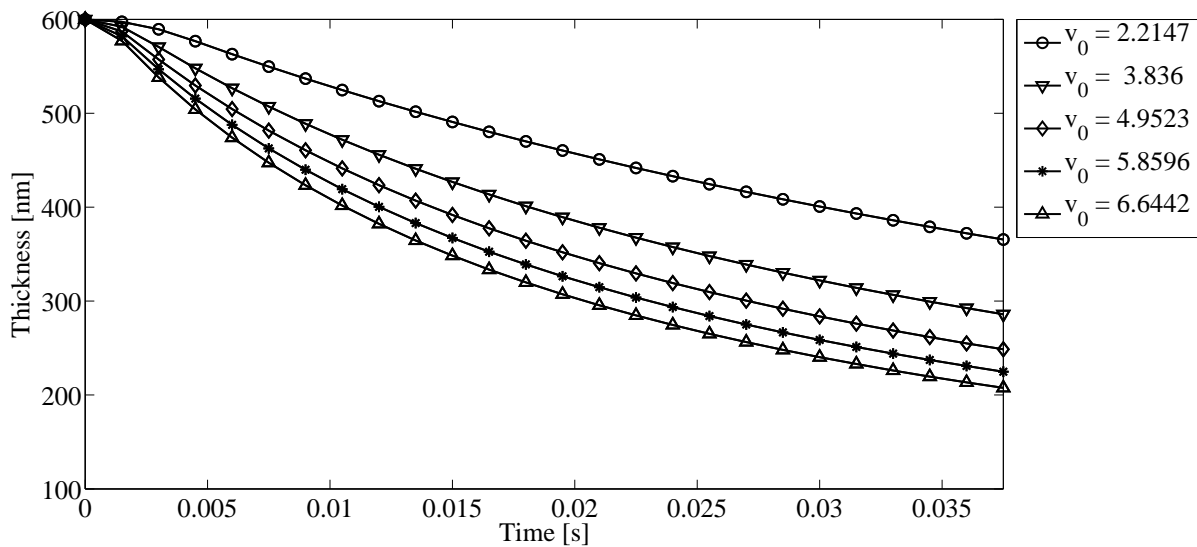


Figure 3.35: Plot of film thickness as a function of time. Thickness is calculated using Equation (3.4). Each line represents a different initial velocity for a 9.4 mm radius aluminum sphere.

### 3.4 Conclusions

This chapter has presented several discoveries concerning the phenomena of passing solid spheres through soap bubbles. We have shown the complete dependence of the regimes' discussed

above dependence on the Weber number and the regimes' surprising independence from the bond number. These results are clear and very reproducible.

We have also discussed the probabilities of bubble rupture sorted under different criteria. From these probabilities several things become apparent. First, that the thickness of the film is key to allowing sphere entry or exit. This is seen, for example, in the differences in film rupture rates and types between the upper and lower hemispheres where the film thickness is different, due to drainage. Second, that there are both limits on the relative size of the spheres, compared to the bubble size, and the absolute size the sphere may be and still successfully pass through the bubble's soap film. Finally, that there is a clear connection between sphere size, its velocity and its ability to pass through the soap film.

## **CHAPTER 4. DISCUSSION OF INTERESTING PHENOMENA**

In this chapter we discuss several interesting phenomena noticed during the course of this research. First, we will view a case where a falling sphere is encapsulated in a smaller satellite bubble after the sphere successfully passes through the bubble's film. Next we will examine interesting behavior of a bubble as it approaches bubble side pinch-off. Then we will witness the remarkable ability of a bubble to be ripped, and yet be able to repair itself before complete rupture occurs. Finally, examine some interactions between the moving sphere and the bubbles soap film. This includes discussing the rates at which the soap film stretches as the sphere moves through the bubble and examining the forces on the sphere as it intersects the soap film.

### **4.1 Sphere Encapsulation**

As the sphere drops through the air and moves toward the bubble there forms a boundary layer of air around the sphere. This boundary layer deforms the bubble surface ahead of the spheres as the sphere approaches the bubble. It may seem however, that once the sphere hits the bubble that the boundary layer disappears and the sphere is wetted, see Figure 4.1, frame (A) for example.

While it is certainly the case that wetting happens under some circumstances, this is not always the case, as evidenced by frames (E) through (L) and especially frame (J) of Figure 4.1. These frames clearly show the entrained air located on top of, and connected to, the sphere moving down the sphere's sides, surrounding the sphere, and even moving a bit below the sphere, as the elasticity of the film reacts to the forces of pinch-off, surface tension, and pressure. An enlargement of the sphere in frame (J) Figure 4.1 may be found in Figure 4.2.



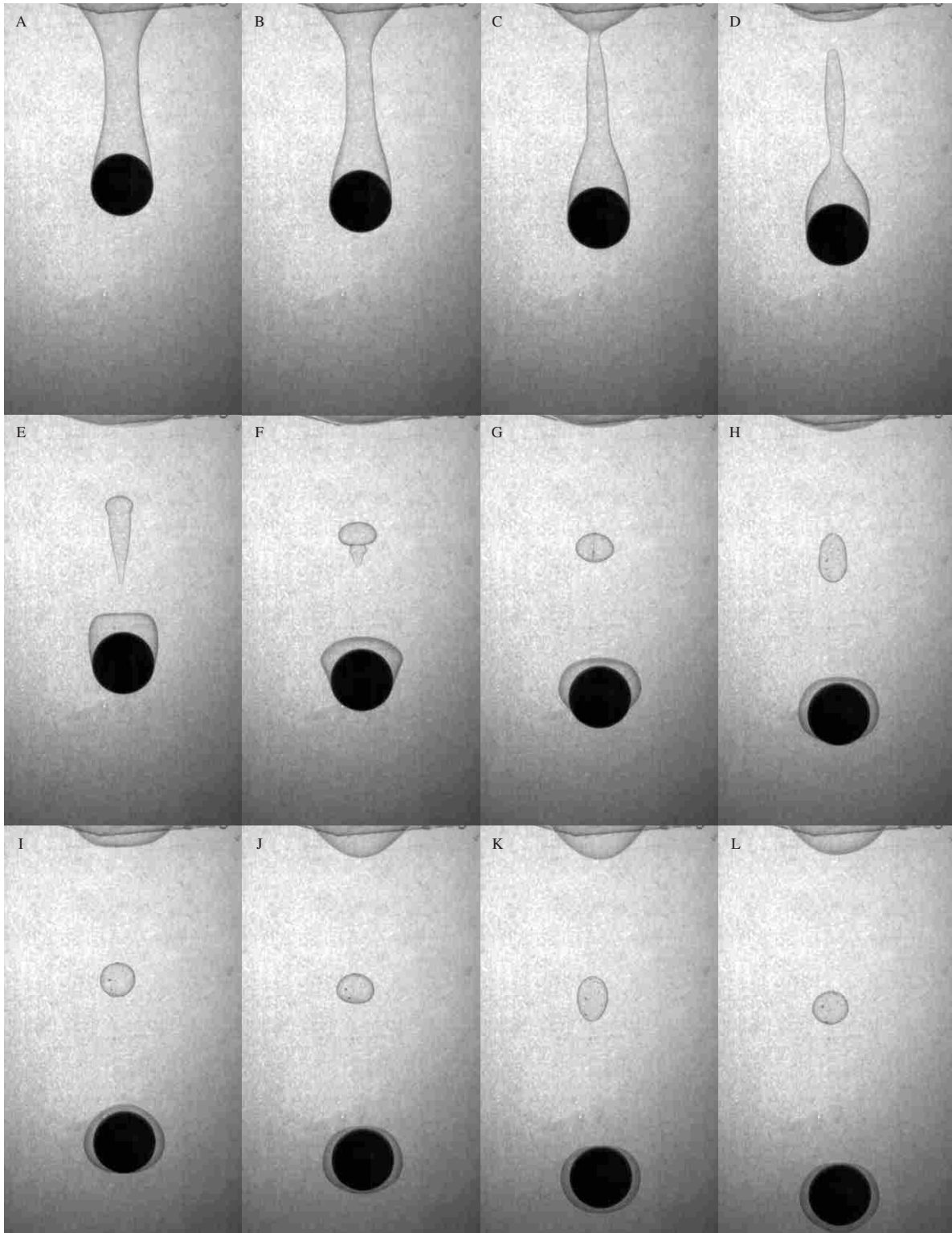


Figure 4.1: Images of a 6.3 mm radius aluminum sphere being encapsulated. Note the decent of the bubble, initially located at the top of the sphere (frame (E)), down the side of the sphere (frames (F) - (J)), until, by frames (K) and (L) the encapsulating bubble's film has moved below the sphere. If the sequence of frames were continued, the bubble would be pushed up again as drag forces push on the bubble.



Figure 4.2: Enlargement of the encapsulated sphere from frame (J) in Figure 4.1

As these figures show, there clearly remains some air between the surface of the sphere and the bubble's soap film. For spheres moving at lower speeds, this phenomena was never noticed. This leads us to believe that the air boundary layer formed by the falling sphere thins to the point where lubrication forces become important and the 'draining' of the air slows down. For low weber numbers, there is enough time for the air to move away from the sphere and become wetted. However, at higher speeds, the boundary layer has insufficient time to drain thus, the sphere becomes encapsulated by a small satellite after piercing the main bubble.

## 4.2 Curvature Battle

We have discussed the pinch-off of the film bridge connecting the bubble to the sphere, see Section 3.1. In most cases the pinch-off of the film bridge follows a predictable course. Surface tension forces compel the film forming the bubble and connected bridge to assume a minimal surface, while the film is being driven to that minimal surface, one of two things may happen.

One outcome of the forced surface minimization is that the surface tension forces cause necking to occur at some point along the film. The necking continues until the pressure dominates surface tension and necking stops. At this point secondary necking occurs on either side of the high pressure area until pinch-off, which produces a satellite bubble of the air entrained between the two pinch-off locations. This is generally what happens in regimes I - III.

The second possible outcome is similar to the first, only the necking continues until pinch-off. This is what happens in regimes III - V. The satellite bubbles occurring in these regimes are a

result of the individual pinch-off's beginning sphere side and continuing upward until bubble side pinch-off.

One of the above two pinch-off and bridge collapse types occurs in nearly every experiment performed. There were noticed, however, a few (and repeatable) examples where the second type mentioned above fails in its initial attempt at bubble side pinch-off. An example of this is seen in Figure 4.3.

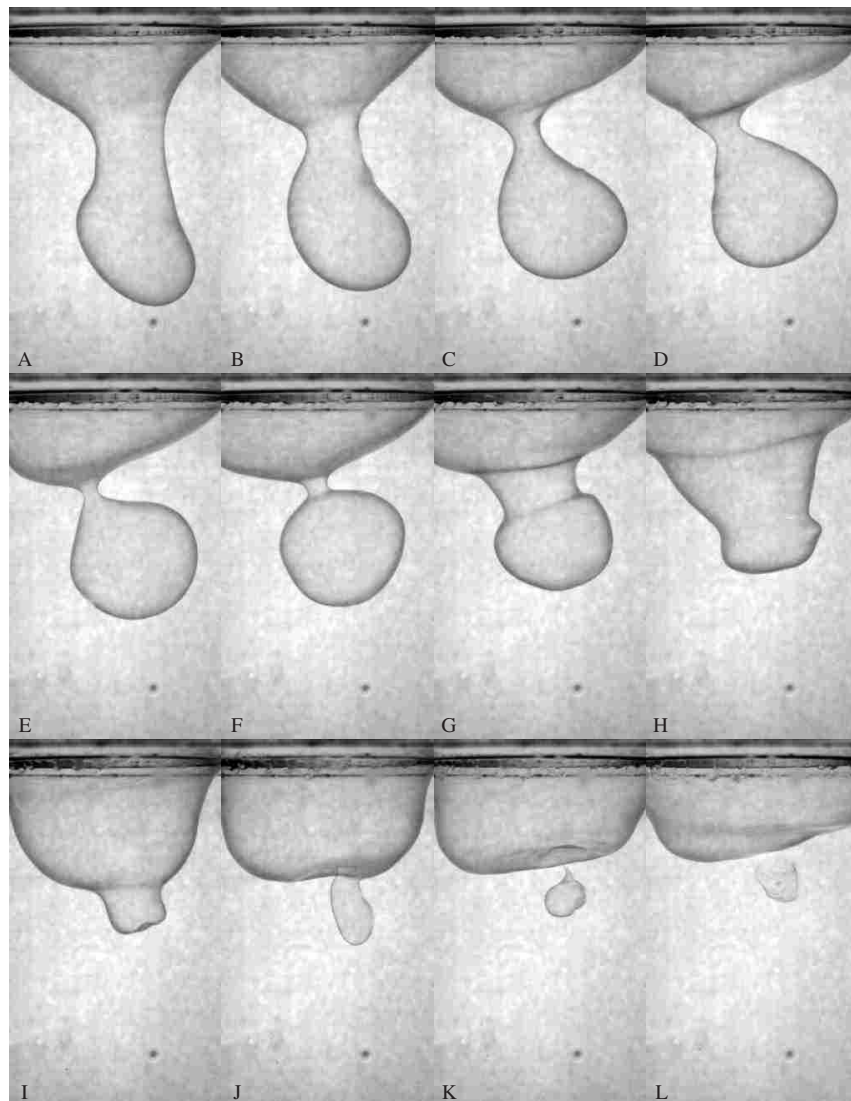


Figure 4.3: An example of a failed bubble side pinch-off attempt. In this example the lower hemisphere of a 2.25 cm bubble was pierced by a 9.4 mm radius aluminum sphere. Sphere side pinch-off has already occurred by frame (A). Note the necking occurring in frames (A)-(F) and the sudden expansion of the 'neck' by frame (G). Another pinch-off attempt is successfully completed by frame (K).

An explanation for this behavior might be found by examining the forces present in frame (F) of Figure 4.3 through the Laplace equation, Equation 1.1. This equation states that the pressure at any point along the wall of a soap film is determined by its curvature and surface tension. Higher curvature results in a higher pressure at the wall, and thus higher forces and vice versa. Applying this principle to frame (F) of Figure 4.3 yields the diagram in Figure 4.4:

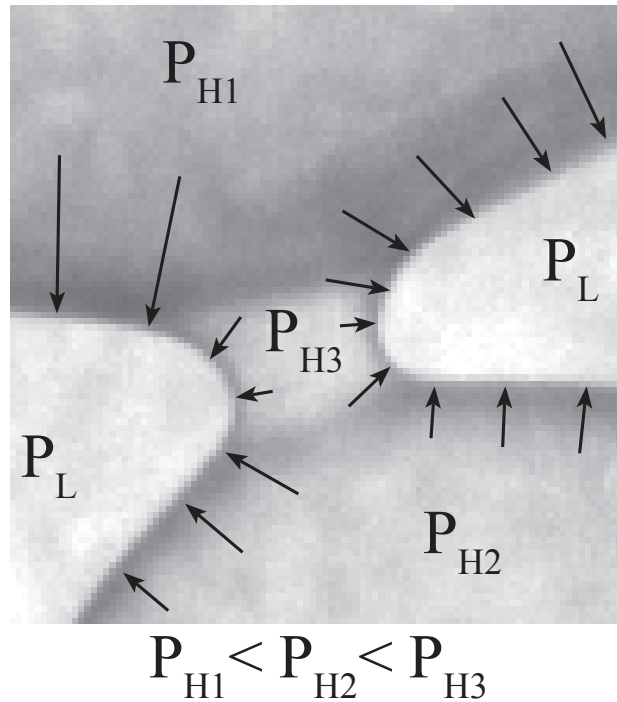


Figure 4.4: Frame (F) from Figure 4.3 with indications of high and low pressure spots as well as general forces acting on the film. Note, arrow size is unimportant.

The draining behavior seems to be driven by two forces, the pressure and surface tension. Surface tension forces are attempting to minimize the surface area of the film, by seeking to pinch-off the large satellite bubble. However, as the necking begins the pressure builds in the region of  $P_{H3}$  in Figure 4.4, with low pressures outside the soap film and high pressures inside the film, with a highest pressure located in the film bridge. If  $P_{H3}$  is large enough the film bridge cannot collapse and the air located in the satellite bubble is given time to drain. Draining moves the flow from  $P_{H2}$  to  $P_{H1}$ , causing a decrease in pressure near  $P_{H3}$ . The decreasing pressure increases the radius of curvature, further encouraging draining and pushing the neck outward. It seems that the key to achieving a  $P_{H3}$  sufficiently high is to keep the satellite bubble near the film bridge. Note that the

radii of curvature of the film bridge are very small and nearly equal. This results in a very large pressure gradient ( Equation (1.1)).

### **4.3 Film Rupture: Pinch-off Repair**

This section touches simply on an interesting phenomenon witnessed only a few times and may be found in Figure 4.5. This phenomenon is by no means reproducible as it is dependent on film thickness at the moment of impact, which, as we have discussed is outside the realm of our control. This phenomenon is marked by a thinning of the film close to the falling sphere to the point of rupture. The film ruptures, but, rather than a complete bubble rupture, the film bridge pinches-off above the thinning rupture, thus preventing complete rupture. This phenomena was also witnessed in the same experimental drop shown in Figure 4.3. In this case, however, the film rupture was caused by the sphere side pinch-off, which resulted in a pinch-off rupture. However, by frame (A) of Figure 4.3 the pinch-off of the ruptured film has already occurred.

It is amazing to witness this ability of the soap film to heal itself above a portion of film which has been ruptured. This phenomena was only found in regime V. A reason for this may lie, again, in the increased thickness of the film allowing for a longer film bridge. A longer bridge may allow additional time for pinch-off to occur before the rupture moves entirely up the film bridge.

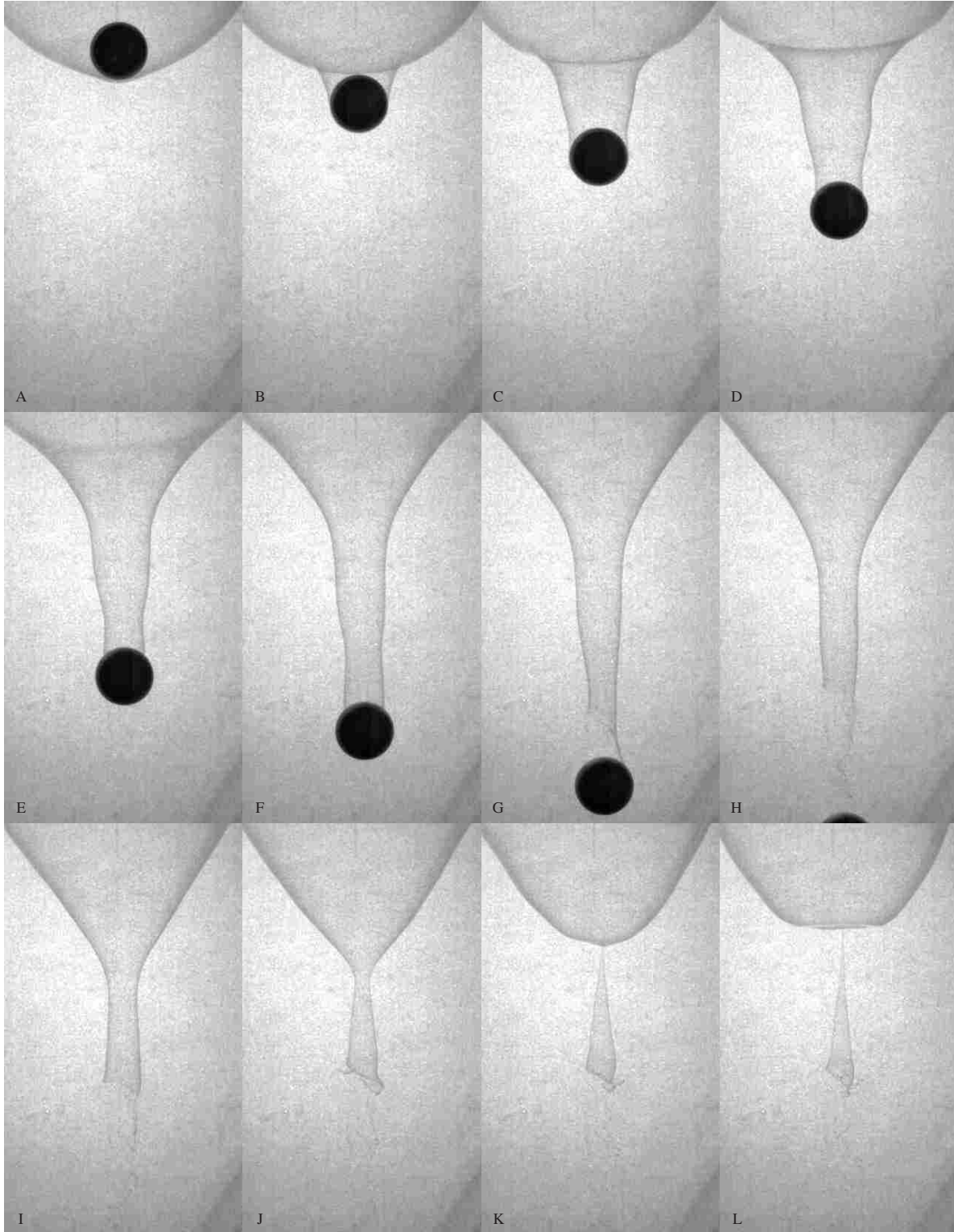


Figure 4.5: This interesting phenomenon of film rupture and pinch-off repair occurred in the lower hemisphere of a 5 cm radius bubble with a 9.4 mm radius aluminum sphere falling through it. The sphere was dropped from a height of 95 cm. Note the thinning rupture by frame (G) and the pinch-off of the ruptured film in frame (K).

#### 4.4 Comparison of Linear Stretch Rates

The surface area of a curve revolved about an axis is found according to the following equation:

$$A_{surf} = \int_C 2\pi r ds \quad (4.1)$$

where  $r$  is the radius of rotation and  $ds$  is the differential arc length. Using this equation, an approximation of the increase of surface area of the bubble's soap film as the sphere passes through it may be found by capturing the profiles of the film in time. Using these profiles we may approximate the differential arc length  $ds$  as the distance between two points on the surface and the radius of rotation,  $r$ , as the distance of the film profile from the center of the bubble (assuming the sphere was dropped through the center of the bubble). Examples of such profiles may be found in Figure 4.6.

Applying the above formulation for approximating the surface area of the deformed bubble and plotting the percent increase of surface area as a function of time yields Figure 4.7.

The linearity of the percent increase of surface area found in regimes II and III is an interesting fact and begs the question of why the film response is linear. One possible answer is found by using the surface tension approximation used above. The linear portions of that approximation (once the sphere has entered the bubble by more than its radius) yields surface area rates of increase of 1.63 and 3.20  $\text{m}^2/\text{s}$  for regime III and IV found in Figure 4.7. This compares well with the rates of increase found in Figure 4.6: 1.24 and 3.27  $\text{m}^2/\text{s}$  for regime III and IV respectively. While we see that the regime IV approximation is very close, under predicting the rate of surface area increase by just over 2%, the approximation for regime III over predicts by just more than 30%. Whether this discrepancy is a result of the regime or the sphere size is, at this point, unclear. As the results in Figure 4.7 for regime II seem to indicate that the film reactions in this case are non-linear, the approximation was not tested against this case.

#### 4.5 Surface Tension Forces

In the course of our investigation it was noticed that ball weight had little effect. For the most part, the balls with density less than water and those with density several times that of water

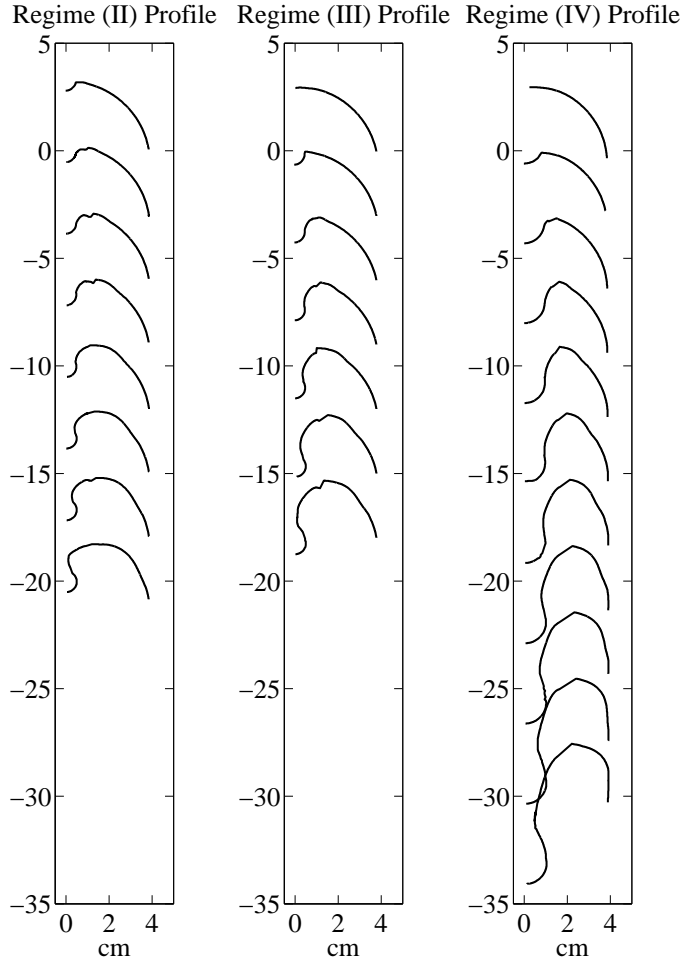


Figure 4.6: Film profile information. Each profile, with the top profile representing our initial time,  $t = 0$  s, represents the film profile after 1.5 ms from the previous profile. The profiles are offset by 3 cm per 1.5 ms for clarity. Also, each profile on each axis is the profile of a 3.75 cm bubble being deformed by a sphere. For the regime II and III profiles, the dropped sphere is a 4.8 mm radius glass sphere dropped from a height of 23.5 cm and 113.9 cm respectively. The regime IV profile was created by a 9.4 mm aluminum sphere dropped from a height of 113.9 cm.

acted the same. An explanation for this may be seen in a comparison of the surface tension forces to gravitational forces. Examination of the ratio of gravitational forces to surface tension forces,

$$\frac{F_g}{F_{st}} = \frac{mg}{2\pi r\sigma} \quad (4.2)$$

shows that gravitational forces on all of the spheres, with the exception of the smallest one, were many times that of surface tension forces, see Table 4.1. This explains why no change in sphere inertia of the dropped spheres was ever noticed, except in the smallest case.



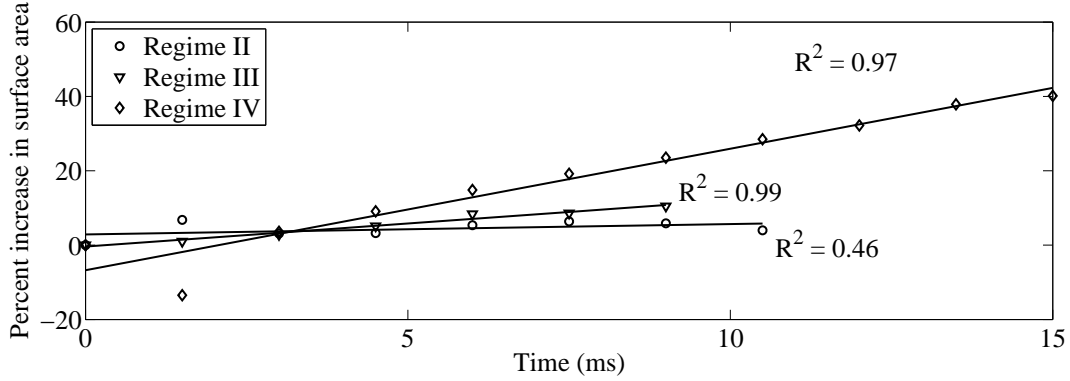


Figure 4.7: Percent increase in surface area as a function of time for the three profiles found in Figure 4.6. Each data set is fit with a linear polynomial. Note the highly linear results for regimes III and IV, while the regime II profile is very non-linear.

Table 4.1: Gravitational to surface tension forces table.

Ball Radius (mm)	$\frac{F_g}{F_{st}}$
1.1750	0.8626
3.1650	5.6271
4.7540	13.7362
6.3333	6.5614
8.7150	146.3188
9.4411	15.0912
11.1050	236.2855
11.8933	270.4387
12.6900	307.4697
17.3992	136.0807
28.5250	382.7273

## 4.6 Conclusions

This chapter has covered several interesting phenomena observed while investigating the passing of solid spheres through soap bubbles. We have examined the entrainment of the sphere by a satellite bubble, pinched-off the main soap bubble, the abortion of the pinch-off of the film bridge due to interesting pressure forces, and the remarkable ability of the soap film to repair itself after rupture has occurred. We have also discussed the rates of film stretching and examined the ratio of gravitational and surface tension forces.

## CHAPTER 5. CONCLUSIONS

This work has categorized and thoroughly documented the dropping of solid spheres through soap bubbles. The experiments were performed in two sets, each set focusing on either the upper or lower hemisphere of the bubble. Bubble and sphere sizes were varied as well as drop heights. A deeper understanding of the bubble's reaction to the passing of the spheres was gained, as well as insight to when successful passage may or may not occur. Several interesting phenomena were also noted and discussed.

An overview of these understandings, insights and noted phenomena is presented below as well as an overview of possible future areas of research which could be performed.

### 5.1 Summary

As the sphere passes through the soap film forming the bubble, the film must deform to make way for the sphere. This shape and characterization of this deformation and pinch-off is highly dependent upon the Weber number which (see Tables 3.2 and 3.3), in our case compares the sphere's inertia to the film's surface tension. It is not surprising that this dependence exists as the surface tension is continually fighting the sphere's work to deform the film. Five new and distinct Weber number regimes have been defined, see Figures 3.3 through 3.12 and Tables 3.2 and 3.3.

In addition to categorizing the deformation of the bubble caused by the spheres passage, the data was also examined to discover trends in bubble rupture. This examination yielded some key insights, such as a relationship between the Weber number and sphere size, and whether or not a rupture will occur. Also, general trends of film rupture were noted which included increased probability for film rupture as either Weber number or sphere radius increase. For example, it was noted that spheres with a radius of greater than about 0.013 m were unable to enter the bubble's upper hemisphere without causing bubble rupture. Also successful entry of spheres with radii between 0.01 m and 0.013 m are very dependent on their Weber number (see Figure 3.29). Similar,

though less well defined, conclusions were noted for the lower hemisphere. Finally, it was noticed that the relative size of the sphere to the bubble is also of importance, with 100% rupture rates occurring at a sphere to bubble radius ratio of greater than 0.55.

The interesting phenomena noted were varied in importance and relevance. Some key points include the linearity of surface area increase at mid to high Weber numbers ( $> 3000$ ), the encapsulation of the falling sphere in a satellite bubble and a competition between curvature, pressure and surface tension in film bridge pinch-off.

## **5.2 Future Work**

As was made clear in Chapter 1, work done on this topic has been limited at best. As a result, there is a myriad of avenues of research which may be pursued. Studies into more precise modeling of the bubbles soap film thickness as a function of time is an area which could add to the body of this work. As mentioned numerous times, the thickness of the film plays a key role in the outcome of the experiment. Film thickness determines whether or not the film will rupture when a given sphere is dropped from a particular height as well as the rupture type. Precise modeling of the thickness, at the point of impact as a minimum, would help to eliminate these unknowns and yield a better understanding of the phenomena.

Related to knowing the film thickness in time is the ability to control, or standardize, the initial film thickness when it is placed upon the bubble cylinder or plate. Being able to at least know that each film started at a set thickness would also yield a clearer understanding, and more precise study, of these events.

Another area of fruitful research would be to find a way to precisely model the film dynamics as the sphere passes through the bubble. Although this model would be unable to capture bubble rupture, as was mentioned in Chapter 1, if the model was able to capture the film dynamics it could be used help explain, or validate the given explanation, for some of the interesting phenomena noted in Chapter 4.

## REFERENCES

- [1] Bull, L., 1924. Recent developments in high-speed cinematography, May.
- [2] Behroozi, F., 2008. “Soap bubbles in paintings: Art and science.” *Am. J. Phys.*, **76**(12), December, pp. 1087–1091.
- [3] de Gennes, P.-G., Wyart, F. B., and Quere, D., 2004. *Capillarity and Wetting Phenomena: drops, bubbles, pearls, waves*. Springer.
- [4] Kotz, J. C., and Paul M. Treichel, J., 2003. *Chemistry and Chemical Reactivity.*, fifth ed. Thomson.
- [5] Boys, C. V., 1959. *Soap Bubbles, Their Colours And The Forces Which Mold Them*. New York, Dover Publications.
- [6] Ropars, G., Chauvat, D., Floch, A. L., O’Sullivan-Hale, M. N., and Boyd, R. W., 2006. “Dynamics of gravity-induced gradients in soap film thicknesses.” *Applied Physics Letters*, **88**(234104).
- [7] Liang, N. Y., and Chan, C. K., 1997. “Fast thickness profile measurement of a thin film by using a line scan charge coupled device camera.” *Rev. Sci. Instrum.*, **68**(12), December, pp. 4525 – 4530.
- [8] Schwartz, L. W., and Roy, R. V., 1999. “Modeling draining flow in mobile and immobile soap films.” *Journal of Colloid and Interface Science*, **218**, pp. 309–323.
- [9] Naire, S., Braun, R. J., and Snow, S. A., 2000. “Limiting cases of gravitational drainage of a vertical free film for evaluating surfactants.” *SIAM Journal on Applied Mathematics*, **61**(3), pp. 889–913.
- [10] Tompkins, H. G., 1997. *A User’s Guide to Ellipsometry*. Academic Press, Inc.
- [11] Jellison, G., 1996. “The calculation of thin film parameters from spectroscopic ellipsometry data.” *Thin Solid Films*, **291**, Dec., pp. 40–45.
- [12] Azzam, R. M. A., 1991. “Transmission ellipsometry on transparent unbacked or embedded thin films with application to soap films in air.” *Applied Optics*, **30**(19), pp. 2801–2807.
- [13] Swanepoel, R., 1985. “Determining refractive index and thickness of thin films from wavelength measurements only.” *Journal of the Optical Society of America*, **2**(8), pp. 1339–1343.
- [14] Serway, R. A., and Beichner, R. J., 2003. *Physics for Scientists and Engineers.*, Vol. III Wadsworth Group.

- [15] Hecht, E., and Zajac, A., 1974. *Optics*. Addison-Wesley.
- [16] Rayleigh, L., 1902. *Scientific Papers.*, Vol. 3 Cambridge University Press.
- [17] Ranz, W. E., 1959. “Some experiments on the dynamics of liquid films.” *Journal of Applied Physics*, **30**, pp. 1950–1955.
- [18] Culick, F. E. C., 1960. “Comments on a ruptured soap film.” *Journal of Applied Physics*, **30**, pp. 1128–1129.
- [19] Evers, L. J., Nijman, E. J., and Frens, G., 1999. “The role of structure in rupturing newton-black soap films: dynamics of a molecular bilayer.” *Colloids and Surfaces*, **149**, pp. 521–527.
- [20] Taylor, G., and Michael, D. H., 1972. “On making holes in a sheet of fluid.” *Journal of Fluid Mechanics*, **58**, pp. 628–639.
- [21] Chen, Y. J., and Steen, P. H., 1997. “Dynamics of inviscid capillary breakup: collapse and pinchoff of a film bridge.” *Journal of Fluid Mechanics*, **341**, pp. 245–267.
- [22] Delale, C. F., Tryggvason, G., and Nas, S., 2008. “Cylindrical bubble dynamics: Exact and direct numerical simulation results.” *Physics of Fluids*, **20**(4).
- [23] Kim, B., Liu, Y., Llamas, I., Jiao, X., and Rossignac, J., 2007. “Simulation of bubbles in foam with the volume control method.” *ACM Transactions on Graphics*, **26**(3), July.
- [24] Sethian, J. A., 1985. “Numerical methods for propagating fronts.” In *Proceedings of the Sept, 1985 Vallambrosa Conference*, P. Concus and R. Finn, eds., Variational Methods for Free Surface Interfaces, Springer-Verlag.
- [25] Sethian, J. A., and Smereka, P., 2003. “Level set methods for fluid interfaces.” *Annual Review of Fluid Mechanics*, **35**, pp. 341–372.
- [26] Thoroddsen, S., Takehara, K., Etoh, T., and Hatsuki, Y., 2005. “Puncturing a drop using surfactants.” *Journal of Fluid Mechanics*, **530**, pp. 295–304.
- [27] Zhao, H. K., Merriman, B., Osher, S., and Wang, L., 1998. “Capturing the behavior of bubbles and drops using the variational level set approach.” *Journal of Computational Physics*, **143**(2), July, pp. 495–518.
- [28] Nagrath, S., Jansen, K. E., and Jr., R. T. L., 2005. “Computation of incompressible bubble dynamics with a stabilized finite element level set method.” *Comput. Methods Appl. Mech. Engrg.*, **194**, pp. 4565–4587.
- [29] Sethian, J. A., 1999. *Level Set Methods and Fast Marching Methods : Evolving Interfaces in Computational Geometry, Fluid Mechanics, Computer Vision, and Materials Science*. Cambridge University Press.
- [30] Fedkiw, R. P., Aslam, T., Merriman, B., and Osher, S., 1999. “A non-oscillatory eulerian approach to interfaces in multimaterial flows (the ghost fluid method).” *Journal of Computational Physics*, **152**(2), pp. 457 – 492.

- [31] Osher, S., and Fedkiw, R., 2000. *Level Set Methods and Dynamic Implicit Surfaces.*, Vol. 154 of *Applied Mathematical Sciences* Springer.
- [32] Foster, N., and Fedkiw, R., 2001. “Practical animation of liquids.” In *Proceedings of the 28th annual conference on Computer graphics and interactive techniques*, SIGGRAPH '01, ACM, pp. 23–30.
- [33] Thoroddsen, S., Etoh, T., and Takehara, K., 2008. “High-speed imaging of drops and bubbles.” *Annu. Rev. Fluid Mech.*, **40**, pp. 257–285.
- [34] Ashgriz, N., and Poo, J. Y., 1990. “Coalescence and separation in binary collisions of liquid-drops.” *Journal of Fluid Mechanics*, **221**, pp. 183–204.
- [35] Munson, B. R., Young, D. F., and Okiishi, T. H., 2006. *Fundamentals of Fluid Mechanics.*, fifth ed. Wiley.
- [36] Gilet, T., and Bush, J. W. M., 2009. “The fluid trampoline: droplets bouncing on a soap film.” *Journal of Fluid Mechanics*, **625**, pp. 167–203.
- [37] Cryer, S. A., and Steen, P. H., 1992. “Collapse of the soap-film bridge: Quasistatic description.” *Journal of Colloid and Interface Science*, **154**(1), pp. 276–288.